

THE (p,n) REACTION ON  $^{13}\text{C}$ , A SCINTILLATING  
LIQUID ARGON TARGET, AND PROTON INDUCED  
K-SHELL IONIZATION STUDIES

by



William Desmond Ramsay, B.Eng., M.A.Sc.

A THESIS

Submitted to the Faculty of Graduate Studies  
In Partial Fulfillment of the Requirements  
for the Degree

DOCTOR OF PHILOSOPHY

Department of Physics  
University of Manitoba,  
Winnipeg, Manitoba

February, 1980



THE (p,n) REACTION ON  $^{13}\text{C}$ , A SCINTILLATING  
LIQUID ARGON TARGET, AND PROTON INDUCED  
K-SHELL IONIZATION STUDIES

BY

WILLIAM DESMOND RAMSAY

A thesis submitted to the Faculty of Graduate Studies of  
the University of Manitoba in partial fulfillment of the requirements  
of the degree of

DOCTOR OF PHILOSOPHY

©1980

Permission has been granted to the LIBRARY OF THE UNIVER-  
SITY OF MANITOBA to lend or sell copies of this thesis, to  
the NATIONAL LIBRARY OF CANADA to microfilm this  
thesis and to lend or sell copies of the film, and UNIVERSITY  
MICROFILMS to publish an abstract of this thesis.

The author reserves other publication rights, and neither the  
thesis nor extensive extracts from it may be printed or other-  
wise reproduced without the author's written permission.

## ABSTRACT

Quasielastic (p,n) differential cross sections have been measured for  $^{13}\text{C}$  for laboratory angles from  $30^\circ$  to  $150^\circ$  using proton energies of 22.5, 25.8, 30.5 and 37.4 MeV. IAS neutrons were detected by means of the University of Manitoba Cyclotron Laboratory neutron time of flight facility. The detector was a liquid scintillator (NE213), used at flight paths ranging from 4m to 6m.

The experiment was performed in preparation for the measurement of polarization and analysing power for the same  $^{13}\text{C}(p,n_0)$  reaction. Conzett's Theorem (Conzett, 1974) states that polarization should be equal to analyzing power for (p,n) reactions linking isobaric analog states. Departures from  $P=A$  may yield information about charge symmetry breaking and asymmetric spin flip probability. The present study has confirmed the suitability of the facility and the P - A program is proceeding.

The  $^{13}\text{C}(p,n)$  data are compared with predictions of the Lane optical model (Lane 1962, Satchler 1969), which predicts (p,p) elastic, (p,n) quasielastic and (n,n) elastic observables from a single isospin dependent potential. Calculations performed using an energy dependent Lane potential (Patterson et al., 1976) formulated for heavier nuclei ( $A > 40$ ) give only fair agreement with the data. By using a Lane potential deduced from global lp-shell neutron and proton potentials (Watson et al. 1969), the agreement with

the data is considerably improved. The results indicate that the strengths assigned to the isospin dependent part of the Lane potential are nearly correct, but that the geometry must be altered. There is some indication that a surface peaked form factor for the real isospin dependent potential may be required to reproduce the shape of the angular distributions.

An existing liquid helium neutron polarimeter has been used as a scintillating liquid argon target. It is found that the scintillations induced in liquid argon by fast neutrons are of low intensity but are adequate to permit the use of an associated particle system for reducing background and with a moderate amount of shielding a clean scattering experiment can be performed. A "recipe" is given for producing high quality liquid argon simply and economically.

Cross sections for proton induced K-shell ionization have been measured at proton energies of 24, 32 and 44 MeV incident on targets of gold, europium, silver, rubidium and copper. These are among the first data in this energy range. The data are compared to the results of PWBA calculations and found to be consistent with these results.  $K_{\beta}/K_{\alpha}$  intensity ratios are measured for each target and energy. A check is made for possible dependence of the  $K_{\beta}/K_{\alpha}$  ratio upon the energy of the inducing proton but, to the accuracy of the experiment, no such energy dependence is found. The

measured  $K_{\beta}/K_{\alpha}$  ratios are found to be in agreement with the theoretical predictions of Scofield (1974).

Calculations are made of the spectrum of "transition radiation" emitted when 35 MeV protons cross the interface between a vacuum and a metallic target. The intensity is found to fall sharply in the ultraviolet. An estimate is made of the transition radiation appearing in the x-ray part of the spectrum during a typical proton induced x-ray experiment and it is found to be insignificant.

## ACKNOWLEDGEMENTS

I wish to acknowledge the great amount of assistance and encouragement given to me during the course of this work, by my supervisor, Dr. Jasper McKee. I would also like to thank Dr. Jim Birchall, who has been involved at almost every stage of this work, and from whom I have learned so much. Thanks are also due to Dr. Swapan Datta for supplying the computer code TWAVE; Dr. John Watson for the Kent State Monte Carlo neutron efficiency program, and Dr. Richard Walter and Dr. Roger Byrd of Duke University for making some of their data available to us prior to publication. Thanks also to Yuen Cheng for all her help with the computer. I am grateful to the staff of the machine shop, the cyclotron technical personnel, and the office staff for their unfailing helpfulness and co-operation. Finally, thanks to my wife Shirley for her excellent work in typing the thesis, and to Cathy, Scott and Shirley for putting up with everything.

## PREFACE

The experimental work described in this thesis was undertaken over a period of time from mid 1976 to late 1979. They are presented here in reverse chronological order, the  $^{13}\text{C}(p,n)$  work being the most recent.

The K-shell ionization measurements represent a completed program. Some work is continuing on the use of proton induced x-ray emission for elemental analysis, but the ionization cross section measurements reported are complete and the results published (Ramsay & McKee, 1978; Ramsay et al., 1978; Kamal et al., 1980).

The work on the liquid argon target is part of an on-going (p,n) program, but that part reported here is self contained (Ramsay et al., 1980).

The  $^{13}\text{C}(p,n)^{13}\text{N}$  experiment is the most recent and most complex of the three. It is the first experiment in a program being undertaken at the University of Manitoba Cyclotron Laboratory to study (p,n) reactions linking analog states of mirror nuclei.

The  $^{13}\text{C}(p,n)$  chapter is the most comprehensive. Since much experimental and data reduction technique is common to the three chapters, I have attempted to avoid unnecessary duplication of details. For example, the electronics in chapter one is the most sophisticated and is described in detail. The electronics in the other chapters is essentially a sub-set of this.

It is hoped that this thesis will form a useful reference for those continuing with the (p,n) program.

## TABLE OF CONTENTS

ABSTRACT	
ACKNOWLEDGEMENTS	
PREFACE	
TABLE OF CONTENTS	
LIST OF FIGURES	
LIST OF TABLES	
<u>CHAPTER 1. THE (p,n) REACTION ON <math>^{13}\text{C}</math></u>	
1.1 INTRODUCTION	2
1.2 THEORETICAL BACKGROUND	6
1.2.1 The Lane Optical Potential	
1.2.2 Extraction of the Symmetry Term	
1.2.3 Matrix Elements of the Lane Potential	
1.2.4 The Coupled Equations	
1.2.5 Equations Used By TWAVE	
1.3 EXPERIMENTAL METHOD	16
1.3.1 Instrumentation	
1.3.2 Detector Thresholds	
1.3.3 Technical Summary	
1.4 ANALYSIS AND RESULTS	38
1.4.1 Neutron Detection Efficiency	
1.4.2 Extracting Neutron Yields	
1.4.3 Normalization	
1.4.4 Error Summary and Results	
1.5 LANE MODEL CALCULATIONS	64
1.5.1 Form of the Potential	
1.5.2 Determining Parameters of the Potential	
1.5.3 Applicability of the Analysis	
1.6 SUMMARY AND CONCLUSIONS	82
<u>CHAPTER 2. A SCINTILLATING LIQUID ARGON TARGET</u>	
2.1 INTRODUCTION	85
2.2 EXPERIMENTAL	89
2.2.1 The Polarimeter	
2.2.2 Making Liquid Argon	
2.2.3 Testing with an $\alpha$ -source	

2.2.4	Testing with Fast Neutrons	
2.2.4.1	Delayed coincidence	
2.2.4.2	Time of flight	
2.2.4.3	Pulse height	
2.2.5	Isoangular Volume	

2.3	CONCLUSION	110
-----	------------	-----

2.4	FUTURE WORK	112
-----	-------------	-----

### CHAPTER 3. PROTON INDUCED K-SHELL IONIZATION STUDIES

3.1	INTRODUCTION	114
-----	--------------	-----

3.2	THEORIES OF K-SHELL IONIZATION	116
-----	--------------------------------	-----

3.2.1	PWBA (Plane Wave Born Approximation)	
-------	--------------------------------------	--

3.2.2	SCA (Semi-Classical Approximation)	
-------	------------------------------------	--

3.2.3	BEA (Binary Encounter Approximation)	
-------	--------------------------------------	--

3.3	THE EXPERIMENT	121
-----	----------------	-----

3.3.1	Correction for Satellite Peaks	
-------	--------------------------------	--

3.3.2	Ge(Li) Detector Efficiency	
-------	----------------------------	--

3.3.3	Absorption Corrections	
-------	------------------------	--

3.3.4	Results	
-------	---------	--

3.4	RELATED WORK	130
-----	--------------	-----

3.4.1	$K_{\beta}/K_{\alpha}$ x-ray Intensity Ratios	
-------	---	--

3.4.2	Transition Radiation	
-------	----------------------	--

3.4.2.1	Theory	
---------	--------	--

3.5	SUMMARY AND CONCLUSIONS	142
-----	-------------------------	-----

### REFERENCES

## LIST OF FIGURES

- 1-1 Floor plan of U of M cyclotron Laboratory
- 1-2 Neutron time of flight spectrum obtained with flight path of 4.17 m at a laboratory angle of  $100^\circ$
- 1-3 Cross section of target ladder
- 1-4 Electronics for the experiment
- 1-5 Effectiveness of the n- $\gamma$  pulse shape discrimination
- 1-6 Pulse height distributions
- 1-7 Computer simulation of pulse height distributions
- 1-8 Calculated neutron detection efficiency for 11.43 cm dia. by 12.7 cm thick NE213
- 1-9 Pulse height spectrum from  $^{60}\text{Co}$
- 1-10 Neutron time of flight spectra with and without shadow bar
- 1-11 Examples of well separated and overlapping peaks
- 1-12 Method of estimating overlap correction
- 1-13 Measured neutron angular distributions for the  $^{13}\text{C}(p,n_0)^{13}\text{N}$  reaction
- 1-14 Results of Lane model calculations using a global Lane potential
- 1-15 Results of Lane model calculations using trial Lane potential inferred from the global l-p shell potentials of Watson et al. (1969) (Table 1-7)
- 2-1 Method of measuring neutron polarization
- 2-2 Cross section of the polarimeter
- 2-3 Method of preparing liquid argon

- 2-4 Pulse height spectrum of scintillations induced in liquid argon by alpha particles
- 2-5 Pulse height spectra for different alpha source positions
- 2-6 Testing with fast neutrons
- 2-7 Electronics used in testing with fast neutrons
- 2-8 n- $\gamma$  PSD spectrum
- 2-9 Spectrum of time differences between neutron events in the polarimeter and the side detector
- 2-10 Coordinate system and notation
- 2-11 Isoangular shape
- 3-1 Schematic diagram of the experiment
- 3-2 Sample x-ray spectra
- 3-3 Ge(li) detector efficiency
- 3-4 K-shell ionization cross sections
- 3-5 Experimental values of  $K_{\beta}/K_{\alpha}$  as a function of atomic number
- 3-6 Transition radiation
- 3-7 Transition radiation spectra for copper and silver

## LIST OF TABLES

- 1-1 Technical data for the  $^{13}\text{C}(p,n_0)^{13}\text{N}$  experiment
- 1-2 Parameters used in the detector efficiency calculation
- 1-3 Dependence of beam monitor yield on energy
- 1-4 Cross section data for  $^{13}\text{C}(p,n_0)^{13}\text{N}$
- 1-5 Lane model consistent transformations between different representations of the potential
- 1-6 Parameters of  $^{13}\text{C}$  Lane potential taken from "global" analysis of Patterson et al
- 1-7 The Watson lp-shell optical potential
- 1-8 Lane potentials implied by the potential of table 1-7
- 3-1 Transmission through Mylar and air
- 3-2 Measured  $K_\beta/K_\alpha$  ratios
- 3-3 Parameters for typical proton induced x-ray experiment

CHAPTER 1

THE (p,n) REACTION ON  $^{13}\text{C}$

## 1.1 INTRODUCTION

The  $^{13}\text{C}(p,n_0)^{13}\text{N}$  experiment described in this chapter is the first in a series of experiments designed to study (p,n) reactions linking isobaric analog states of mirror nuclei. The interesting thing about such reactions is that it is possible to consider the target and residual nucleus to be the same except for the direction of their isospin. The  $^{13}\text{C}$  and  $^{13}\text{N}$  ground states, for example, both have spin  $\frac{1}{2}$ , negative parity, and almost the same mass. The only difference is charge state. They can thus be thought of as different isospin states of the same isospin  $\frac{1}{2}$  ( $T = \frac{1}{2}$ ) "particle" in the same sense that the proton and neutron can be considered to be  $T_3 = -\frac{1}{2}$  and  $T_3 = \frac{1}{2}$  states of the same  $T = \frac{1}{2}$  nucleon, or that the  $\pi^-$ ,  $\pi^0$  and  $\pi^+$  are considered different isospin states of a  $T = 1$  pion.

In the context of the above isospin formalism, (p,n) reactions leading to the isobaric analog state of the target are simply elastic scattering with isospin flip. Because of this simplicity such reactions are sometimes referred to as "quasielastic".

If isospin is a good quantum number for the reaction and the only change is in isospin projection, then this has several implications. One is that the (p,p) elastic, (p,n) quasielastic, and (n,n) elastic processes can all be described by a single Lane model (Lane, 1962; Satchler, 1969) optical potential,  $U = U_0 + 4(\vec{T} \cdot \vec{t})U_1/A$ , where  $\vec{T}$  is the

isospin of the target,  $\vec{t}$  the isospin of the projectile, and  $A$  the atomic number of the target.

Another consequence of isospin conservation is Conzett's Theorem (Conzett, 1974) which states that the analyzing power,  $A(\theta)$ , in the reaction  $A(\vec{p},n)B$  should be equal to the polarization,  $P(\theta)$ , in the reaction  $A(p,\vec{n})B$ , provided  $A$  and  $B$  are isobaric analog states - i.e. that  $A(p,n)B$  is quasielastic.

While the results of the Lane model and of Conzett's Theorem are based only on the assumption that the  $(p,n)$  reaction involved connects isobaric analog states, one would expect the results to be more nearly correct if the target and residual nucleus are members of an isospin doublet (mirror nuclei -  $T = \frac{1}{2}$ ) than if they are members of a larger isospin multiplet. This is because a  $\Delta T_3 = 1$   $(p,n)$  transition between members of an isospin doublet corresponds to a  $180^\circ$  rotation in isospin space and invariance under this operation only requires the limited assumption of charge symmetry. On the other hand, conservation of isospin for a  $\Delta T_3 = 1$  transition between members of a larger ( $T \geq 1$ ) isospin multiplet requires complete rotational invariance in isospin space which is synonymous with the more general (and less well established) assumption of charge independence.

Data of Byrd (1978) for the mirror reaction  $^{15}\text{N}(p,n)^{15}\text{O}$  at energies up to 12 MeV suggest a discrepancy between  $P$  and  $A$ . According to Conzett's Theorem, such dis-

crepancies indicate a breaking of charge symmetry. Byrd points out by means of fairly simple arguments credited to Arnold (1977) that  $P \neq A$  also means that spin flip probability must be asymmetric - that is, the cross section for transition from a spin up proton to a spin down neutron must be different from the cross section for transition from a spin down proton to a spin up neutron. Whether this statement is saying the same thing as Conzett's Theorem is not clear. Careful measurements of  $P$  and  $A$  at a series of energies will help to answer this question.

We intend to extend the  $^{15}\text{N}(p,n)$  measures of Byrd to higher energy, and as well study the very similar  $^{13}\text{C}(p,n)^{13}\text{N}$  reaction. It was considered best to start the experimental program with the  $^{13}\text{C}(p,n)^{13}\text{N}$  reaction. The  $^{13}\text{C}$  target can be made thicker than the  $^{15}\text{N}$  target, which is important because the polarized beam intensity is expected to be initially quite low. In addition the  $^{13}\text{C}$  target is self supporting. This means that no background from a gas cell is present and makes it easier to ensure that the rest of the experiment is working properly.

We have measured  $^{13}\text{C}(p,n)^{13}\text{N}$  differential cross sections at energies of 22.5, 25.8, 30.5, and 37.4 MeV for laboratory angles between  $30^\circ$  and  $150^\circ$ . This experiment provided a very valuable test of the experimental equipment and procedure, and the measured cross sections permit accurate predictions to be made of the running time required for

the  $^{13}\text{C}(\vec{p},n)^{13}\text{N}$  experiment. Also, these cross section measurements are a good means of investigating the  $^{13}\text{C}$  plus nucleon Lane potential. The balance of this chapter is devoted to details of the experiment and its interpretation within the context of the Lane model.

## 1.2 THEORETICAL BACKGROUND

### 1.2.1 The Lane Optical Potential

Conventional optical potentials of the form  $U=V+iW$  have been quite successful in describing nucleon nucleus elastic scattering. In practice one adjusts the strength and shape of  $V$  and  $W$  to fit  $(p,p)$  and  $(n,n)$  data. "Global" optical potentials, providing fits to proton and neutron data for a wide range of nuclei (e.g. Becchetti and Greenlees, 1969) are always found to require a "symmetry term" proportional to  $(N-Z)/A$ . Such a potential can be written

$$U=U_0 \pm \left( \frac{N-Z}{A} \right) U_1 \quad 1-1$$

where the negative sign is for protons and the positive sign for neutrons.  $U_0$  and  $U_1$  are in general complex and  $U_1$  is positive so  $U$  will be more attractive for protons in the case of a nucleus with neutron excess. That this should be the case is a direct consequence of the Pauli principle. The strongest force is between particles in the <sup>3</sup>S state which because of the Pauli principle is allowed only for unlike particles. As a result incident protons interact mainly with neutrons and find a neutron rich nucleus more attractive. The reverse will be true for neutrons. If  $N=Z$  of course the symmetry term will be zero and the only difference between proton and neutron potentials will be Coulomb.

It was pointed out by Lane (1962) that a more satisfactory way of writing a potential such as 1-1 was

the periodic table.

A much more direct way of measuring  $U_1$  is by means of (p,n) reactions leading to the isobaric analog state (IAS) of the target and it is here that the Lane representation (equation 1-2) shows its main formal advantage. The expansion of  $(\vec{t} \cdot \vec{T})$  contains not only the  $t_3 T_3$  term giving (p,p) and (n,n) potentials, but also a  $t_+ T_-$  term predicting the (p,n) transition to the isobaric analog state. In fact, as will be shown shortly, the whole interaction responsible for such "quasielastic" transitions is simply

$$U_{pn} = \langle n | U | p \rangle = \frac{2(2T)^{\frac{1}{2}}}{A} U_1 \quad .$$

Thus it is evident that the quasielastic (p,n) reaction provides a very sensitive tool for investigating the details of  $U_1$  .

### 1.2.3 Matrix Elements of the Lane Potential

The above relation may be deduced from expansion of the quantity  $\vec{t} \cdot \vec{T}$  in terms of raising and lowering operators.

$$\vec{t} \cdot \vec{T} = \frac{1}{2}(t_+ T_- + t_- T_+) + t_3 T_3 \quad 1-3$$

where, as in the usual angular momentum relation,

$T_{\pm} = T_1 \pm iT_2$ . The action of the raising and lowering operators is given by

$$\begin{aligned} T_{\pm} |T, T_3\rangle &= \sqrt{T(T+1) - T_3(T_3 \pm 1)} |T, T_3 \pm 1\rangle \\ &= \left[ (T \pm T_3 + 1)(T \mp T_3) \right]^{\frac{1}{2}} |T, T_3 \pm 1\rangle \quad . \end{aligned}$$

In particular (nuclear ground state with  $T = T_3$ )

$$T_- |T, T\rangle = (2T)^{\frac{1}{2}} |T, T-1\rangle \quad 1-4a$$

$$T_+ |T, T-1\rangle = (2T)^{\frac{1}{2}} |T, T\rangle \quad . \quad 1-4b$$

volunteer status which was compared with MMPI, occupation, income, education, and psychiatric diagnosis, all of which had been obtained at earlier visits. The authors noted that there were fewer schizophrenics among the volunteers and therefore concluded that degree of psychopathology influences volunteering. Furthermore, they believed that the participants were more motivated about their treatment. Patient records obtained at some undisclosed time after the study were examined and they demonstrated that 57% of those who had volunteered had also continued therapy or been referred elsewhere. On the other hand, 69% of nonvolunteers had terminated early from the program.

The study is important since it suggests that nonparticipants are also noncompliant. Thus, participants may form a select sample with respect to compliance. However, it is possible that the contact with investigators and the consequences of a request to volunteer in this situation may have differentially affected later attendance in the clinic and, therefore, participants in general may not necessarily be more compliant. Conversely and equally important, prior experiences of patients in the clinic may have influenced tendency to volunteer.

It appears then, that it is still not known whether sample selection methods result in the creation of a compliant sample. Therefore, the present study was designed to examine prior compliance of participants and nonparticipants in a blood

We see that  $T_-$  converts the target in isospin state  $|T, T\rangle$  to its analog,  $|T, T-1\rangle$ . Similarly  $t_+$  will convert a proton,  $|\frac{1}{2}, -\frac{1}{2}\rangle$ , to a neutron,  $|\frac{1}{2}, \frac{1}{2}\rangle$ .

Let the initial state of proton and target nucleus (proton-core state) and the final neutron-analog state be represented in the following way:-

$$\text{initial state: } |T, T\rangle |\frac{1}{2}, -\frac{1}{2}\rangle \equiv |pC\rangle \quad 1-5a$$

$$\text{final state: } |T, T-1\rangle |\frac{1}{2}, \frac{1}{2}\rangle \equiv |nA\rangle \quad 1-5b$$

The matrix element of  $U$  between these isospin states is then

$$\begin{aligned} U_{pn} &= \langle nA | U | pC \rangle \\ &= \frac{4U_1}{A} \langle nA | \vec{t}_+ \cdot \vec{T} | pC \rangle \\ &= \frac{2U_1}{A} \langle nA | t_+ T_- | pC \rangle \end{aligned}$$

$$\begin{aligned} \text{and since } t_+ T_- |T, T\rangle |\frac{1}{2}, -\frac{1}{2}\rangle \\ = (2T)^{\frac{1}{2}} |T, T-1\rangle |\frac{1}{2}, \frac{1}{2}\rangle = (2T)^{\frac{1}{2}} |nA\rangle \end{aligned}$$

$$\text{we have } U_{pn} = \langle nA | U | pC \rangle = \frac{2(2T)^{\frac{1}{2}}}{A} U_1$$

$$\text{similarly, } U_{np} = \langle pC | U | nA \rangle = \frac{2(2T)^{\frac{1}{2}}}{A} U_1$$

Including for completeness the trivial diagonal matrix elements we have then

$$U_{pC} = U_0 - \frac{2T}{A} U_1 \quad 1-6a$$

$$U_{nC} = U_0 + \frac{2T}{A} U_1 \quad 1-6b$$

$$U_{nA} = U_0 + \frac{2(T-1)}{A} U_1 \quad 1-6c$$

$$U_{pn} = U_{np} = \frac{2(2T)^{\frac{1}{2}}}{A} U_1 \quad 1-6d$$

For a mirror transition ( $T=\frac{1}{2}$ ) these become

$$U_{pC} = U_0 - \frac{U_1}{A} \quad 1-7a$$

$$U_{nC} = U_0 + \frac{U_1}{A} \quad 1-7b$$

$$U_{nA} = U_0 - \frac{U_1}{A} \quad 1-7c$$

$$U_{pn} = \frac{2U_1}{A} \quad 1-7d$$

Equations 1-7 are appropriate for the  $^{13}\text{C}(p,n)^{13}\text{N}$  reaction under study.

#### 1.2.4 The Coupled Equations

The Schrödinger equation for relative motion may be written

$$(H-E)|\psi\rangle = 0 \quad ,$$

in detail,

$$\left\{ \frac{-\hbar^2}{2\mu} \nabla^2 + U + \left\{ \left( \frac{1}{2} - t_3 \right) U_C \right\} - \left\{ E_p - \left( \frac{1}{2} + t_3 \right) \Delta E_C \right\} \right\} |\psi\rangle = 0$$

where  $\mu$  is the reduced mass,  $U$  the charge independent Lane potential,  $U_C$  the electrostatic potential felt by a proton,  $E_p$  the relative energy of the proton target system and  $\Delta E_C$  the Coulomb displacement energy of the analog state. For the quasielastic (p,n) reaction  $\Delta E_C = -Q$ , where  $Q$  is the  $Q$  value of the reaction. Note that for neutrons ( $t_3 = \frac{1}{2}$ ) the electrostatic term is zero and the last term,  $E_p - (\frac{1}{2} + t_3) \Delta E_C$ , becomes  $E_p + Q$  which is just the neutron energy (centre of mass system). For protons the term is  $E_p$ .

Because of the  $\vec{t} \cdot \vec{T}$  coupling between the target and its analog state, the state  $|\psi\rangle$  may be written

$$|\psi\rangle = \chi_p |pC\rangle + \chi_n |nA\rangle \quad 1-8$$

The kets are the product isospin states of equations 1-5 and  $\chi_p$  and  $\chi_n$  are wave functions for the relative motion of the proton-core and neutron-analog systems respectively.

Taking  $\langle pC | H-E | \psi \rangle$  and  $\langle nA | H-E | \psi \rangle$  to project out the  $|pC\rangle$  and  $|nA\rangle$  components and making use of the matrix elements 1-6 gives the coupled equations

$$\left( \frac{-\hbar^2}{2\mu} \nabla^2 + U_0 - \frac{2T}{A} U_1 + U_c - E_p \right) \chi_p = - \frac{2(2T)^{\frac{1}{2}}}{A} U_1 \chi_n \quad 1-9a$$

$$\left( \frac{-\hbar^2}{2\mu} \nabla^2 + U_0 + \frac{2(T-1)}{A} U_1 - (E_p - \Delta E_c) \right) \chi_n = - \frac{2(2T)^{\frac{1}{2}}}{A} U_1 \chi_p \quad 1-9b$$

which may be written rather neatly as

$$(K + U_p - E_p) \chi_p = -U_{pn} \chi_n \quad 1-10a$$

$$(K + U_n - E_n) \chi_n = -U_{np} \chi_p \quad 1-10b$$

where  $K$  is the kinetic energy operator;  $U_p = U_{pC} + U_c$  is the potential experienced by the proton, namely the Lane proton-core potential plus the electrostatic potential;  $U_n = U_{nA}$  is the Lane neutron-analog potential experienced by the outgoing neutron;  $E_p$  is the centre of mass energy for the incident proton plus target nucleus system;  $E_n$  is the centre of mass energy for the outgoing neutron plus analog state residual nucleus system;  $U_{pn} = U_{np} = 2(2T)^{\frac{1}{2}} U_1 / A$  is the coupling term. If  $U_{np} = 0$  the equations are decoupled and we would have separate proton and neutron equations.

From established scattering theory (e.g. Messiah, 1965) the  $(p,n)$  transition amplitude is given by

$$T_{pn} = \int \chi_{no}^{(-)*} \langle nA | \frac{4(\vec{t} \cdot \vec{T})}{A} U_1 | pC \rangle \chi_p^{(+)} d^3 r$$

where  $\chi_p$  is the exact solution of the coupled equations

1-10 and  $\chi_{no}$  is the homogeneous solution of 1-10b, found by setting the right hand side equal to zero. The (+) and (-) refer to asymptotically incoming or outgoing boundary conditions.

Applying the previous result (1-6) for the matrix element gives

$$T_{pn} = \frac{2(2T)^{\frac{1}{2}}}{A} \int \chi_{no}^{(-)*} U_1 \chi_p^{(+)} d^3 r \quad . \quad 1-11$$

In terms of this transition amplitude the differential cross section is

$$\frac{d\sigma}{d\Omega} = \left( \frac{\mu}{2\pi\hbar^2} \right)^2 \frac{k_n}{k_p} \left| T_{pn} \right|^2$$

where  $k_n$  and  $k_p$  are the neutron and proton relative wave numbers.

If the coupling term is small it is possible to neglect it and replace the exact solution  $\chi_p$  with the homogeneous solution of the first equation. This results in the Distorted Wave Born Approximation (DWBA) for the transition amplitude. For nuclei with  $A > 40$  the coupling term is less than 4% of the main potential and DWBA is probably reasonable. The coupling term is considerably larger for light nuclei, for example 11% for  ${}^9\text{Be}$  and around 8% for  ${}^{13}\text{C}$ . In this analysis we use the computer code TWAVE (Cotanch, 1973) which solves the coupled equations exactly. In addition to the (p,n) cross section, TWAVE calculates other observables such as the (p,p) cross

section and polarization. As was pointed out by Cotanch and Robson (1973 a), the theoretical elastic cross section is decreased by 5% to 15% depending on the coupling term when solving the coupled equations. This is due to the additional neutron channel which provides an alternate escape for the flux. It is worth bearing this in mind when comparing the (p,p) predictions of a coupled channels Lane model calculation to existing optical model calculations. The Lane model (p,p) potential may require a slightly smaller imaginary part to fit the same (p,p) data.

#### 1.2.5 Equations Used by TWAVE

For use in numerical calculations the usual partial wave decomposition is made. This removes the angular dependence and reduces the three dimensional equations 1-9 to one dimensional radial equations with the appearance of the usual  $\frac{\hbar^2}{2\mu} \frac{\ell(\ell+1)}{r^2}$  centrifugal potential. The resulting coupled radial equations are

$$\left( \frac{d^2}{dr^2} - \frac{\ell(\ell+1)}{r^2} + \frac{2\mu}{\hbar^2} (E_p - U_p^{\ell j}(r)) \right) f_{\ell j}^p(r) = \frac{2\mu}{\hbar^2} U_{pn}(r) f_{\ell j}^n(r) \quad 1-12a$$

$$\left( \frac{d^2}{dr^2} - \frac{\ell(\ell+1)}{r^2} + \frac{2\mu}{\hbar^2} (E_n - U_n^{\ell j}(r)) \right) f_{\ell j}^n(r) = \frac{2\mu}{\hbar^2} U_{np}(r) f_{\ell j}^p(r) \quad 1-12b$$

where p refers to proton, n to neutron and  $j = \ell \pm \frac{1}{2}$  depending on whether spin is parallel or anti-parallel to the orbital angular momentum. The proton and neutron potentials used

$$\text{are } U_p^{\ell j}(r) = U_{pc} + V_{so} + U_c$$

$$U_n^{\ell j}(r) = U_{nA} + V_{so} \quad .$$

$U_{pC}$  and  $U_{nA}$  are the proton-core and neutron-analog optical potentials. They may be calculated from the Lane potential (1-2) using the relations given earlier, namely

$$U_{pC} = U_0 - \frac{2T}{A} U_1 \quad 1-6a$$

and 
$$U_{nA} = U_0 + \frac{2(T-1)}{A} U_1 \quad . \quad 1-6b$$

The spin-orbit potential  $V_{so}$  has been shown explicitly and is calculated from

$$V_{so}(r) = \frac{V_0 \lambda_{so}}{90.4} \frac{\langle \vec{\ell} \cdot \vec{\sigma} \rangle}{r} \frac{df_{so}}{dr} \quad 1-13$$

where  $V_0$  is the strength (in MeV) of the real part of  $U_0$ ,  $\lambda_{so}$  is a spin-orbit strength parameter and  $f_{so}$  is a Woods-Saxon form factor using radius and diffuseness supplied as input (more details of the radial shape of this and the other potentials are included in section 1.5 on the Lane model analysis). The angular momentum scalar product  $\langle \vec{\ell} \cdot \vec{\sigma} \rangle$  equals  $\ell$  for  $j = \ell + \frac{1}{2}$  and  $-(\ell + 1)$  for  $j = \ell - \frac{1}{2}$ .

Note that the spin orbit term is real and isospin independent. A later version of TWAVE (Byrd et. al., 1979) makes provision for an isospin dependent spin orbit term. Byrd (1978) has suggested that such a term may help produce better fits to charge exchange analyzing power data.

Using the potentials supplied as input, TWAVE solves the equations 1-12 numerically up to a maximum of  $\ell=50$  and for a maximum of 400 radial steps, usually 0.1 fm each. The resulting wave functions and distorted waves may be

outputted on disc if desired. This is useful if the charge exchange reaction is only part of a multistep process and the program is being used with the companion programs TBIND and TDWUCK (Cotanch, 1973). In our case all that are required are the observables.

### 1.3 EXPERIMENTAL METHOD

Fig. 1-1 shows a plan view of the University of Manitoba Cyclotron Laboratory. The cyclotron itself is a variable energy, negative ion machine adjustable to produce proton beams nominally in the energy range of 20 MeV to 50 MeV. In practice the beam current is found to fall off rather sharply nearing 50 MeV and, to obtain reasonable beam currents, most experimenters limit themselves to, say, 46 MeV unless the higher energy is vital to the experiment.

Neutron time of flight experiments are carried out on the beam line marked "neutron time of flight facility" in Fig. 1-1. Quite a complete description of the facility has been given by Watson et al. (1979) and I will describe, therefore, only the most important features, as well as some ways in which our current setup differs from that described by Watson.

The beamline has three quadrupole doublets - one inside the wall, one between the wall and target location "B" and one between location "B" and "C" (there are also three steering magnets not shown on the diagram). By setting the quadrupoles appropriately, it is possible to produce a small beam spot at any one of the three locations "A", "B", or "C". In the paper by Watson the 41 cm chamber is shown at location "A" while in the experiment of this work we have used location "B". Location "C" is currently being used for Proton Induced X-ray Emission (P.I.X.E.) studies. Most of the

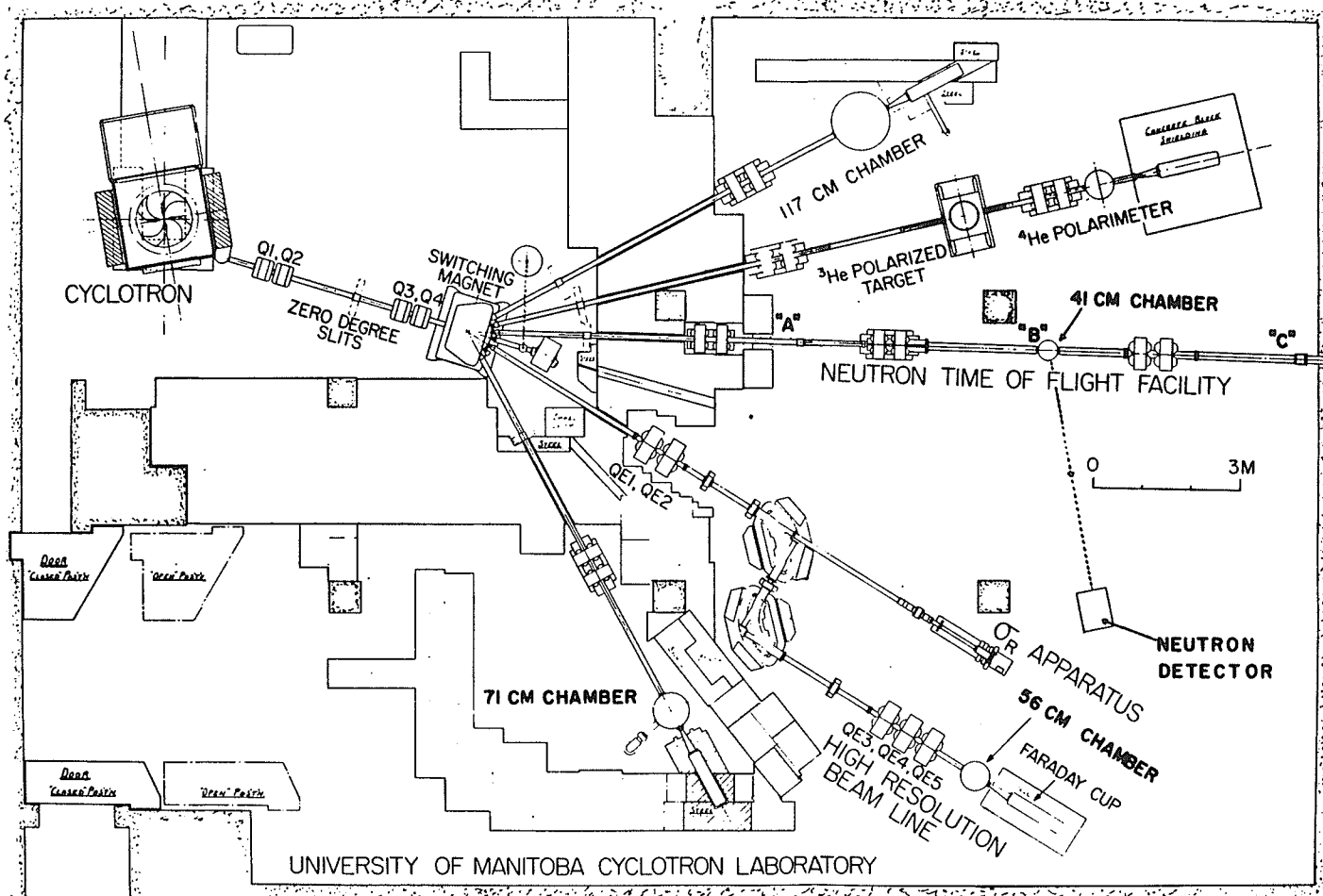


Fig. 1-1 Floor plan of the University of Manitoba Cyclotron Laboratory. The  $^{13}\text{C}(p,n)^{13}\text{N}$  experiment was performed on the beam line marked "neutron time of flight facility."

"neutron" line inside the experimental area is assembled from oversized (15 cm dia.) beam pipe. This is to reduce the neutron and gamma ray background that could result from beam halo hitting the pipe. Beam optics calculations have shown that the beam is likely to be quite large especially in the vicinity of the quadrupoles, so the 15 cm pipe is believed to be an important feature. Also important for reducing background is the location of the Faraday cup. It is located 4 m along a shaft bored 7 m into the wall. Very little radiation can be detected with the beam running through into the Faraday cup without a target in the chamber.

As mentioned, Watson shows the target chamber at location "A". The advantage of this location is that it permits relatively long neutron flight paths of 10 m or more. Long flight paths are important, particularly at higher energies, if good neutron energy resolution is required. Clearly if two very fast neutron groups have almost the same energy they will have to travel a long distance before the difference in their flight times becomes detectable.

Location "A" has the rather serious disadvantage that angular distributions can only be measured up to about  $70^\circ$ . Location "B", on the other hand, permits measurement to be made over the angular range  $20^\circ$  to  $160^\circ$  without moving the chamber. The price of the increased angular range is a reduction in flight path. The flight paths available when using location "B" are 5 to 6 m except around  $100^\circ$  where

there is a post in the way and one is restricted to 4 m. Fortunately these shorter flight paths were adequate for the  $^{13}\text{C}(p,n)^{13}\text{N}$  studies. Fig. 1-2 shows a neutron time of flight spectrum taken using a flight path of only 4 m. Notice that there is no difficulty in resolving the desired isobaric analog state (ground state here) from the excited states. Fig. 1-2 is the spectrum at  $100^\circ$  from the run at 22.5 MeV. At higher energies the separation was not as good but even at 37.2 MeV it was possible to unfold the peaks with little error (see section 1.4.2 on data analysis).

The neutron detector is an 11.4 cm dia. by 12.7 cm thick NE213 scintillator coupled to an RCA 4522 photomultiplier. The assembly is mounted near the rear of a hole bored in a standard 61.0 cm x 91.4 cm x 81.3 cm high concrete shielding block. The block is mounted on a sturdy wheeled wagon which can be rolled around the area, the detector remaining at beam height. As well as the neutron detector, we used two smaller proton detectors which were mounted on the side of the chamber away from the neutron detector. The proton detectors view the target through a 76  $\mu\text{m}$  Kapton-H window. A small 5 cm dia. by 5 cm thick NaI detector was fitted with a 3.2 mm dia. brass collimator and mounted at  $60^\circ$  to detect elastically scattered protons. This served as a beam monitor and provided a means of normalization independent of the Faraday cup. A 2.54 cm dia. by 3.8 cm NE111 fast plastic scintillator was mounted at  $30^\circ$  and

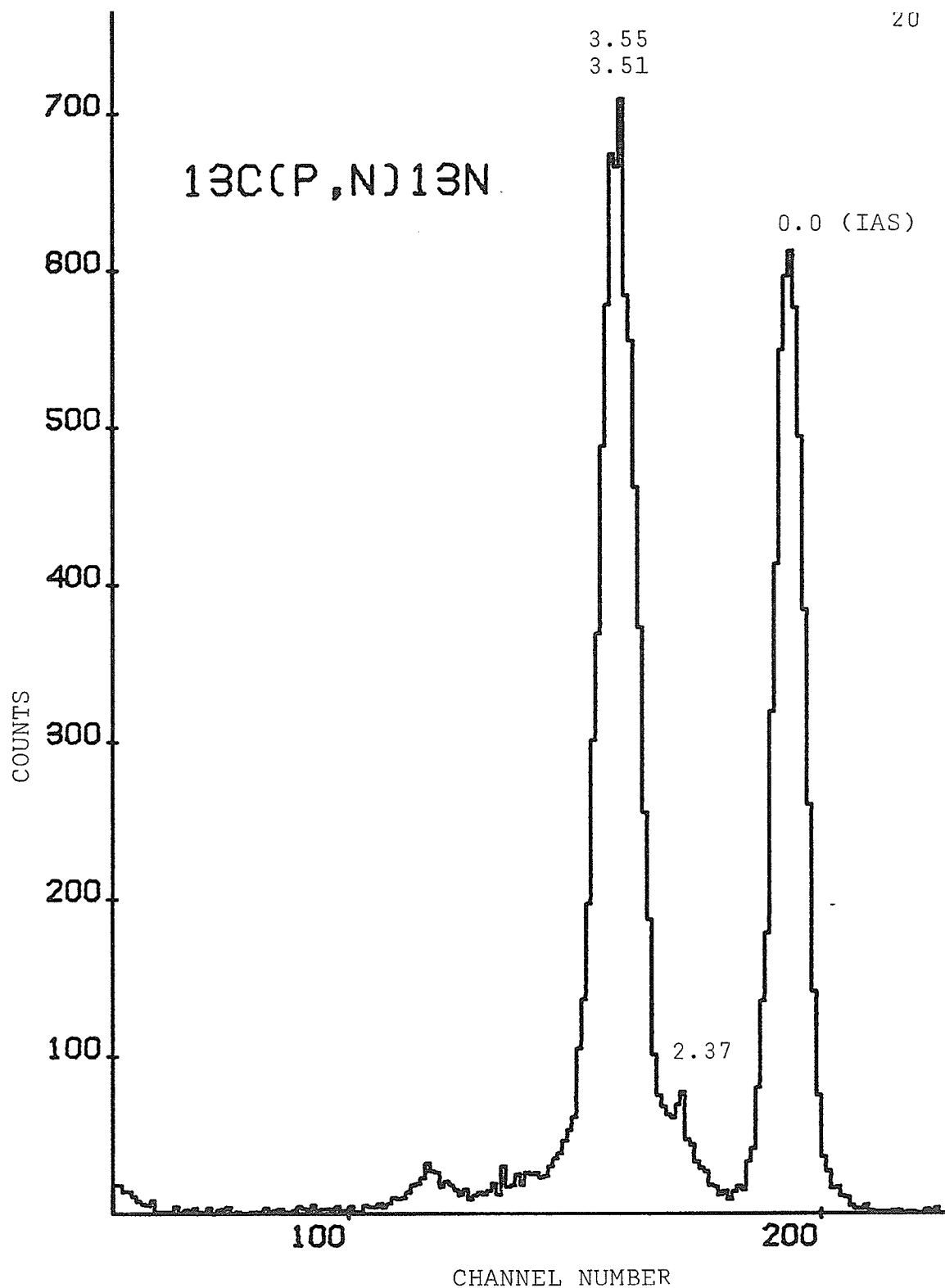


Fig. 1-2 Neutron time of flight spectrum obtained with flight path of 4.17 m at a laboratory angle of  $100^\circ$ . The incident proton energy was 22.5 MeV. Numbers indicate state energies in MeV.

detected elastic protons for the purpose of determining the time structure of the beam. The count rate of the NE111 was high enough that a usable time spectrum could be accumulated in about two seconds. By watching this time spectrum while adjusting cyclotron parameters it was possible to tune the machine for minimum beam burst width. During this experiment typical "time tunes" of 1 ns FWHM were obtained.

Before this experiment, the 41 cm chamber was modified to accept a standard target ladder and vacuum lock assembly which mounts on the top of the chamber. There were a variety of reasons for this change. First, this is a standard assembly and can be used on other chambers such as our 71 cm or 56 cm chambers. The assembly also includes a gas cell and this feature was felt to be important as the (p,n) program is intended to include gas targets, for example  $^{15}\text{N}$ . Finally, the vacuum lock feature enables us to insert and remove the targets or even transfer them to another chamber without venting. One slightly annoying feature of this target assembly is that the target ladder has thick struts. This means that neutrons leaving at certain angles have to penetrate about 8 mm of aluminum (see Fig. 1-3). In a test at medium neutron energy this attenuated the neutron flux by 9%, so during the experiment the target ladder was always rotated to give the neutron detector a clear view of the target.

The target itself was made from amorphous carbon

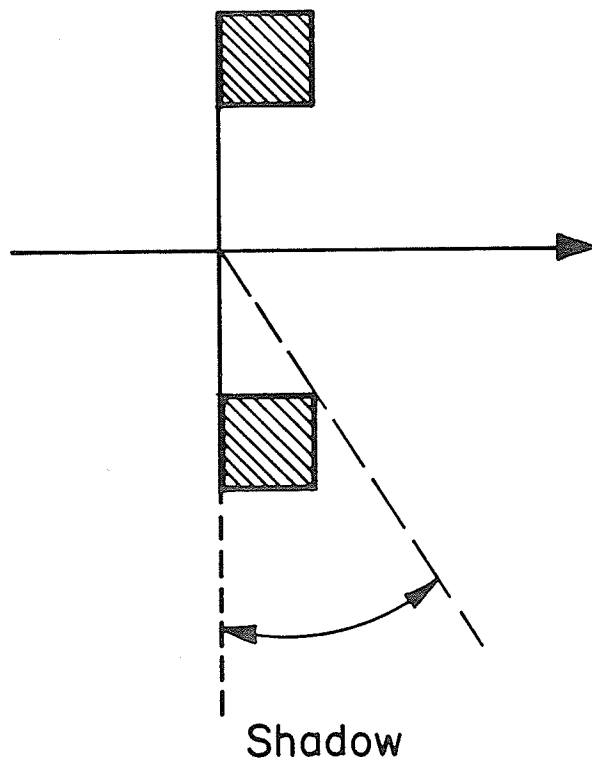


Fig. 1-3 Cross section of target ladder. Shaded areas indicate metal struts. During the experiment the ladder was always rotated so that the neutron detector was never in the shadow of a strut. The thick struts were found to attenuate the neutron flux by several percent.

enriched to 90% in  $^{13}\text{C}^\dagger$ . The charcoal-like powder was placed in a hydraulic pellet press and compacted into a carbon disc 1.9 cm in diameter. No additional binder was used. Weighing the disc and dividing by its area indicated an average thickness of  $35.9 \text{ mg/cm}^2$ . The relatively large thickness was intentional as it is intended to measure the  $^{13}\text{C}(\vec{p},n)^{13}\text{N}$  analyzing power when polarized beam becomes available. As polarized beam intensity will no doubt be quite low it was thought advisable to have as thick a target as was practicable.

Angular distributions were measured in  $10^\circ$  steps over the angular range  $30^\circ$  to  $150^\circ$  for proton energies of 22.5, 25.8, 30.5 and 37.2 MeV. Selected points were re-measured a few days apart to check repeatability. To measure the contribution to neutron background from neutrons not coming directly from the target, we used an 83.8 cm long by 7.58 cm dia. steel shadow bar that could be positioned so as to shield the detector from direct neutron flux from the target.

Beam currents on target ranged from about 30 to 100 nA, a typical figure being 50 nA. Running time per angle was from about  $\frac{1}{2}$  hour to 4 hours; long enough to keep the statistical error to approximately 1%.

---

$^\dagger$  Stohler Isotope Chemicals, Montreal, Quebec

### 1.3.1 Instrumentation

A block diagram of the electronics used is shown in Fig. 1-4. To the left are the three detectors: the NE213 liquid scintillator chosen for its good n- $\gamma$  pulse shape discrimination (PSD) properties, the NE111 fast plastic for determining the beam time structure, and the NaI beam monitor.

The NE213 is contained in a thin aluminum can with a glass window at one end.<sup>†</sup> The inside is coated with white reflector paint. The unit is fastened to the front face of the RCA 4522 14 stage photomultiplier with RTV-602 clear silicone rubber potting compound. This provides a bond that is removable yet strong enough to keep the rather heavy scintillator in place during use. The photomultiplier is operated in the grounded anode configuration. This permits the anode to be DC coupled and gives the best timing. It does, however, place the cathode at high voltage. To prevent adverse voltage gradients across the face of the photomultiplier the aluminum can of the scintillator and the conducting coating of the photomultiplier are operated at cathode potential. The entire assembly is covered with an insulating sleeve and a high permeability magnetic shield.

---

<sup>†</sup> Nuclear Enterprises BA-1 housing.

Fig. 1-4 Electronics for the experiment. Modules are standard NIM units.

LIN AMP (DDL) = linear amplifier (double delay line)

CFD = constant fraction discriminator

TSCA = timing single channel analyzer

GDC = gate and delay generator

TAC = time to amplitude converter

PRE AMP = charge sensitive (integrating) preamplifier

SPECT AMP = shaping spectroscopy amplifier

COINC = universal co-incidence unit

LIN GATE = linear gate

SCA = single channel analyzer



Fast timing signals are derived from the anode of the photomultiplier by means of a constant fraction discriminator. The use of a constant fraction discriminator results in a minimum of timing walk over a wide range of pulse heights. The fast timing signals are used to start two time to amplitude converters (TAC's). The upper TAC in Fig. 1-4 is used to differentiate between neutron and gamma signals by means of pulse shape discrimination (PSD). This widely used method is quite effective and is based on the fact that scintillations induced in the liquid scintillator by neutrons have a smaller fast component than those resulting from gammas. Thus the linear bipolar pulse resulting from integration and double delay line shaping of a neutron signal crosses zero at a later time than does the pulse derived from a gamma signal. By starting the TAC on the initiation of an event as indicated by the fast timing signal from the anode and stopping it on the zero crossing of the linear signal (as determined by the timing single channel analyser operated in crossover mode), one gets a spectrum containing two distinct peaks, one corresponding to the detection of neutrons and the other, gammas.

The centre TAC is used to derive the time of flight (TOF) information. It is started on the fast timing signal from the neutron detector<sup>†</sup> and stopped on a signal derived

---

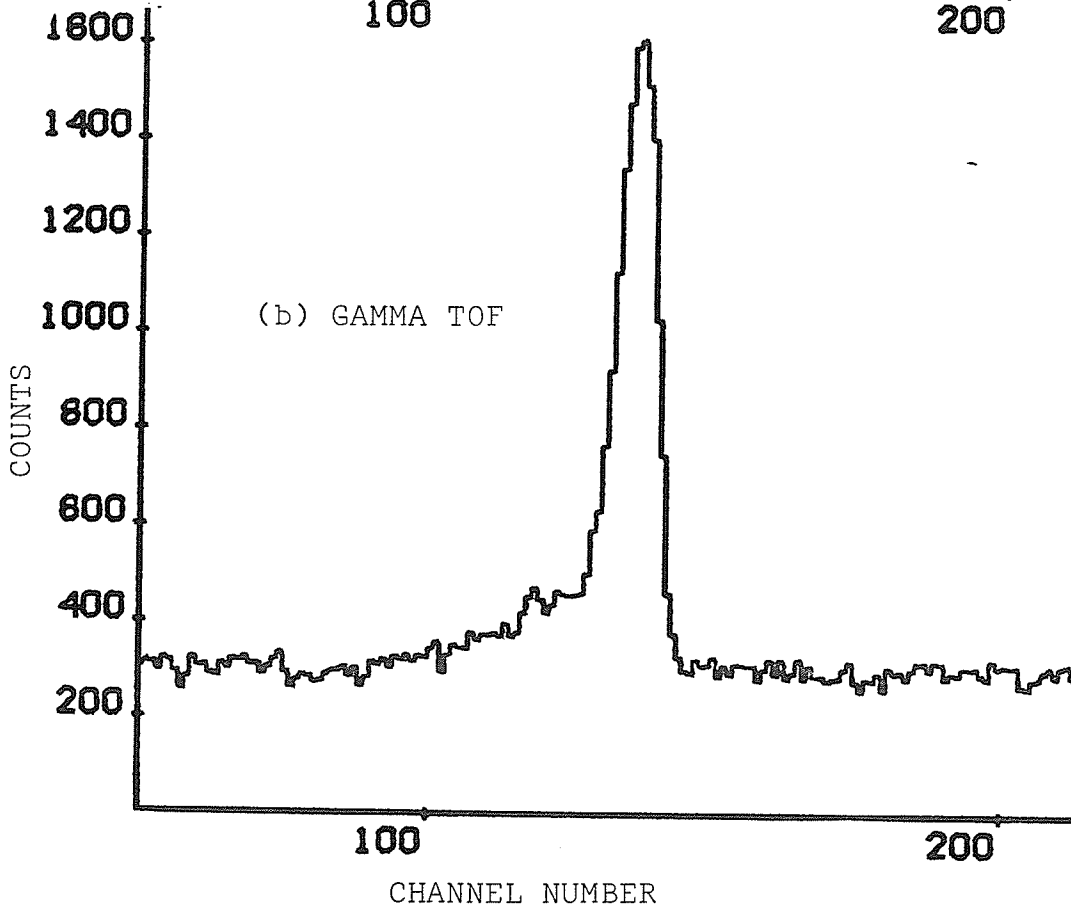
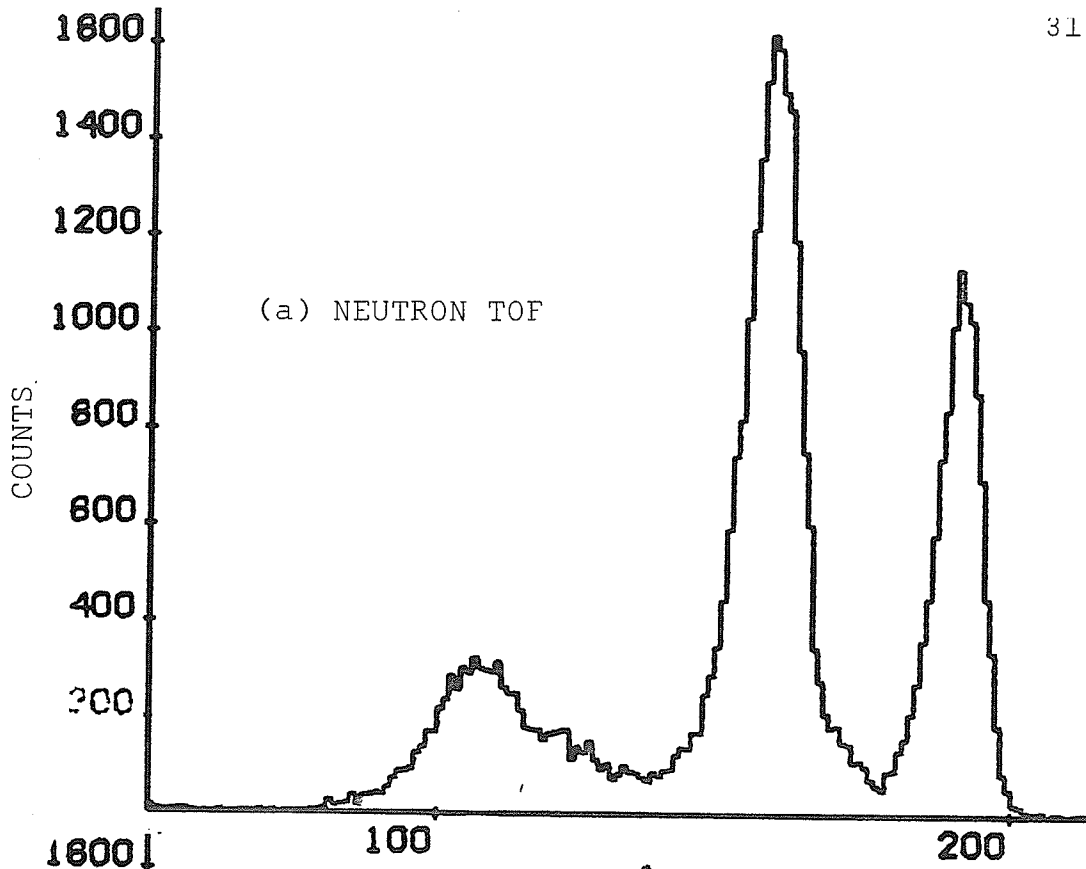
<sup>†</sup> This follows standard practice of starting on the signal having the lower count rate, hence reducing the number of false starts.

range of pulse heights, the neutron and gamma peaks appear smeared together and it is no longer possible to separate them completely. We have removed this problem by using a two dimensional PSD versus PH representation. In the PSD-PH plane the signals appear as two curved, but separated neutron and gamma "islands". Using the routine MULPAR the PSD-PH plane is displayed on a CRT and loci are drawn around the neutron and gamma islands using a light pen. These loci are then stored. The identification routine CMTPID is then able to sort the incoming events into different single parameter spectra depending on whether they fall within the neutron or gamma locus. Fig. 1-5 shows an example of the effectiveness of this method. Both spectra were taken at the same time with the same TAC. 1-5a is the spectrum of those TOF signals whose co-incident PH and PSD fell within the neutron locus in the PSD-PH plane and 1-5b those within the gamma locus. The scales are the same for a and b. Notice that there is no sign of gamma peaks leaking through into the neutron spectrum or neutrons into the gamma spectrum.

PH, PSD and TOF parameters were logged event by event on magnetic tape. In this way it was possible to "play back" any part of the experiment at a later date. This is useful to check for suspected gain shifts, to change loci, etc.

The time structure spectrum is derived from the NE111 in the same way as from the neutron detector. A

Fig. 1-5 Effectiveness of the n- $\gamma$  pulse shape discrimination. (a) neutron time of flight and (b) gamma time of flight taken from same TAC with neutron and gamma events sorted according to PSD. Note no evidence of gamma peak leaking through into neutron spectrum or vice versa.



pulse height window is set on the elastic peak and timing is only done on the elastic signals. As a precaution we adjusted the constant fraction discriminator (anode of time structure detector) to 0.5V and then set the photomultiplier high voltage just high enough for dependable triggering. As the elastic protons produce the largest pulse heights, this further ensures that timing is done only on the elastic peak. This should give the best possible timing.

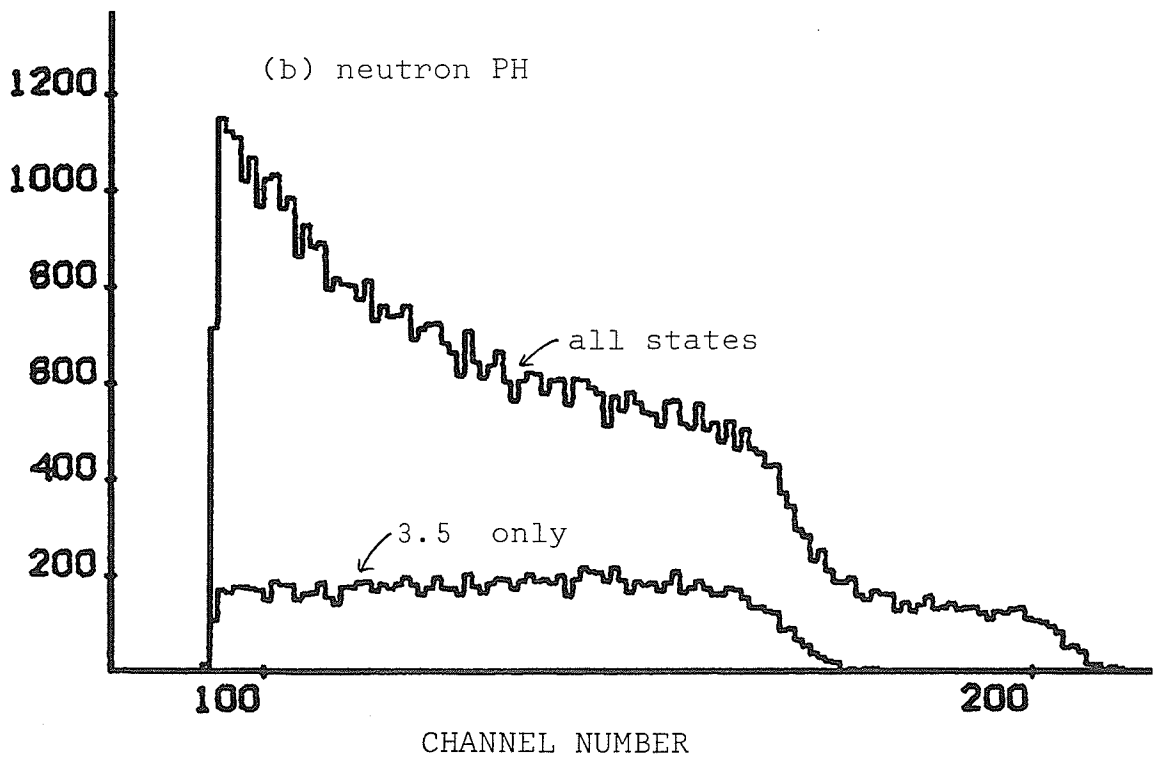
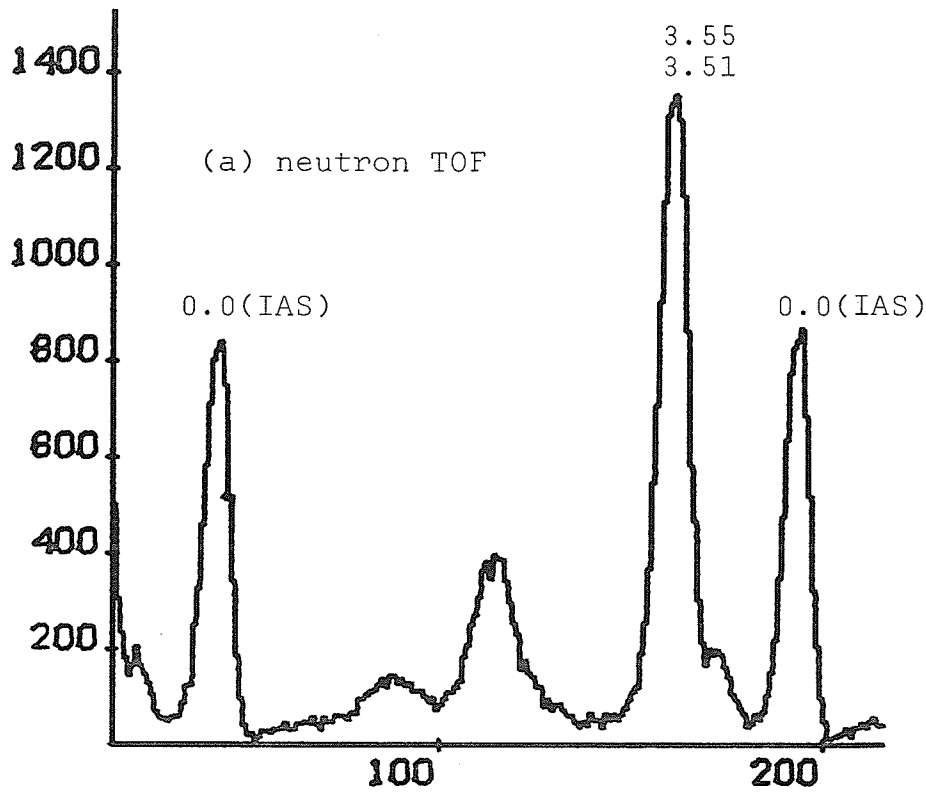
Signals from the NaI beam monitor are fed through the standard preamplifier and spectroscopy amplifier to the ADC. As with the CAMAC ADC, every event admitted to the ADC is counted by a scaler to allow later correction for deadtime.

### 1.3.2 Detector Thresholds

A monoenergetic beam of neutrons will produce a continuous distribution of pulse heights ranging from zero to some maximum value corresponding to the maximum recoil energy for that energy of neutron. Fig. 1-6a shows a neutron time of flight spectrum and the upper curve in 1-6b is the corresponding pulse height spectrum. Notice that a pulse height threshold has been set at channel 93 and pulses of lower amplitude than this do not appear. The lower curve in 1-6b is the pulse height distribution for the neutrons in the 3.55/3.51 MeV peak. Notice that this distribution falls to zero at around channel 175. If the pulse height threshold were raised to channel 175 then the

Fig. 1-6 Pulse height distributions.

The upper curve in (b) is the pulse height spectrum corresponding to the TOF spectrum in (a). Lower curve in (b) is the pulse height spectrum for the 3.55/3.51 peak only. To eliminate neutrons below a certain energy from the time of flight spectrum, the pulse height threshold is raised above the corresponding maximum pulse height for that neutron energy.



only peak remaining in the TOF spectrum would be the 0.0 ground state. As the PH threshold is lowered, more and more events appear to the left of the ground state. If the threshold is too low, low energy neutrons will overlap the ground state of the adjacent cycle. This situation is referred to as "wrap-around" and corresponds to slower neutrons from one beam burst arriving at the detector at the same time as the faster ground state group from the following beam burst. The detector pulse height threshold must be set just high enough to reduce the detection efficiency to zero for neutrons slow enough to wrap around. Such a setting eliminates wrap-around yet gives the maximum possible detection efficiency for the ground state group. Fig. 1-6 is an example of a good pulse height threshold. The low energy neutron spectrum just reaches zero in time for the next ground state group.

To produce a good clean lower cutoff, the pulse height threshold was set by means of the PH SCA (upper SCA Fig. 1-4). The anode CFD threshold was set to a value just lower than this. Sometimes, in an attempt to get maximum detection efficiency, the threshold was set too low and wrap-around occurred. Such runs were easily salvaged by playing back the logging tapes using a neutron locus cutting off at the required pulse height. It is possible to complete all runs with a low hardware threshold and have the PH thresholds imposed later by the locus. This, however, has

no clear advantage and merely uses up logging tape unnecessarily.

### 1.3.3 Technical Summary

Table 1-1 provides a convenient summary of the technical data for the  $^{13}\text{C}$  experiment. Some of the items in the table are discussed in more detail later.

Table 1-1 Technical data for the  $^{13}\text{C}(p,n_0)^{13}\text{N}$  experiment

## PROTON BEAM

current on target: 30 to 100 nA; 50 nA typical  
time between beam bursts: 35.11 ns  
width of burst: <1 ns FWHM  
energies used: 22.5, 25.8, 30.5, 37.2 MeV

## NEUTRON DETECTOR

NE213 liquid scintillator encapsulated in Nuclear Enterprises type BA-1 bubble free enclosure, inside dimensions 11.43 cm dia. x 12.7 cm thick.

photomultiplier: RCA 4522 operated grounded anode; typical overall voltage - 1800 V; timing from anode; linear signals from dynode 12

PH thresholds: 5 to 11 MeVee; efficiency during this experiment: from 7% to 12%

FLIGHT PATHS: 4 m to 6 m

ANGULAR RANGE:  $30^\circ$  to  $150^\circ$ ;  $10^\circ$  steps

OVERALL RESOLUTION (includes effects of beam burst width, electronic timing, detector thickness, target thickness, beam energy spread):

Variable, depending on "time tune", flight path and neutron energy - best  $\approx$  600 KeV  
worst  $\approx$  3 MeV  
typical  $\approx$  1 MeV

ELECTRONICS: standard NIM modules, mostly ORTEC

ADC'S: for main detector: EG & G/ORTEC AD811

8 parameter CAMAC ADC

for timing & beam monitor: Northern Scientific  
NS 625 dual 4096 ADC

COMPUTER: PDP-15/20

## 1.4 ANALYSIS AND RESULTS

In terms of measured quantities the desired (p,n) differential cross section is just

$$\frac{d\sigma}{d\Omega} = \frac{C N_{n_0} L^2}{N_{fc} I_{fs} t_{eff} \eta_d} \quad 1-14$$

where

$N_{n_0}$  = number of counts observed from the ground state neutron group.

$L$  = target to detector distance (flight path).  
( $L^2$  accounts for variation in solid angle with  $L$ .)

$N_{fc}$  = number of Faraday cup counts recorded by current integrator.

$I_{fs}$  = full scale current set on current integrator.

$t_{eff}$  = effective thickness of target. If target is rotated this goes up as  $1/\cos \theta$ .

$\eta_d$  = neutron detection efficiency for the ground state neutron group.

$C$  is a constant dependent on the number of atoms/g in the target, the detector area and the current integrator constant. If  $L$  is in metres,  $I_{fs}$  in nA and  $t_{eff}$  in  $\text{mg}/\text{cm}^2$  then for a target of  $^{13}\text{C}$ , an 11.43 cm dia. detector as used in this experiment and our Brookhaven Instruments current integrator (Coulomb/count = full scale Amps  $\times 10^{-2}$ ) one gets a value of  $C = 33.72$  to give  $\frac{d\sigma}{d\Omega}$  in mb/sr.

C may also be treated as a normalization constant and simply adjusted to normalize the measured cross sections to some trusted datum. This is the method of choice if target thickness or charge collection efficiency are not known accurately.

The other quantities in 1-14 are determined, often somewhat indirectly, from the measurements made during the experiment. Let us look at detector efficiency first.

#### 1.4.1 Neutron detection efficiency

Because neutrons are uncharged, they are not detected directly, but rather by means of the charged particles produced when they interact with hydrogen and carbon in the organic scintillator.<sup>†</sup> Knowing the composition of the scintillator and the light produced in it by the various charged particles, it is possible to calculate the fraction of incident neutrons that will produce a pulse height above threshold and hence be detected. Kurz (1964) produced a computer program to perform such a calculation analytically. Stanton (1971) re-worked the Kurz code in a Monte Carlo form. Some advantages of the direct Monte Carlo simulation were:

- 3rd and higher order scatterings automatically accounted for - important with large scintillators.

---

<sup>†</sup> for a detailed discussion of the mechanisms see the report by Stanton (1971)

- simulated pulse height spectrum available; this can be useful for comparison to observed PH spectra.
- much more flexible geometry; scintillators may be rectangular or cylindrical and user can control where and how the neutron beam enters the detector.

McNaughton (1974) improved the accuracy of the Stanton code by incorporating improved n-carbon data. Recently a group at Kent State (Cecil et al 1979) have reported further refinements to the code which result in improved predictions over a wide range of neutron energies and detector thresholds. The major changes are

- improved inelastic cross sections and kinematics for neutron induced reactions on  $^{12}\text{C}$ . This includes the addition of a  $\text{C}(n,2n)$  reaction channel.
- use of the latest light response functions. These give the light output as a function of energy for protons and alphas.
- use of relativistic kinematics.
- proper determination of the light produced by escaping charged particles. Previous codes assumed the light output from a given charged particle was independent of where in the scintillator the charged particle was produced. In fact, particles produced near an edge may escape and not give much light.

We have obtained a copy of the Kent State code and have used it to calculate neutron detection efficiencies.

The program provides a full simulation of the neutron detection process. It follows each neutron (and its products) scatter by scatter until they are lost or fall to a negligible energy. Seven interaction channels are provided - the (dominant at low energies) n-p channel and 6 n-Carbon channels, namely (n,n), (n,np), (n,2n) (n, $\gamma$ ), (n,3 $\alpha$ ) and (n, $\alpha$ ). The program simulates the intensity spectrum of light from the charged particles (pulse height spectrum) and calculates detection efficiency as a function of threshold. The calculations are believed accurate to a few percent, probably better in most cases (Cecil, 1979).

To calculate neutron detection efficiency the parameters of table 1-2 were used. The size, density and hydrogen to carbon ratio are self explanatory and were taken from the manufacturer's specifications. The neutron energy spread seems realistic for this experiment as estimated from typical values of the beam energy spread and energy loss in the target. It is not critical for the calculation of efficiencies. The light response function and pulse height resolution however require a bit of explanation.

The light response functions for protons and alphas are those recommended by Cecil (1979) for NE 213. They give the energy,  $T_e$ , of the stopping electron which would produce the same light output as the stopping heavier particle of energy  $T_p$ . The reason for converting to electron equivalent is that the light produced by a stopping electron increases



Table 1-2 Parameters used in the detector efficiency calculation.

- NE213 liquid scintillator, end-on cylinder, 11.43 cm diameter x 12.7 cm thick
- density: 0.874 g/cm<sup>3</sup>
- ratio of hydrogen to carbon atoms: 1.213
- light response function:

$$T_e = a_1 \left[ 1 - \exp(a_2 T_P^{a_3}) \right] + a_4 T_P$$

coefficients for NE213:

	<u>a<sub>1</sub></u>	<u>a<sub>2</sub></u>	<u>a<sub>3</sub></u>	<u>a<sub>4</sub></u>
protons:	-2.83	-.25	.93	.83
alphas:	-5.90	-.065	1.01	.41

- neutron energy spread: 0.7 MeV
- pulse height resolution: one photoelectron level  
= 0.005 MeVee

linearly with its energy while the light output from heavier particles (high ionization per unit path) does not. Because of the linear relationship between light output and electron energy, it is convenient (and standard practice) to express the light output for all particles in terms of MeV electron equivalent (MeVee).

Because of finite pulse height resolution the pulse height spectrum is somewhat more smeared than the theoretical light intensity spectrum. To simulate the resolution smearing, the program translates the energy deposited by a monoenergetic charged particle into a Gaussian pulse height distribution, the width of the distribution being determined by the number of photoelectrons released. This number depends on such things as the state of the reflector paint in the scintillator, coupling to the phototube and the photocathode itself. The more electrons released by the monoenergetic particle, the better defined will be the corresponding pulse height.

Fig. 1-7 shows the effect of pulse height resolution. "A" represents perfect resolution and a very small value of neutron energy spread. The pulse height cutoff is very sharp, reflecting only the small neutron energy spread. "B" is for a realistic neutron energy spread of 0.7 MeV, but a one photoelectron (p.e.) level of 0.1 MeV. This means that a 1.0 MeV electron (or a 1.0 MeVee proton) would release only  $1.0/0.1 = 10$  photoelectrons. The resulting

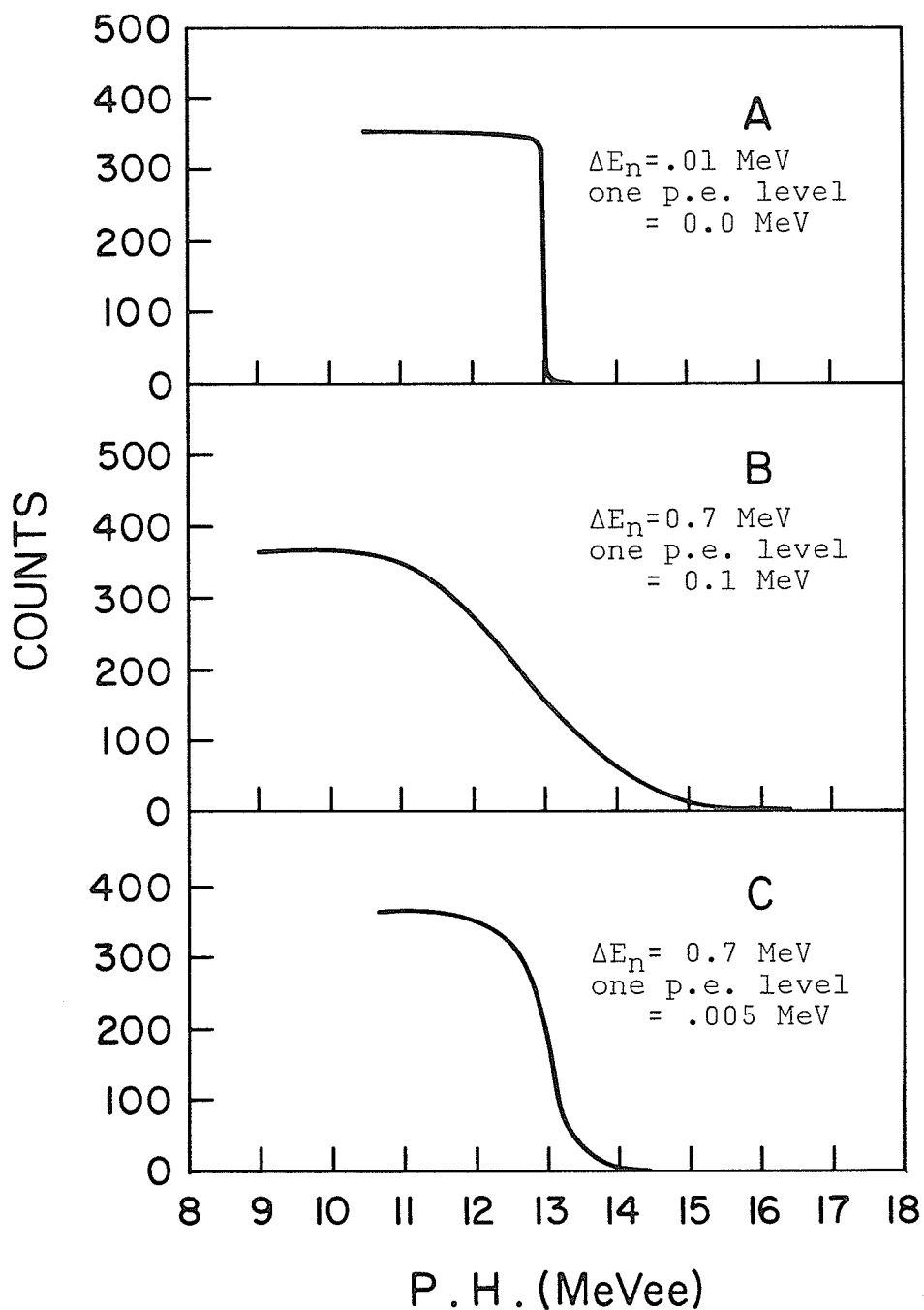


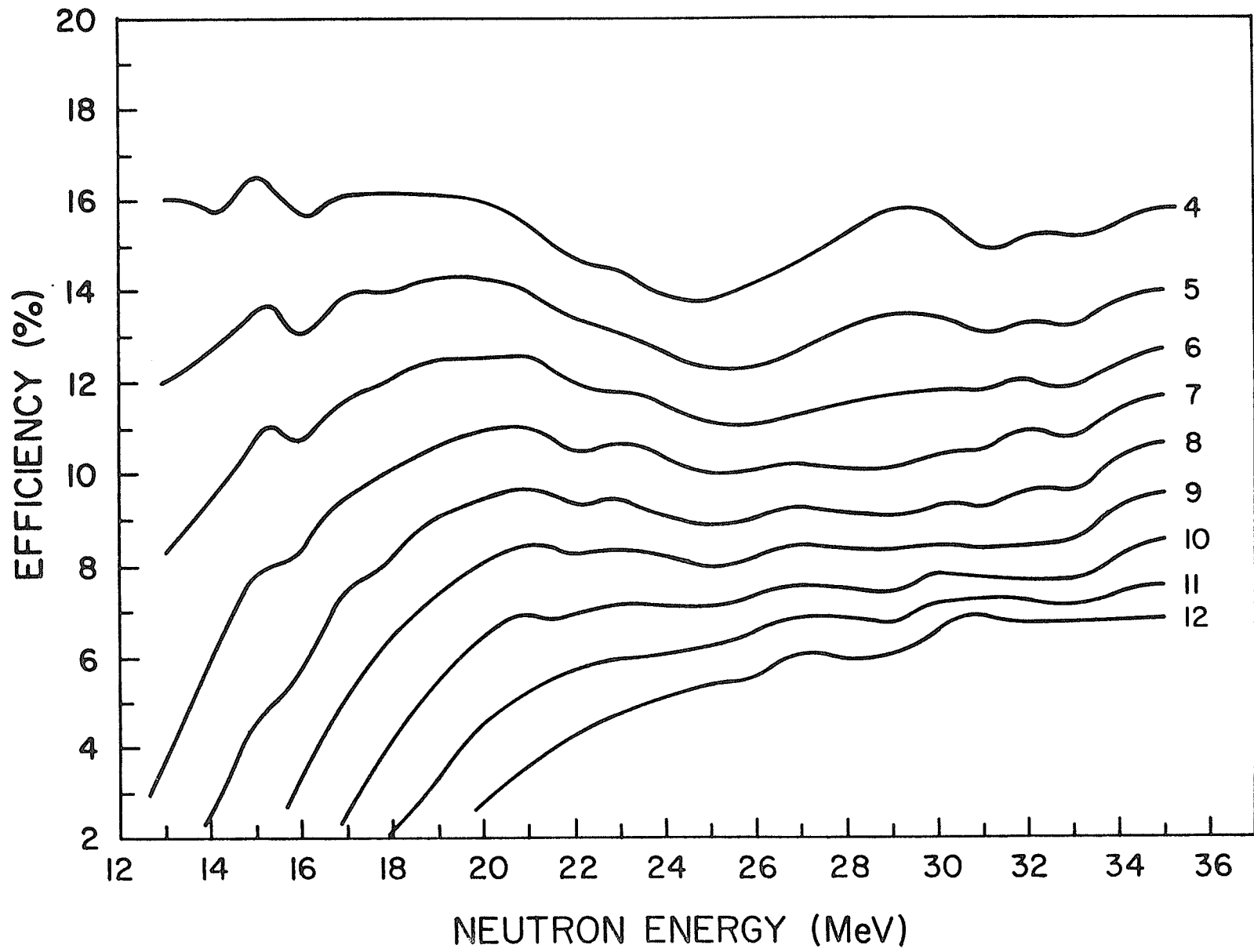
Fig. 1-7 Computer simulation of pulse height distributions. Shown is upper end of pulse height spectrum for 19.1 MeV neutrons, the energy of the  $^{13}\text{C}(p,n)^{13}\text{N}$  ground state group at  $30^\circ$  lab. angle and 22.5 MeV incident. Distribution "C" agrees with that observed experimentally. Pulse height bin width = 0.1 MeVee.

pulse height distribution is quite broad. By adjusting the one photoelectron level we were able to match the resolution smearing to that actually observed. "C" shows the result judged to best simulate the observed resolution. The indicated one photoelectron level of 0.005 MeVee (200 photoelectrons per MeVee) was used in the calculations of detector efficiency. Actually, the resolution value has a large effect on efficiency only for detector thresholds near the maximum pulse height. As our thresholds were never more than about 50% of maximum pulse height, our calculated efficiencies were not very sensitive to the assumed one photoelectron level.

Fig. 1-8 shows the detection efficiency calculated using the parameters of table 1-2. Calculations were made from 13 - 35 MeV to cover the neutron energy range of the experiment. Although Fig. 1-8 shows pulse height threshold in steps of one MeVee, steps of 0.1 MeVee are available on the computer printout.

To obtain the detection efficiency for any given run, the pulse height threshold in MeVee is required. Since the threshold level is plainly visible on each pulse height spectrum (see Fig. 1-6 for example) all that is required is to calibrate the spectra in terms of MeVee. The Compton distribution from a gamma source provides a convenient calibration point, at the level of about 1 MeV. We took a  $^{60}\text{Co}$  pulse height spectrum at least once for each PH gain

Fig. 1-8 Calculated neutron detection efficiency for 11.43 cm dia. by 12.7 cm thick NE 213. Graph shows efficiency as a function of neutron energy with pulse height threshold in MeVee as a parameter. Calculations were performed with the Kent State Monte Carlo program (Cecil, 1979) using the data of table 1-2.



setting used. This gives a distribution such as shown in Fig. 1-9 and the channel of the half height point on the right hand side of the Compton edge corresponds to 1.07 MeV.<sup>†</sup> As the detector thresholds used ranged from 5 - 11 MeVee, it was important to have calibration points at much higher pulse height than that provided by the  $^{60}\text{Co}$  Compton edge. Since the neutron energy is known from kinematics, the upper end of the neutron pulse height spectrum itself provides a convenient calibration. For every run we calculated the MeV electron equivalent of the ground state neutron group and then plotted these against channel number of the upper end of the pulse height distribution (taken to be half way down the tail). Several plots were prepared, one for each group of runs sharing the same pulse height gain setting. The results confirmed a linear relation between pulse height and MeVee and provided the required calibration. The degree of scatter of the data points about a true straight line permitted an estimate to be made of the uncertainty in efficiency resulting from the assignment of the pulse height

---

<sup>†</sup> Some workers (e.g. Watson et al, 1979) take the point at two thirds full height to correspond to maximum recoil electron energy. Others (e.g. Drosig, 1972) take the point at half height to correspond to 1.04 to 1.05 times this value. The  $^{60}\text{Co}$  spectrum results from gamma rays of equal intensity at 1.33 and 1.17 MeV. The value of 1.07 MeV for the half height of the composite Compton electron distribution is taken from Carlson et al (1972) and is consistent with both the above approaches.

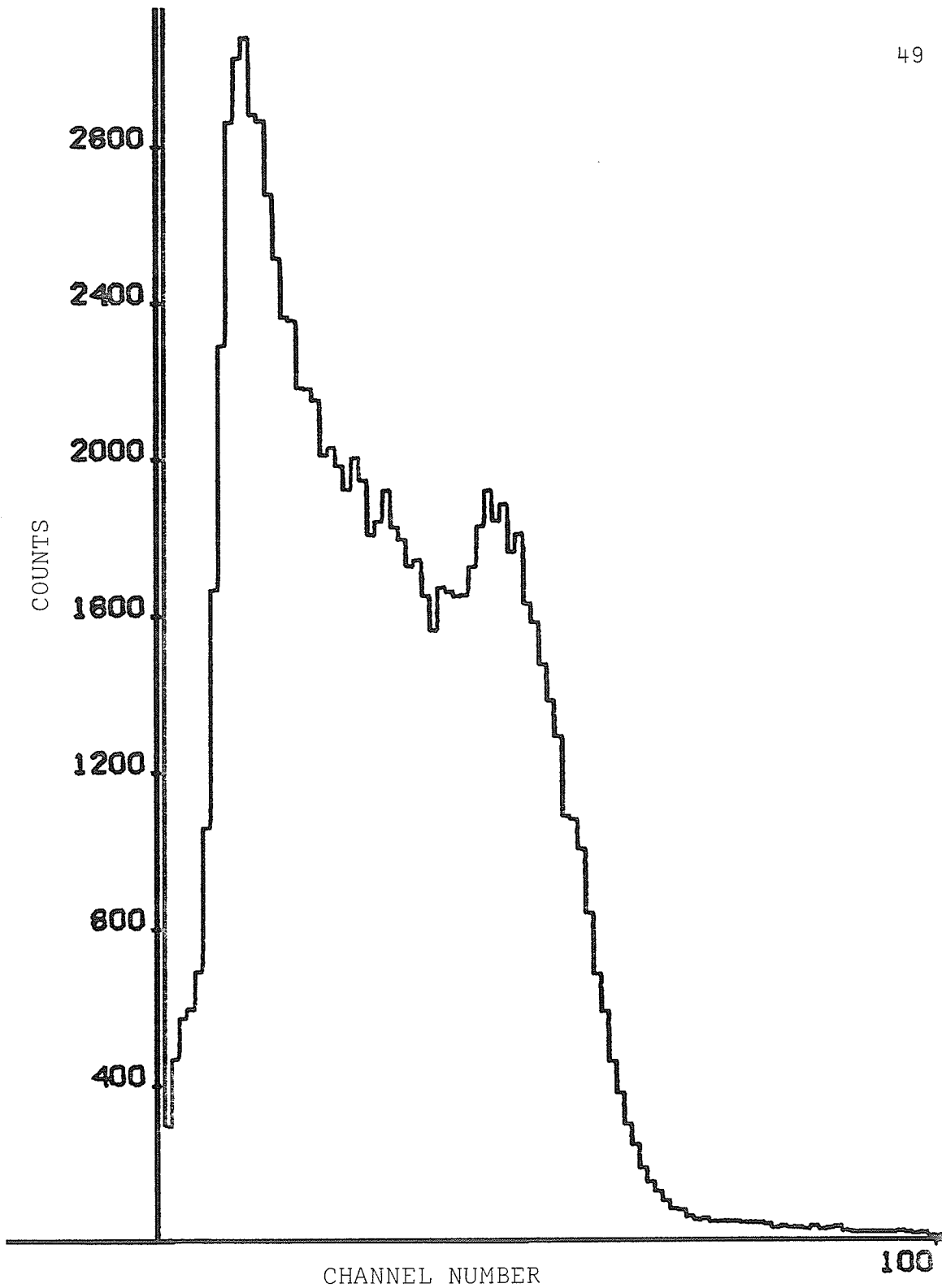


Fig. 1-9 Pulse height spectrum from  $^{60}\text{Co}$ .  
Shown is bottom end of 1024 channel spectrum.

threshold.

The detector efficiencies for the experiment were found to range from about 7% to 11%. The lowest detection efficiencies tend to be for long flight paths and high neutron energies, as in these cases high thresholds are required to prevent wrap-around.

#### 1.4.2 Extracting neutron yields

The neutron yield from (p,n) reactions to the isobaric analog state is determined by integrating the IAS peaks in the neutron time of flight spectra and subtracting the contributions of non-IAS neutrons such as room background, overlapping peaks, or neutron continua from the target. This was generally straightforward, as in most cases the peaks were well separated and the background very small.

It can be seen from Fig. 1-10 which shows a neutron spectrum with and without shadow bar, that neutrons not coming directly from the target make no significant contribution to the area of the ground state peak. The spectrum shown was taken at  $150^\circ$  where running times were long and the contribution from non-target neutrons would be relatively more significant. The spectrum taken with the shadow bar in place shows that non-target background is not significant. In fact the structure in the spectrum taken with the shadow bar in place is similar to the main spectrum and the counts observed probably come from incomplete shadowing or from "in-scattering" from the concrete block containing the

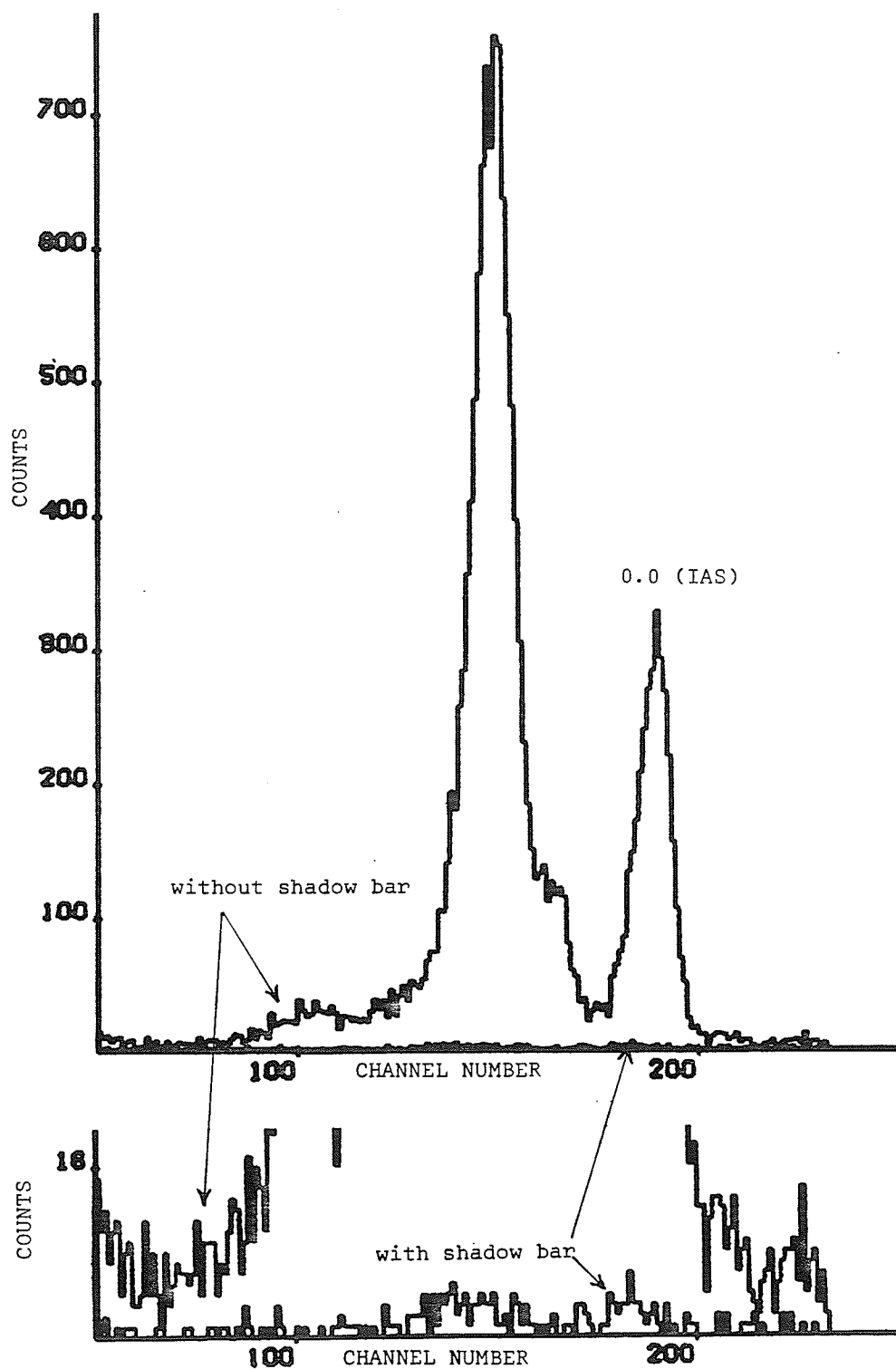
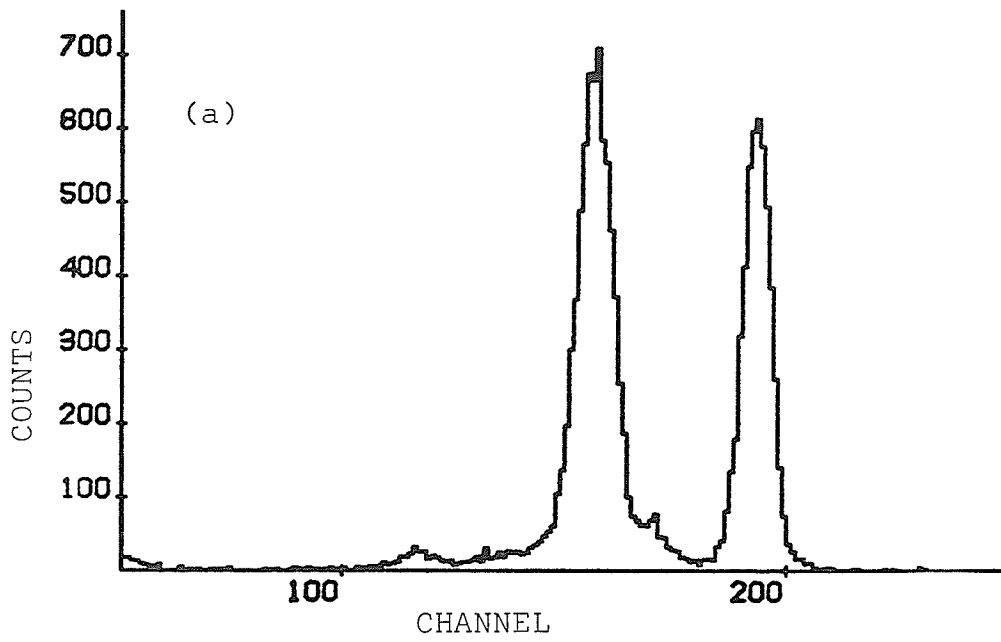


Fig. 1-10 Upper: neutron time of flight spectra taken for similar run times (2h:15m and 2h:08m) with and without shadow bar in place. Lower: lower part of the top spectrum shown with expanded vertical scale.

detector (the bar is placed so as to shadow only the detector, not the block). Such in-scattering is clearly not of sufficient magnitude to warrant special treatment.

On most of the time of flight spectra the peaks are well separated and no correction is required for peak overlap. In a few cases, particularly the runs at 37.2 MeV, some peak overlap has occurred. Examples of well separated and overlapping peaks are shown in Fig. 1-11. As the peaks have the same shape as the beam burst, which can be quite complex, it is difficult to unfold the peaks accurately by fitting them with an analytic shape. What was done therefore was to integrate the IAS peak using a simple "straight cut" and then to correct for the overlap. If the overlapping peaks have the same shape and size then the straight cut method will require no correction at all as the tail of the desired peak lost outside the cut is exactly compensated for by the tail of the overlapping peak that sticks inside the cut (if the peaks are symmetric). A correction only becomes necessary if the overlapping peaks are not the same size and shape. In cases like 1-11 (b) the IAS peak area obtained from a straight cut tends to be slightly high as more peak area is gained than is lost. To estimate the size of this correction the peaks were fitted as closely as possible with Gaussian shapes (Fig. 1-12) and then the area of the small peak as obtained using a straight cut integration was compared with the actual peak area. For the case shown in



### $^{13}\text{C}(p,n)^{13}\text{N}$ NEUTRON TOF

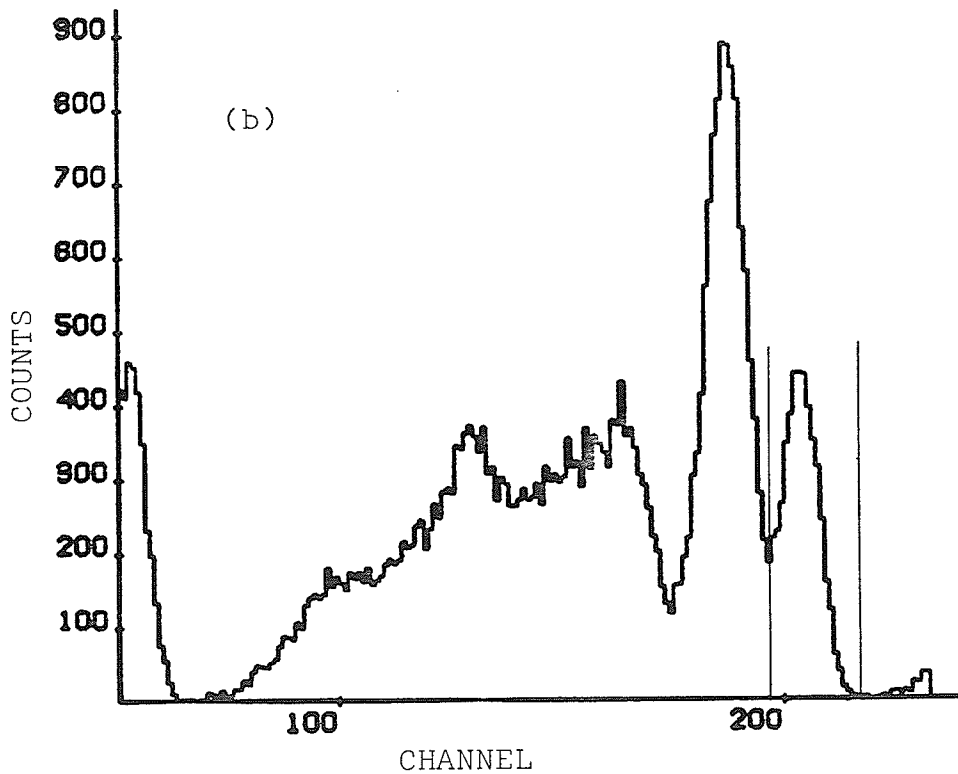


Fig. 1-11 Examples of (a) well separated and (b) overlapping peaks. The IAS peak area in (b) obtained by taking a straight cut as shown by the vertical lines is 3% too high.

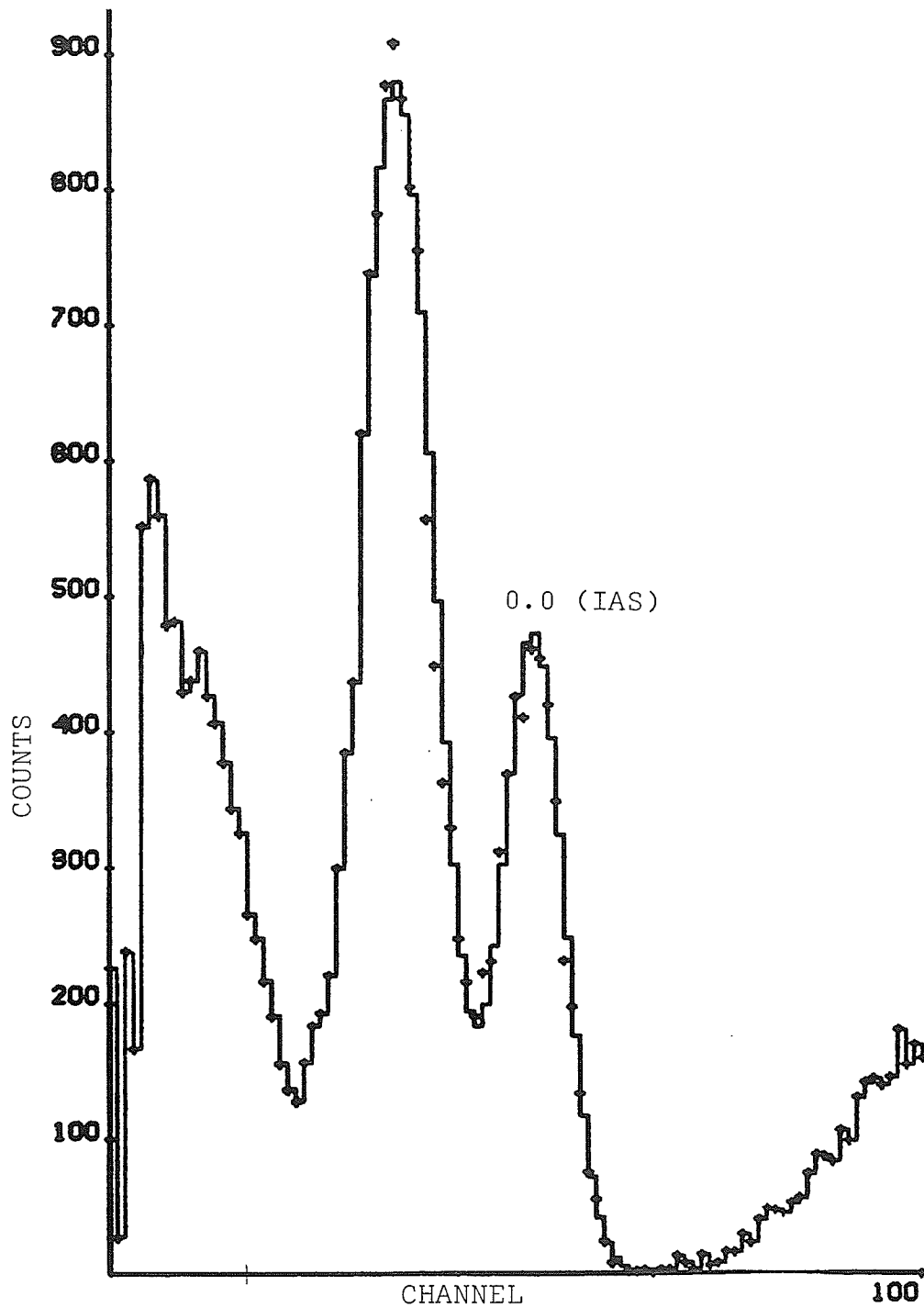


Fig. 1-12 Method of estimating overlap correction. The crosses are the data and the histogram a Gaussian fit. This procedure showed that the IAS peak area obtained from a "straight cut" had to be reduced by 3%.

Fig. 1-11 (b) the straight cut area was 3% too high. Even in the worst case observed the correction was only 8%.

#### 1.4.3 Normalization

The normalization presented some difficulty. For one thing the target was non-uniform. This was apparent from a visual inspection - the surface appeared flaky and irregular. During the experiment it was discovered that a crack had developed across the centre of the target. It is not known exactly when this happened. Further, when removing the target ladder it was noticed that some carbon had flaked off and was lying in the bottom of the chamber. To further complicate matters, the thick target caused enough beam blow-up that not all the beam was caught by the Faraday cup. An attempt was made to determine beam loss by measuring the ratio of Faraday cup current to stripping foil current with the target in and out, but no consistent quantitative measurement could be made. Values for the ratio of target out/target in, Faraday cup current ranged from a low of 1.12 to a high of 1.42, with the average value being around 1.2.

In view of all the above, it was decided to set the relative normalization according to the beam monitor and determine the absolute normalization from known (Lind et al, 1975) (p,n) cross sections at 22.8 MeV. The number of counts observed by the beam monitor is proportional to the integrated beam current (total charge), effective target

thickness, and elastic cross section at the angle of the beam monitor. Writing

$$N_{\text{bm}} \propto N_{\text{fc}} I_{\text{fs}} t_{\text{eff}} (d\sigma_{\text{pp}}/d\Omega),$$

the expression 1-14 for the (p,n) differential cross section becomes

$$\frac{d\sigma}{d\Omega} = \frac{K(d\sigma_{\text{pp}}/d\Omega)N_{\text{no}} L^2}{N_{\text{bm}} \eta_{\text{d}}} \quad 1-15$$

where K is a constant which sets the absolute normalization. The important thing about 1-15 is that the total charge,  $N_{\text{fc}}I_{\text{fs}}$ , and the effective target thickness,  $t_{\text{eff}}$ , do not appear explicitly. Normalizing to the beam monitor automatically corrects for the variation in target thickness and charge collection efficiency.

In order that a single normalization constant, K, suffice for the whole experiment, it was necessary to know the variation in elastic yield with energy. This was measured by performing a short experiment on the  $45^\circ$  R line (using the 71 cm scattering chamber shown in Fig. 1-1). Two 2mm thick semi-conductor detectors were used one behind the other with the outputs summed. They were placed at the same angle ( $59.7^\circ$ ) as the NaI beam monitor on the neutron chamber, and collimated to subtend a similar solid angle ( $1.87 \times 10^{-4}$  sr for  $45^\circ$ R tests,  $1.65 \times 10^{-4}$  sr for NaI beam monitor). A series of runs was made at the same four energies used in the (p,n) experiment. At the two highest energies a 2.6 mm

thick aluminum degrader was used in front of the detectors in order that the protons stop in the detector. At each beam energy six runs were made - one for each of four target angles (normal, reversed,  $10^\circ$  right,  $10^\circ$  left), one with the detector angle increased by  $5^\circ$  and one with the detector angle reduced by the same amount. Each run was made for 15,000 to 20,000 counts in the elastic peak. The measurements at  $\pm 5^\circ$  were made in order to estimate the effect of error in the angular position of the beam monitor.

For each run the number of counts in the elastic peak was measured, corrected for dead time and normalized to the Faraday cup charge. The relative elastic yield for different proton energies is shown in table 1-3. For all target positions the variation with energy agreed with table 1-3 to within the 0.7% to 0.8% statistical precision expected.

For any given energy the variation in yield with target angle was not as  $1/\cos \theta$ . The departure from  $1/\cos \theta$  dependence was as much as 6%. This was probably due to the beam hitting a slightly different place on the non-uniform target as the ladder was rotated.

#### 1.4.4 Error Summary and Results

The statistical error was kept to about 1% except for a few runs at 37.2 MeV where it was as high as 2.5% because of running time limitations.

Operator error (uncertainty in assigning the back-

Table 1-3 Dependence of beam monitor yield on energy.

<u>proton energy</u>	<u>relative elastic yield at 59.7<sup>0</sup></u>
22.5	1.000
25.8	0.943±.011
30.5	0.887±.011
37.2	0.649±.008

ground and the integration limits for the peaks) was estimated by taking extreme values and is limited to about 2%.

Peak overlap contributed less than 1% error except for several spectra at 37.2 MeV where the uncertainty in the overlap correction introduced an error of as much as 3%.

Deadtime was very small ( $\approx 1\%$ ) and deadtime errors are estimated as zero after correction.

The basic detection efficiency calculation is believed accurate to 5%, but uncertainty in determining the detector threshold in MeVee contributed an additional error. The uncertainty in detector threshold was estimated from the scatter of points on the MeVee vs channel number plots. The effect of an error in detector threshold on calculated efficiency is most serious if the threshold is near the maximum pulse height. In fact, to a good approximation,

$$\frac{\Delta\eta}{\eta} \approx \left( \frac{f}{1-f} \right) \frac{\Delta B}{B}$$

where  $f$  is the threshold expressed as a fraction of maximum pulse height and  $\Delta\eta/\eta$  and  $\Delta B/B$  are the fractional errors in efficiency and threshold respectively. Our errors in detector threshold were found to range from 1% to 4% (of the threshold in MeVee). The resultant relative error in detection efficiency was up to 7%, but more typically around 3% or 4%.

Errors in relative normalization using the beam monitor are believed to be small. The statistical errors

are insignificant and the main source of uncertainty is operator error in extracting the peak areas. As with the neutron spectra, this is limited to about 2%.

The angular position of the beam monitor is known to  $\frac{1}{2}^{\circ}$ . Based on the variation in cross section with angle that was measured during the experiment in the 71 cm chamber, it is estimated that this contributes a systematic uncertainty of no more than 2%.

The angular distribution at 37.2 MeV had to be normalized to the Faraday cup because of electronic problems with the beam monitor. Once that problem was resolved, points at  $30^{\circ}$ ,  $80^{\circ}$ ,  $90^{\circ}$  and  $110^{\circ}$  were taken again using the beam monitor. The run without the beam monitor could then be normalized to the Faraday cup using the same average ratio of Faraday cup to beam monitor readings. As a result of this procedure, the relative normalization of the 37.2 MeV points is uncertain to about 8% (based on the departure from a linear relation between beam monitor and Faraday cup for the runs during which the beam monitor was working).

Flight paths were measured to 1 cm which would mean a solid angle error of  $\pm 1.5\%$  at 4 m.

Laboratory angles of the neutron detector were surveyed to  $0.5^{\circ}$ .

Results of the data analysis are presented in Fig. 1-13. The error bars include all the sources of error mentioned in this section. The absolute normalization is good

to  $\pm 20\%$  which is the accuracy of the reference data (Lind et al 1975). The data are presented in tabular form in table 1-4.

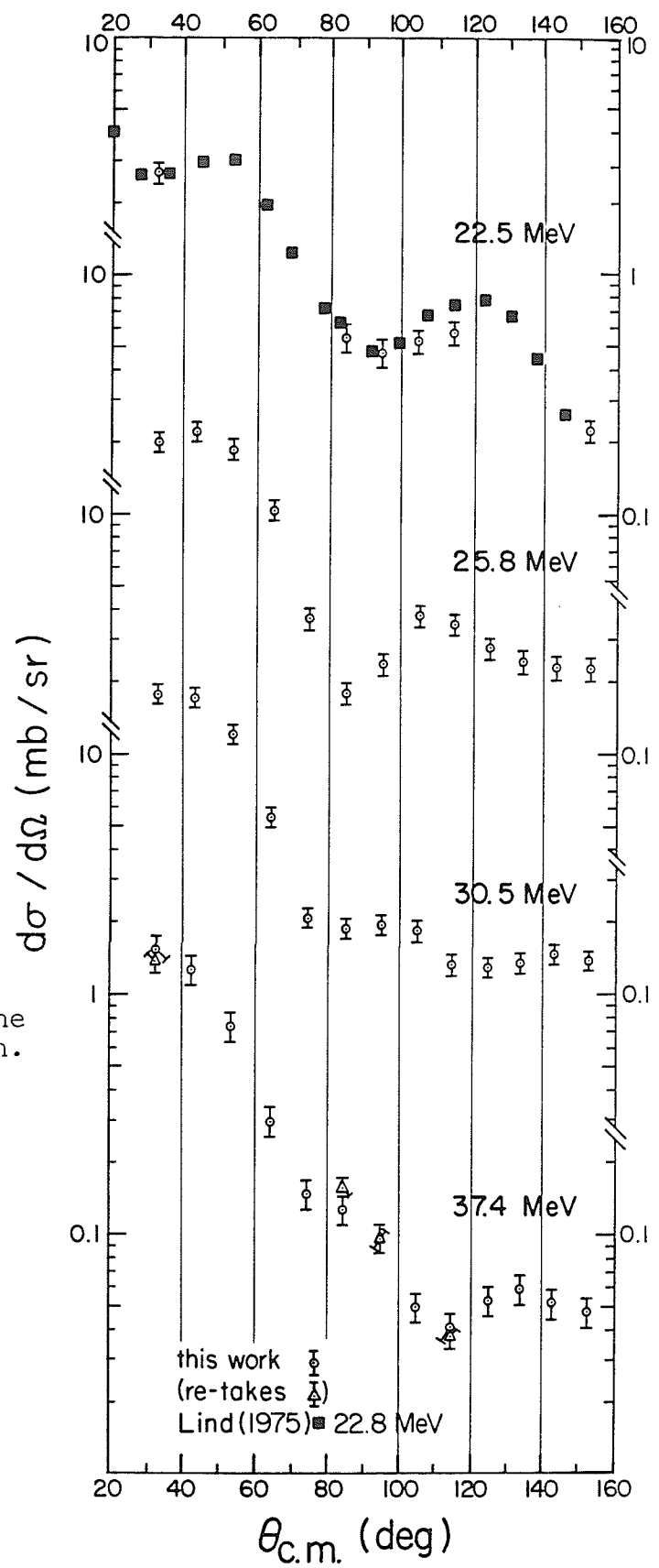


Fig. 1-13 Measured cross sections for the  $^{13}\text{C}(p,n_0)^{13}\text{N}$  reaction.

this work  
(re-takes  
Lind (1975)  $\blacksquare$  22.8 MeV

proton $\theta_{cm}$ energy (deg.)	22.5 MeV	25.8 MeV	30.5 MeV	37.2 MeV
32.4	2.70(29)	2.00(20)	1.80(16)	1.51(21)
43.1		2.19(22)	1.71(15)	1.26(18)
53.7		1.84(18)	1.21(11)	.74(10)
64.2		1.02(10)	.549(49)	.292(41)
74.5		.369(37)	.208(19)	.146(20)
84.8	.544(70)	.180(18)	.187(18)	.126(18)
94.8	.433(63)	.236(24)	.194(19)	.096(13)
104.7	.530(56)	.378(38)	.186(19)	.0497(70)
114.5	.574(63)	.349(35)	.132(13)	.0410(57)
124.2		.274(27)	.130(12)	.0524(73)
133.7		.242(27)	.135(12)	.0583(82)
143.1		.228(25)	.147(13)	.0506(71)
152.4	.223(23)	.225(26)	.138(12)	.0468(66)

Table 1-4 Measured differential cross sections for the  $^{13}\text{C}(p,n_0)^{13}\text{N}$  reaction. Entries in the body of the table are in mb/sr. Figures in brackets give the relative uncertainty in the last two digits of the number quoted.

## 1.5 LANE MODEL CALCULATIONS

1.5.1 Form of the Potential

A Lane model consistent analysis is one in which the potentials for (p,p), (p,n)IAS, and (n,n) are related by

$$U = U_0 + \frac{4(\vec{t} \cdot \vec{T})}{A} U_1 \quad . \quad 1-2$$

Lane consistent potentials for a  $T=\frac{1}{2}$  target such as  $^{13}\text{C}$  have been shown explicitly in equations 1-7. The importance of using only potentials that satisfy these relations rigorously has been emphasized by Cotanch and Robson (1973 a). They point out that some early analyses used potentials that were not Lane consistent and hence did not conserve isospin for the strong interaction.

Because of the relationships (1-7) among the different potentials, knowledge of any two,  $(U_p, U_1)$ ,  $(U_0, U_1)$  or  $(U_p, U_n)$ , for example, completely determines the potential. Another representation that is sometimes used is  $(U_<, U_>)$ . This form is based on the fact that for  $t=\frac{1}{2}$ , only two values of total isospin are possible for the nucleon nucleus system:

$$T_< = |T - \frac{1}{2}| \quad (T \text{ lower state})$$

$$\text{and} \quad T_> = T + \frac{1}{2} \quad (T \text{ upper state}).$$

$U_<$  and  $U_>$  refer to the potentials in these two states of good total isospin.<sup>†</sup>

---

<sup>†</sup> The product states of 1-5a and 1-5b may be expanded in terms of states of good total isospin. For a  $T=\frac{1}{2}$  target the only possible values of total isospin are  $T_t=0$  or  $T_t=1$ . Since

The potentials in the  $T_<$  and  $T_>$  states are (e.g. Satchler, 1969)

$$U_< = U_0 - \frac{2(T+1)}{A} U_1 \quad 1-15a$$

$$U_> = U_0 + \frac{2T}{A} U_1 \quad 1-15b$$

where it should be remembered that  $U_0$  is negative and  $U_1$  positive. This means  $|U_<| > |U_>|$ .

The version of TWAVE used, parameterizes the real part of  $U$  in terms of  $V_0$  and  $V_1$  but the imaginary part in terms of  $W_<$  and  $W_>$  ( $V$  refers to the real part and  $W$  to the imaginary). It is argued by Cotanch (1973) that this forces the user to apply the Lane model correctly.

Conversion from one representation to another can be made with strict Lane model consistency as shown in Table 1-5. Note that this table is specifically for the case of a  $T=\frac{1}{2}$  target and involves absolute values only.

The normal radial forms of the potentials are volume (Woods-Saxon) for the real part and volume plus surface

---

both the proton-core and neutron-analog systems have  $T_{3,t}=0$ , they can be expressed as linear combinations of  $T_t=0$  ( $T_<$ ) and  $T_t=1$  ( $T_>$ ) with projection  $T_{3,t}=0$ . Inserting the appropriate Clebsch-Gordan coefficients gives (coupling in the order  $T,t$ )

$$|pC\rangle = |\frac{1}{2}, \frac{1}{2}\rangle |\frac{1}{2}, -\frac{1}{2}\rangle = \frac{1}{\sqrt{2}} |1,0\rangle + \frac{1}{\sqrt{2}} |0,0\rangle$$

$$|nA\rangle = |\frac{1}{2}, -\frac{1}{2}\rangle |\frac{1}{2}, \frac{1}{2}\rangle = \frac{1}{\sqrt{2}} |1,0\rangle - \frac{1}{\sqrt{2}} |0,0\rangle$$

given: wanted	$(U_p, U_1)$	$(U_0, U_1)$	$(U_>, U_<)$
$(U_p, U_1)$	$U_p = U_p$ $U_1 = U_1$	$U_p = U_0 + \frac{U_1}{A}$ $U_1 = U_1$	$U_p = \frac{1}{2}(U_< + U_>)$ $U_1 = \frac{A}{4}(U_< - U_>)$
$(U_0, U_1)$	$U_0 = U_p - \frac{U_1}{A}$ $U_1 = U_1$	$U_0 = U_0$ $U_1 = U_1$	$U_0 = \frac{1}{4}(U_< + 3U_>)$ $U_1 = \frac{A}{4}(U_< - U_>)$
$(U_>, U_<)$	$U_> = U_p - \frac{2U_1}{A}$ $U_< = U_p + \frac{2U_1}{A}$	$U_> = U_0 - \frac{U_1}{A}$ $U_< = U_0 + \frac{3U_1}{A}$	$U_> = U_>$ $U_< = U_<$

Table 1-5 Table shows the relation between the ABSOLUTE VALUES of the potentials in the three most common Lane consistent representations. It assumes  $U = U_0 + 4(\vec{t} \cdot \vec{T})U_1/A$  and also that  $|t| = \frac{1}{2}$  (nucleon) and that  $|T| = \frac{1}{2}$  (mirror nucleus).

peaked (Woods-Saxon derivative) for the imaginary part.

Explicitly:

$$V_0(r) = -V_0 f_0 \quad 1-16a$$

$$V_1(r) = V_1 f_1 \quad 1-16b$$

$$W_{<}(r) = -W_{<V} f_{<V} + W_{<S} 4a_{<S} \frac{df_{<S}}{dr} \quad 1-16c$$

$$W_{>}(r) = -W_{>V} f_{>V} + W_{>S} 4a_{>S} \frac{df_{>S}}{dr} \quad 1-16d$$

$$\text{where } f_i = \frac{1}{1 + e^{a_i \frac{r - R_i}{r - R_i}}} ; R_i = r_i A^{1/3} \quad 1-17$$

and  $V_0, V_1, W_{<V}, W_{<S}, W_{>V}, W_{>S}$  are positive numbers. At the option of the user  $V_1(r)$  can be chosen to have a surface form,

$$V_1(r) = -V_1 4a_1 \frac{df_1}{dr} \quad 1-18$$

and if desired the surface peaked imaginary terms can be chosen to have the Gaussian form

$$W_s e^{-\left(\frac{r-R}{a}\right)^2} \quad 1-19$$

rather than Woods-Saxon derivative.

The spin orbit potential is taken to have a Thomas form

$$V_{SO}(r) = V_{SO} \frac{\chi_\pi^2 \langle \vec{l} \cdot \vec{\sigma} \rangle}{r} \frac{df_{SO}}{dr} \quad 1-20$$

where  $\chi_\pi^2 = 2.0 \text{ fm}^2$  is the pion Compton wavelength squared and the spin-orbit strength  $V_{SO}$  is entered in terms of a spin-orbit strength parameter,  $\lambda_{SO} = 180.8 V_{SO}/V_0$  where  $V_0$  is the strength (in MeV) of the real isoscalar potential.

The Coulomb potential is taken to be that of a

uniformly charged sphere of radius  $R_c = r_c A^{1/3}$ :

$$U_c(r) = \frac{ze^2}{2R_c} \left[ 3 - \left( \frac{r}{R_c} \right)^2 \right] \quad r \leq R_c \quad 1-21a$$

$$= \frac{ze^2}{r} \quad r > R_c \quad 1-21b$$

where  $e^2 = 1.440 \text{ MeV fm}$ .

### 1.5.2 Determining parameters of the Potential

Various approaches exist to deducing the Lane potential from experimental data. One way is to adjust  $U_1$  to fit (p,n) IAS data and adjust  $U_0$  so that the resulting proton potential duplicates a potential already known to describe (p,p) elastic scattering. It has been argued by Lovas (1976) that the proton potential used in such an analysis should be "global" and not individually fitted. Lovas found that fitting both (p,p) and (p,n) differential cross sections for an individual nucleus resulted in a potential that was unable to describe the (n,n) data.

Examples of the use of global proton potentials and (p,n) IAS differential cross sections to determine the Lane potential are the work of Carlson, Zafiratos and Lind (1975) and of Patterson, Doering and Galonsky (1976). Both groups adjusted  $U_1$  to fit (p,n) IAS differential cross sections while constraining  $U_p$  to reproduce the Becchetti-Greenlees (BG) global proton potential (Becchetti and Greenlees, 1969). Their approaches to fitting the (p,n) data were, however, different.

Carlson et al found that the shape of the (p,n) angular distribution was most sensitive to the radius and diffuseness,  $r_{1I}$  and  $a_{1I}$ , of the surface peaked, imaginary part of  $U_1$ . Consequently they assumed an arbitrary normalization and adjusted  $r_{1I}$  and  $a_{1I}$  to best fit the shape of the angular distribution. The rest of the geometry parameters were fixed at Becchetti-Greenlees values and the strengths  $W_1$  and  $V_1$  were fixed at values implied by the N-Z/A dependent terms in the BG potential ( $V_1=24$  MeV,  $W_1=12$  MeV). Once the best fit to the shape was found they then assumed that both  $V_1$  and  $W_1$  would have to be multiplied by the square root of the scale factor required to obtain the correct normalization. The ratio  $V_1/W_1$  stayed at 2. They presented a smoothed parametrization of best fit  $U_1$  for 22 nuclei from  $^{40}\text{Ar}$  to  $^{165}\text{Ho}$  at an energy of 22.8 MeV.

Rather than adjust geometry parameters to fit the shape of the (p,n) IAS angular distribution, Patterson et al fixed all the geometry parameters at Becchetti-Greenlees values and adjusted the isovector strength parameters to give a least squares fit to the data. They fitted (p,n) data between 25 and 45 MeV for targets from  $^{48}\text{Ca}$  to  $^{208}\text{Pb}$  and deduced an energy dependent Lane potential that is reasonably successful in reproducing (p,p), (p,n) IAS, and (n,n) scattering over a wide mass and energy range.

It is tempting to see how well the "universal" Lane potential of Patterson, Doering and Galonsky reproduces our

$^{13}\text{C}$  (p,n) data. Table 1-6 shows  $^{13}\text{C}$  Lane model parameters for the four proton energies for which we have data. The values in the table are calculated using parameter set "B" of Patterson et al. This is the set they rated as "best overall".

Fig. 1-14 shows the results of Lane model calculations made with TWAVE using the above potential as input. Agreement with the data is not very good. General features and trends are reproduced in a qualitative way but quantitative agreement, particularly at backward angles, is poor.

It is not surprising that this potential should fail to give a good description of the  $^{13}\text{C}(p,n)^{13}\text{N}$  quasielastic data. Firstly the potential was formulated by fitting (p,n) data for nuclei from  $^{48}\text{Ca}$  to  $^{208}\text{Pb}$ . Further, it is constrained to reproduce the Becchetti-Greenlees proton potential which was not intended for nuclei under  $A=40$ .

Although no global Lane model analysis has been done for the lighter nuclei, Watson et al. (1969) produced an optical model potential giving a good description of proton and neutron elastic scattering on 1p-shell nuclei over the energy range 10 to 50 MeV. The parameters judged by Watson et al to fit the data best are shown in table 1-7. The real part has a Woods-Saxon (volume) form and the imaginary part is Woods-Saxon derivative (surface) plus Woods-Saxon (volume) as indicated by  $W_s$  and  $W_v$  respectively. The spin orbit

$E_p$ (MeV)	$V_0$	$W_{<v}$	$W_{<s}$	$\lambda_{so}$	$V_1$	$W_{>v}$	$W_{>s}$
22.5	49.42	2.98	7.97	22.68	17.7	2.98	4.30
25.8	48.37	3.71	7.01	23.17	17.7	3.71	3.65
30.5	46.86	4.74	5.64	23.92	17.7	4.74	2.73
37.2	44.72	6.22	3.68	25.07	17.7	6.22	1.41

Geometry parameters  $r_R=1.17$ ,  $a_R=0.75$ ,  $r_I=1.32$ ,  $a_I=.56$ ,  $r_{so}=1.01$ ,  $a_{so}=0.75$ ,  $V_{so}=6.2$

Table 1-6 Lane model potentials taken from the global parameterization of Patterson et al. (1976). Lengths are in fm and strengths in MeV. The numbers in this table are from the preferred parameter set, set "B".  $|W_{<}| = |W_0| + 3|W_1|/A$  and  $|W_{>}| = |W_0| - |W_1|/A$ .

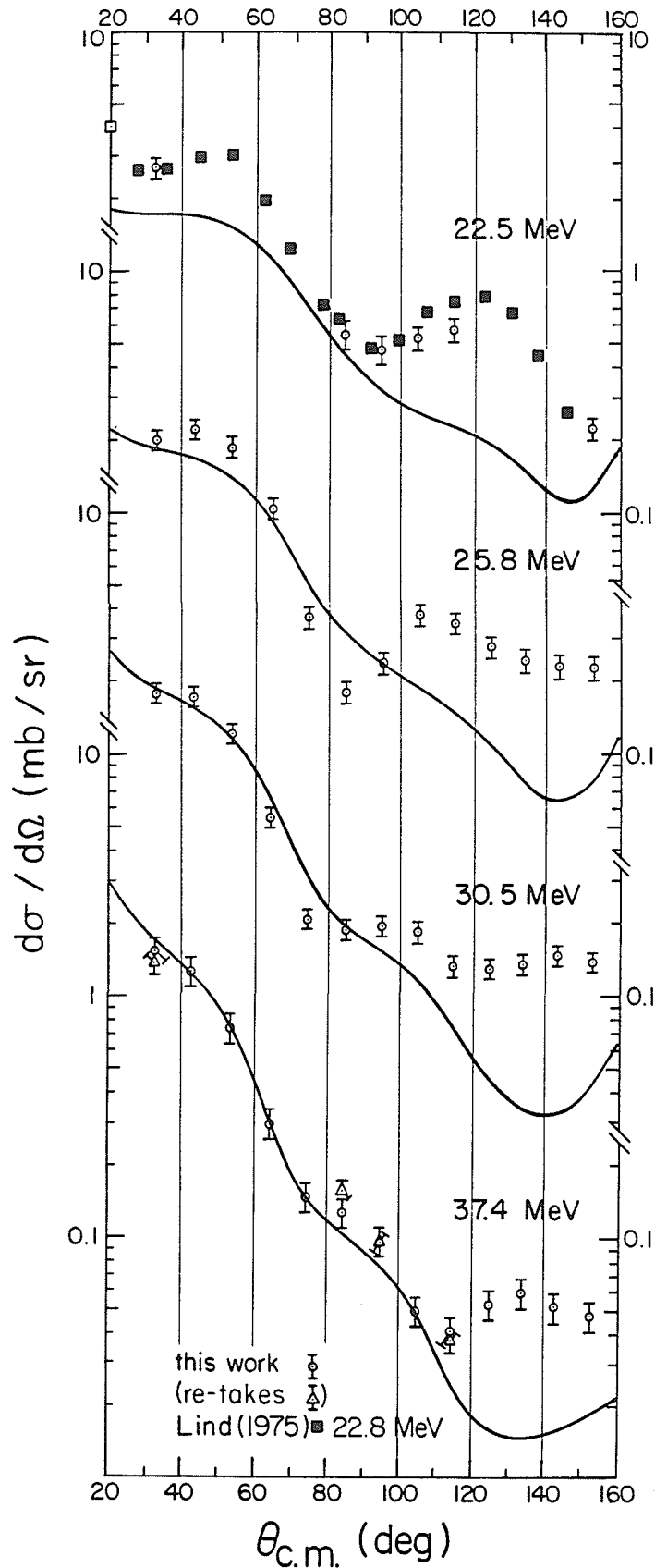


Fig. 1-14 Results (solid lines) of calculations using the "universal" Lane potential of Patterson et al.

$$V_R = 60.0 + 0.4(Z/A^{1/3}) \pm 27.0 [(N-Z)/A] - 0.3 E_{cm},$$

$$V_{SO} = 5.5,$$

$$r_R = r_I = r_{SO} = r_C = 1.15 - 0.001 E_{cm},$$

$$a_R = a_{SO} = 0.57, a_I = 0.5,$$

$$W_S = W_S(E) \pm 10.0(N-Z)/A,$$

$$W_V = W_V(E),$$

$$W_S = 0.64 E_{cm}, \quad \text{for } E_{cm} < 13.8$$

$$= 9.60 \text{ MeV} - 0.06 E_{cm}, \quad \text{for } E_{cm} \geq 13.8 \text{ MeV}$$

$$W_V = 0, \quad \text{for } E_{cm} < 32.7 \text{ MeV}$$

$$= 1.15 (E_{cm} - 32.7 \text{ MeV}), \text{ for } 32.7 \leq E_{cm} \leq 39.3 \text{ MeV}$$

$$= 7.5 \text{ MeV} \quad \text{for } E_{cm} > 39.3 \text{ MeV}$$

Table 1-7 The Watson 1p-shell optical potential. Lengths are in fm, potentials and energies in MeV. Where  $\pm$  appears, + is for protons and - for neutrons.

potential has the form

$$V_{so}(r) = V_{so} \frac{\lambda^2 \langle \vec{l} \cdot \vec{\sigma} \rangle}{R_{so}} \frac{df_{so}}{dr} \quad 1-22$$

which is the same as the Thomas form 1-20 except  $r$  in the denominator has been replaced by  $R_{so} = r_{so} A^{1/3}$ . Watson did this so  $V_{so}(r)$  would not lose its surface peaked character for light nuclei.

One can infer a trial Lane potential from the Watson 1p-shell potential by taking  $U_1$  as the  $(N-Z)/A$  dependent part of the potential and choosing  $U_0$  such that the resultant  $U_p$  reproduces the Watson proton potential.  $U_1$  may then be adjusted to best fit the  $(p,n)$  IAS data while still constraining  $U_p$  to reproduce the Watson 1p-shell proton potential.

Trial Lane potentials inferred from the Watson 1p-shell potential are shown in Table 1-8 and the results of Lane model calculations using this potential are shown in Fig. 1-15. Agreement with the data is noticeably better than for the calculations performed using the Patterson Lane potential. It is evident, however, that although the general slope and vertical normalization is good, more structure is required. This indicates that adjustment to the geometry of  $U_1$  must be made. Changes to the strength parameters  $V_1$  and  $W_1$  can only alter the normalization or

$E_p$ (MeV)	$V_o$	$W_{<v}$	$W_{<s}$	$\lambda_{so}$	$V_1$	$W_{>v}$	$W_{>s}$	$W_{1s}$
22.5	54.72	0.0	10.66	18.17	27	0.0	7.58	10
25.8	53.82	0.0	10.47	18.48	27	0.0	7.39	10
30.5	52.52	0.0	10.21	18.93	27	0.0	7.13	10
37.2	50.62	2.12	9.84	19.64	27	2.12	6.76	10

geometry parameters  $r_R = r_I = r_{so} = r_c = 1.12$ ,  $a_R = a_{so} = 0.57$ ,  $a_I = 0.5$   
 $V_{so} = 5.5$

Table 1-8 Lane model potentials inferred from the 1p-shell optical potential of Watson et al. (see Table 1-7).

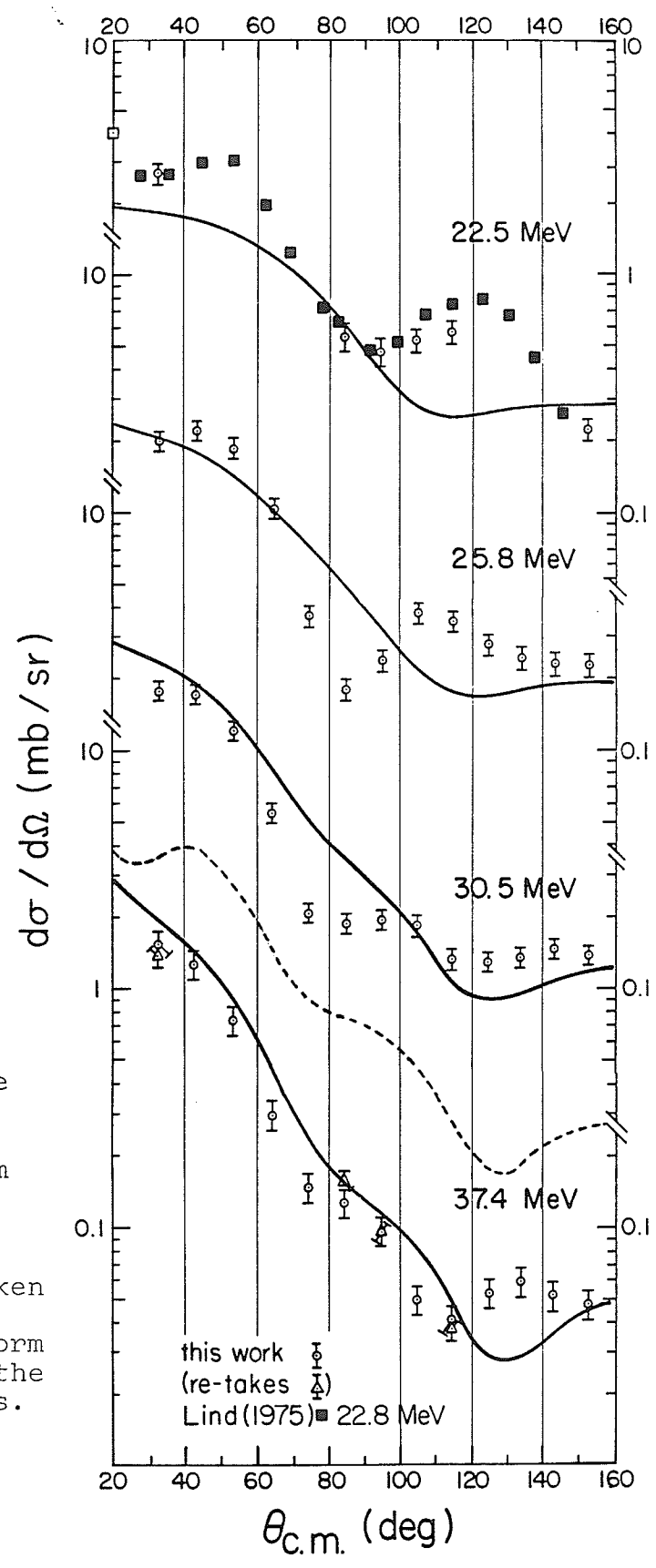


Fig. 1-15 Results (solid lines) of Lane model calculations using trial Lane potential inferred from the global 1p-shell potential of Watson et al. (1969) (see table 1-7). The broken curve results from assuming a surface form factor for  $V_1(r)$  in the 37.4 MeV calculations.

overall slope<sup>†</sup>.

Whereas it is possible with the current computer code to change the strength parameters  $V_1$  and  $W_1$  without affecting the proton potential,  $U_p$ , it is not possible to alter the geometry parameters of  $U_1$  without also changing the geometry of  $U_p$ . This restriction is not present in a more recent version of TWAVE (Byrd, 1978, 1979) which we hope to be obtaining soon. This expanded program accepts the input potentials in any of the forms  $(U_p, U_n)$ ,  $(U_p, U_1)$ ,  $(U_0, U_1)$ ,  $(U_<, U_>)$ , or  $(V_0, V_1, W_<, W_>)$ . The program converts from any of these representations into the  $(U_{pC}, U_{nA}, U_{pn})$  form in which the equations are actually solved. The conversion is a point-by-point transformation as the radial form of the potential is evaluated, thus including all the implications of different geometry parameters. By use of input in the form  $(U_p, U_1)$  for example, the isovector strength and geometry parameters can be adjusted at will to provide the best fit to  $(p, n)$  data without the slightest effect on  $U_p$ .

Two more features of the updated code which should be particularly useful are that it provides an automatic

---

† Trials with TWAVE confirmed that multiplying both  $V_1$  and  $W_1$  by a factor  $S$  (hence multiplying the geometric mean of  $V_1$  and  $W_1$  by  $S$  but leaving the ratio  $V_1/W_1$  unchanged) has the effect of shifting the entire  $(p, n)$  cross section curve upwards by a factor of  $S^2$ . Changing  $V_1/W_1$  while holding the geometric mean constant has the effect of "tilting" the curve. Larger  $V_1/W_1$  results in a steeper overall slope.

search for the best fit to the data and permits use of the Watson form of the spin orbit potential (equation 1-22) which may be more suitable for light nuclei.

In the Lane model analyses discussed above it was assumed that  $V_1(r)$  had a volume Woods-Saxon form. Actually, there are reasons to believe  $V_1(r)$  may be surface peaked. Since the isovector part of the Lane potential is essentially the difference between proton and neutron potentials, one might expect its radial form to reflect the distribution of the additional neutrons in a nucleus with neutron excess. If the extra neutrons form a neutron "skin" this would definitely imply surface peaking of  $V_1(r)$ . Such qualitative arguments have been supported by Hartree-Fock calculations (Dover and Van Giai, 1972).

In his Lane model analysis of  ${}^9\text{Be}(p,n_0){}^9\text{B}$  data, Byrd (1978) found that it was difficult to predict the correct location of the (p,n) cross section minima using a volume form factor for  $V_1(r)$ . Although a good description was eventually provided with a volume form factor (Byrd et al. 1979) by using 15 free parameters and imposing multi-channel and polarization constraints, the failure of our volume form factor to correctly predict the location of the (p,n) cross section minima suggests that a surface peaked  $V_1(r)$  should be tried.

The result of arbitrarily changing  $V_1(r)$  to a pure Woods-Saxon derivative surface form for the 37.4 MeV cal-

ulation is shown as a broken line in Fig. 1-15. It is realized of course that the proton potential is no longer correct, and no attempt has been made to correct the obvious scale factor error by adjusting the strengths  $V_1$  and  $W_1$ . The structure, however, is sufficiently enhanced, particularly in the region of the first minimum near  $30^\circ$ , to make some form of surface form factor for  $V_1(r)$  appear interesting for trial once a suitable computer program is available.

### 1.5.3 Applicability of the analysis

Fundamental to the applicability of the Lane model analysis is the question of the applicability of the optical model itself. Although the optical model is usually associated with heavier nuclei, previous work has shown that it can be applied successfully to light nuclei. The work of Watson et al. (1969) (from which our trial Lane potential was inferred) produced a good optical model description of (p,p) and (n,n) elastic scattering for a series of 1p-shell nuclei including  $^{13}\text{C}$ . Greaves et al. (1972) described both cross section and polarization data for (p,p) elastic scattering by  $^{13}\text{C}$  using a macroscopic optical model. Thus while the general applicability of the optical model to light nuclei may be questioned, there seems to be no reason why, in this case, it should not be successful.

Another fundamental requirement of our analysis is that the reaction be direct. If the measured neutron yields are contaminated by non-direct, compound nucleus processes,

then no direct reaction model can provide an adequate description. This certainly does not seem to be a general problem in our energy range.

Carlson et al. (1975) discuss the problem of compound nucleus contribution in some detail in the analysis of their 22.8 MeV (p,n) IAS data. They conclude that contributions from compound nucleus processes are insignificant. Similarly, other workers (Byrd, 1978; Hoffman & Coker, 1974) have concluded that compound nucleus formation should be no problem at several MeV above the threshold for the (p,n) reaction to the analog state.

In general, processes dominated by direct reaction mechanisms are identified by the absence of any resonance structure in the forward angle excitation function and by angular distributions with the distinct direct reaction diffraction signature.

Byrd (1978) found a smooth variation with energy in the forward angle  ${}^9\text{Be}(p,n_0){}^9\text{B}$  cross section to energies as low as 10 MeV. Some resonance structure was noted in the  ${}^{15}\text{N}(p,n_0){}^{15}\text{O}$  cross section excitation function, but even this was smoothing out by 12 MeV. The energies of our data are not closely enough spaced to give a meaningful excitation function but the measured forward angle cross sections do change smoothly with energy. Since our incident energies are considerably higher than those in the work of Byrd mentioned above, it seems likely that if our forward angle

cross sections for  $^{13}\text{C}(p,n_0)^{13}\text{N}$  were measured at more closely spaced energies, no resonances would be found.

Our angular distributions, particularly at higher energy, do show the forward angle peaking and back angle minima characteristic of a direct reaction.

In summary it does not seem that our observed neutron yields are significantly contaminated by compound nucleus decays. The final test, of course, is the extent to which a direct reaction model can give an adequate description of the data.

## 1.6 SUMMARY & CONCLUSIONS

Quasielastic (p,n) reactions are those leaving the residual nucleus in the isobaric analog state of the target. Such reactions may be viewed as elastic scattering with isospin flip.

Lane (1962) showed that a single optical potential,

$$U = U_0 + \frac{4(\vec{t} \cdot \vec{T})}{A} U_1$$

where  $\vec{t}$  is the isospin of the projectile and  $\vec{T}$  the isospin of the target, could provide a simultaneous description of (p,p) elastic, (p,n) quasielastic and (n,n) elastic scattering. As the entire interaction responsible for the (p,n) quasielastic process is  $U_{pn} = 2(2T)^{\frac{1}{2}}U_1/A$ , the (p,n) reaction provides a sensitive tool for investigating the details of the  $U_1$  part of such a potential.

We have measured differential cross sections for the  $^{13}\text{C}(p,n_0)^{13}\text{N}$  reaction at energies of 22.5, 25.8, 30.5 and 37.4 MeV for laboratory angles between  $30^\circ$  and  $150^\circ$ . The neutrons were detected by means of an organic liquid scintillator (NE213) and the isobaric analog state (ground state) neutron group identified by the use of time of flight techniques.

An energy dependent Lane potential taken from the analysis of Patterson et al. (1976) was used in an isospin conserving coupled channels calculation to predict the (p,n<sub>0</sub>) cross sections. The agreement with the data was not

particularly good, especially at backward angles. It is believed that this is because the potential of Patterson et al was obtained by fitting data from  $^{48}\text{Ca}$  to  $^{208}\text{Pb}$  and the potential apparently fails for lighter nuclei.

A second trial Lane potential was formulated from the global 1p-shell proton and neutron potentials of Watson et al. (1969). The results of Lane model calculations performed using this potential are in better agreement with the data than are the calculations performed using the potential of Patterson. They do, however, fail to fit the shape of the angular distributions, in particular the location of the diffraction minima. This indicates the need to alter the radial shape of the isospin dependent part of the potential. Some surface peaking of the real isospin dependent potential may be advantageous.

More work is required to determine the exact form of the potential. The present results, though, are encouraging and it should be possible to obtain a Lane model potential affording a good description of the  $^{13}\text{C}$  plus nucleon system.

CHAPTER 2  
A SCINTILLATING LIQUID ARGON TARGET

## 2.1 INTRODUCTION

The work described in this chapter arose out of the need for a good scintillating analyser for use in measuring the polarization of fast neutrons. Such a need arises, for example, in measuring the polarization of neutrons from the  $^{13}\text{C}(p, \vec{n})^{13}\text{N}$  reaction mentioned at the start of chapter one. Fig. 2-1 shows a practical method of making such a measurement. The unpolarized proton beam is incident on a target and partially polarized neutrons from the reaction are observed at an angle  $\theta$ . Two detectors, A and B, are located symmetrically to the right and left of a scatterer of known analysing power. The neutrons are allowed to fall on the scatterer and the relative number of counts in detectors A and B recorded.

If R is the number of counts recorded in the right detector and L the number of counts recorded in the left detector in the same time, then the right-left asymmetry defined by

$$\epsilon = \frac{R-L}{R+L} \quad 2-1$$

is given by the simple expression

$$\epsilon = P \cdot A(\phi) \quad 2-2$$

where P is the polarization of the incident beam and  $A(\phi)$  is the analysing power of the scatterer. In practice, the different count rates observed by detectors A and B may be due in part to small differences in the electronics or geometry of the two channels. The spin precession solenoid

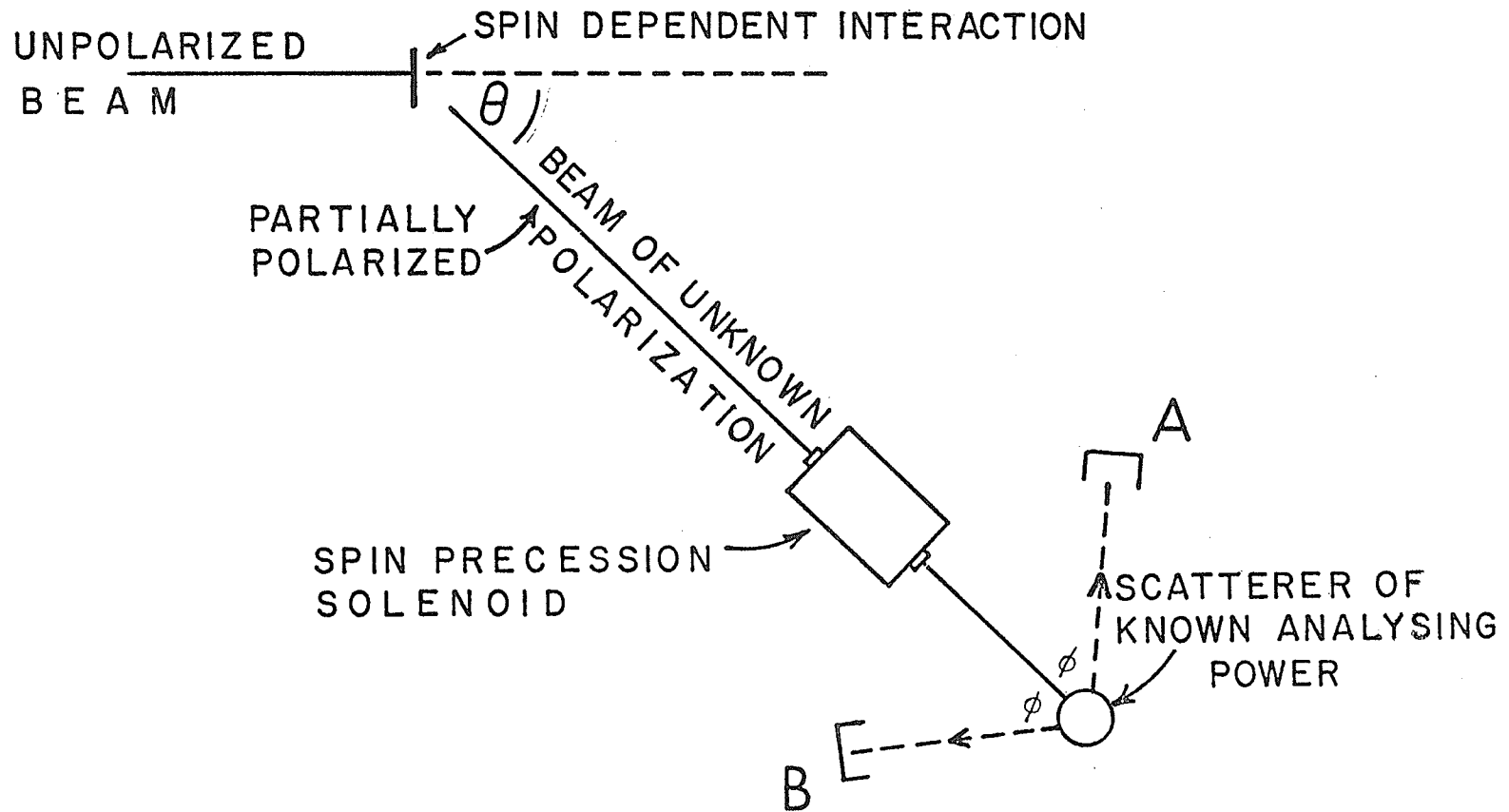


Fig. 2-1 Method of measuring neutron polarization. Neutrons are scattered from a target of known analysing power. The spin precession solenoid is used to cancel instrumental asymmetry.

is used to cancel the effects of such instrumental asymmetry. By using the spin precession solenoid to turn the incident neutron spin through  $180^\circ$ , the left-right roles of the two detectors are switched. That part of the asymmetry arising from true spin dependent scattering will hence reverse whereas any part due to instrumental asymmetry will not.

We can re-write 2-1 as

$$\epsilon = \frac{\frac{R}{L}-1}{\frac{R}{L}+1} = \frac{r-1}{r+1} \quad 2-3$$

If  $r_1 = R_a/L_b$  is the ratio when detector A is right and detector B is left, and  $r_2 = R_b/L_a$  is the ratio when detector B is right and detector A is left, then use of the geometric mean  $r = \sqrt{r_1 r_2}$  in 2-3 gives the true scattering asymmetry, corrected for instrumental effects.

When measuring polarization by this method, the only signals of interest in detectors A and B are those resulting from neutrons actually scattered from the analyser. In practice, the number of neutrons arriving at the side detectors directly from the neutron source may exceed, by orders of magnitude, the number actually scattered from the analyser into the side detectors. If the analyser scintillates, this provides a means of separating the pulses representing legitimate scatterings from the undesired background. Not only does the scintillation accurately fix the time of a scattering event, but the intensity of the scintillation

depends on the energy of the recoil nucleus and hence on the angle through which the neutron was scattered. By viewing the scintillations with a photomultiplier it is thus possible to electronically reject those detector pulses not appearing in the correct time interval following a scattering or not corresponding to a scattering through the known detector angle. This technique of using the recoiling particle to reduce background is called the "associated particle method" and is particularly important in fast neutron work where shielding is very expensive and not completely effective.

Most neutron polarimeters use liquid helium as the analyser. Helium scintillates and has a high analysing power that is accurately known and fairly constant over a wide range of angles and energies. Unfortunately liquid helium is very cold (4.2K) and boils off very easily (one Watt boils off 33 litres per day). By contrast, liquid argon is relatively warm (87.4K) and is much harder to boil off (one Watt boils off only 0.38 litres per day). Since argon is known to scintillate (Birks, 1967; Blyth and Phillips, 1975), it was decided to try liquid argon in an existing neutron polarimeter (Birchall et al, 1968, 1971). Even if argon does not prove suitable as an analyser, a good liquid argon target will be useful in its own right, making possible experiments on the scattering of neutrons from argon.

## 2.2 EXPERIMENTAL

### 2.2.1 The Polarimeter

A cross section of the polarimeter is shown in Fig. 2-2. The scintillating liquid is located in a 7 cm diameter copper scintillation volume and in a reservoir located above the scintillation volume. Total capacity is 1.2 litres. To minimize boil-off, the space surrounding the scintillation volume is maintained at a vacuum of approximately  $10^{-4}$  pascal. The scintillation volume is also surrounded by copper radiation shields maintained at liquid nitrogen temperature. To measure how much heat was being transferred into the scintillation volume and reservoir, the boil-off rate was measured. The heat leak was then calculated directly from the heat of vaporization. Initially we found that the heat leak with liquid helium in the inner volume was about 2.7 Watts. When filled with liquid nitrogen the heat leak was almost the same (2.5 W). This indicated that the leak was between the scintillation volume/reservoir area and a region essentially at room temperature. If heat was being transferred mainly from the heat shields or nitrogen reservoir then the heat leak would be expected to be almost zero when the inner volume was filled with liquid nitrogen. By wrapping the upper ends of the filling and boil-off tubes with copper shim stock so as to make thermal contact with the liquid nitrogen jacket, the temperature of the upper end of these tubes was lowered

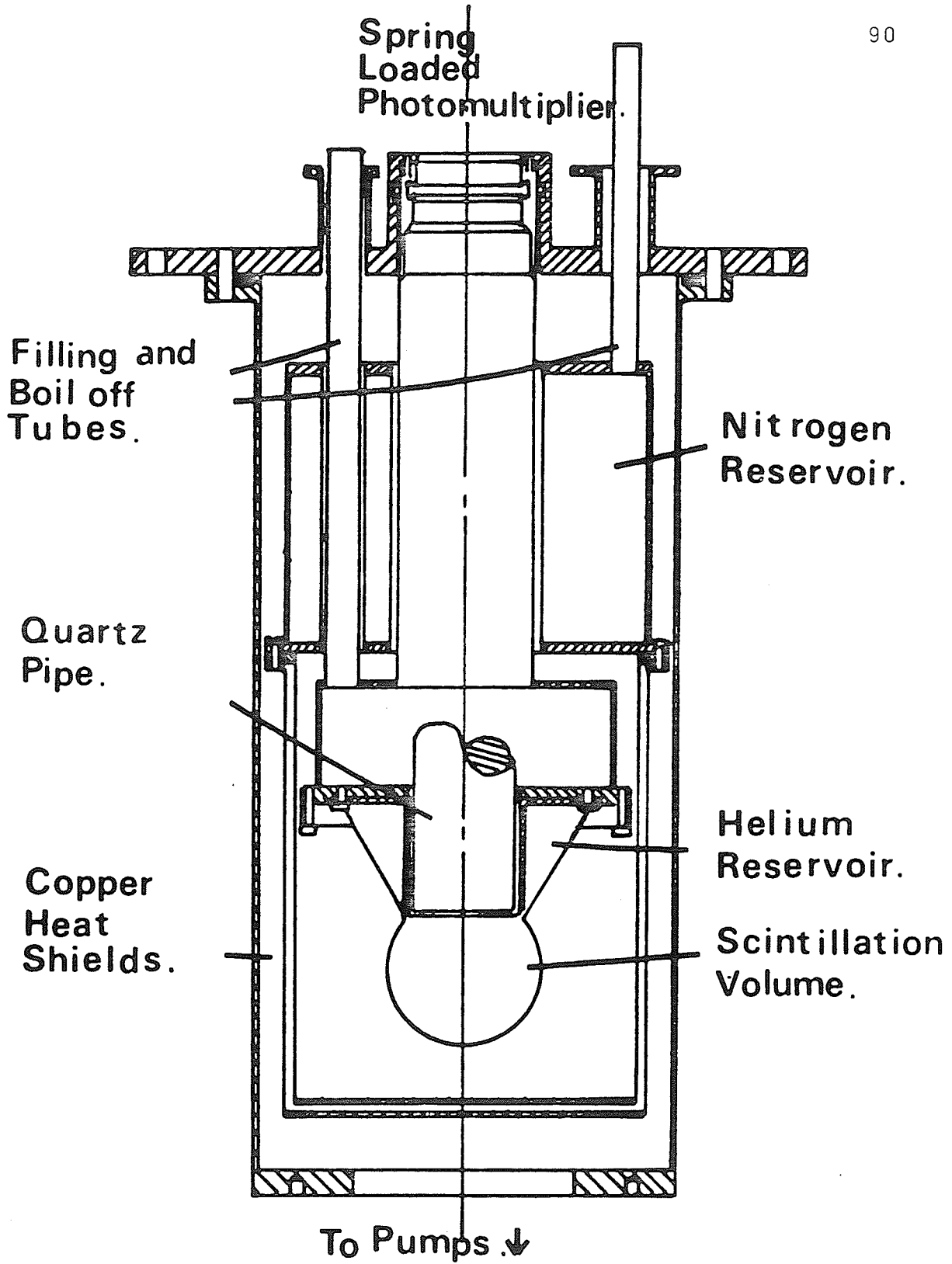


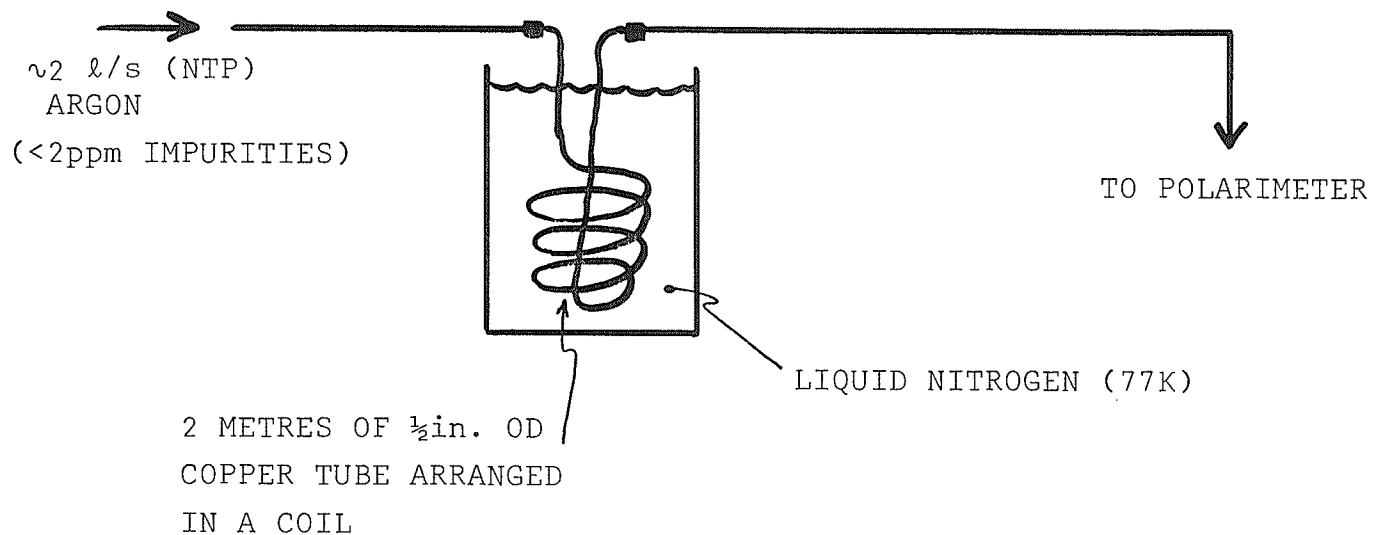
Fig. 2-2 Cross section of the polarimeter.

considerably. This reduced the heat leak (with liquid nitrogen in the inner volume) to 1.5 Watts. Raising the quartz light pipe out of contact with the liquid had little effect on the heat leak so it is believed that most heat still entered through the filling and boil-off tubes. Smaller diameter tubes and better thermal clamping of their upper ends would probably reduce the heat leak significantly.

Both liquid helium and liquid argon scintillate in the ultraviolet. For this reason the inside of the scintillation volume and the end of the light pipe are coated with the wavelength shifter pp' diphenylstilbene (DPS) which converts the light to the violet. Titanium dioxide is used as reflector paint and  $100\mu\text{g}/\text{cm}^2$  DPS is deposited on the inside of the ball and  $30\mu\text{g}/\text{cm}^2$  DPS on the end of the light pipe. The quartz light pipe provides direct optical coupling between the scintillation volume and an RCA8575 photomultiplier which is spring loaded and mounted vertically above the 38 cm long light pipe.

### 2.2.2 Making Liquid Argon

Argon is condensed by passing it through 2 metres of "one-half inch O.D." copper tubing arranged in a coil and immersed in liquid nitrogen (Fig. 2-3). A flow rate of two NTP gaseous litres per second (estimated from rate of pressure drop in the argon cylinder) is found to be adequate



ARGON: liquid 87.4K  
 freezes 83.8K

Fig. 2-3 Method of preparing liquid argon. The flow rate indicated is low enough to ensure that no uncondensed argon is fed through, but not so low that the condensing coil freezes up.

to prevent freeze-up<sup>†</sup> but not so high as to result in feed-through of uncondensed gas. The liquid argon flows directly into the scintillating volume of the polarimeter. A complete filling with liquid argon takes about 15 minutes using this method.

### 2.2.3 Testing with an $\alpha$ -source

A small monoenergetic alpha source is a very useful tool for testing the polarimeter. The alpha particles simulate the monoenergetic recoil nuclei which would result from neutrons scattered through a specific angle. A series of pulse height spectra taken with the alpha source at different locations in the volume will reveal both the energy resolution of the system and the extent to which pulse height depends on the location of the scintillation. Fig. 2-4 shows a pulse height spectrum of scintillations induced in liquid argon by 5.3 MeV alpha particles from a small  $^{210}\text{Po}$  source at the centre of the scintillation volume. The resolution is about 25% FWHM. During initial  $\alpha$ -source testing it was found that performance was not repeatable and appeared to be easily degraded by the presence of impurities. In particular the pulse height spectrum was often strongly dependent on the position of the  $\alpha$ -source within the volume

---

<sup>†</sup> At one atmosphere the boiling point of argon is 87.4K and the freezing point 83.8K. In liquid nitrogen at 77K the condensing coil can easily freeze up.

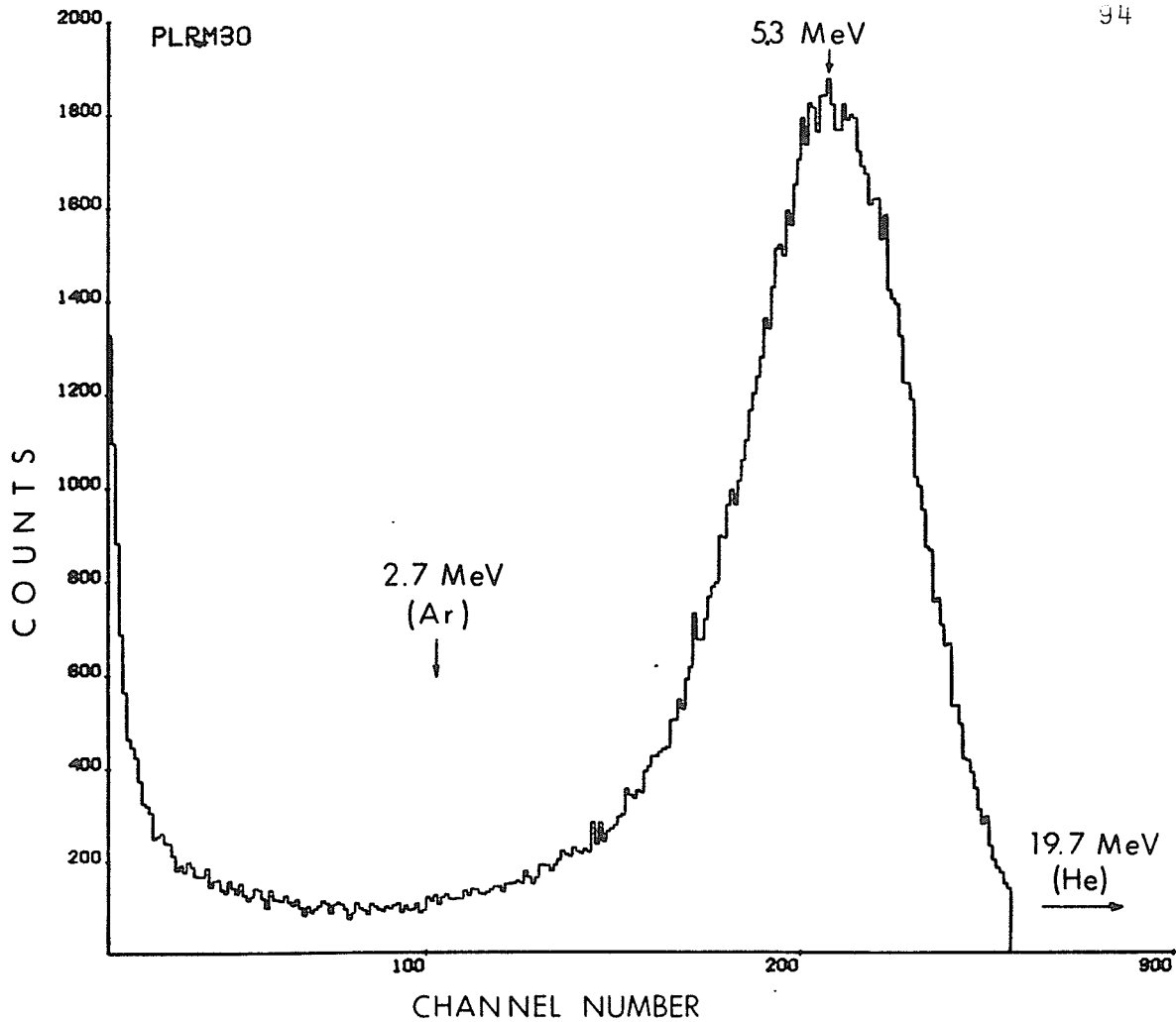


Fig. 2-4 Pulse height spectrum of scintillations induced in liquid argon by 5.3 MeV alpha particles from a  $^{210}\text{Po}$  alpha source. Also shown are the energy and corresponding peak position of the recoil nucleus for 36 MeV neutrons scattering through  $120^\circ$ . Helium peak is off scale to the right.

of liquid argon. This behaviour is shown in Fig. 2-5 and is indicative of strong self absorption of the primary ultraviolet scintillation light. The explanation of the spectrum is as follows: both argon and helium scintillate in the ultraviolet and the emitted radiation is shifted to the violet region by a wavelength shifter coated on the inside of the scintillation volume. When impurities are present in the liquid argon, heavy absorption of the primary ultraviolet occurs but not when the light is shifted into the visible (the argon appears clear to the eye). The range of alpha particles in liquid argon is so small (50 $\mu$ m) that the scintillations appear essentially on the surface of the 380 $\mu$ m diameter wire. Two main peaks are apparent in the pulse height spectra - one from scintillations on the bottom half of the wire and the other from scintillations on the top. The intensity of the upper peak (from scintillations on the side of the wire nearest the wavelength shifter) was found to vary exponentially with distance from the wall at a rate indicating a self absorption mean free path of <1 cm. By contrast Kayne et al (1963) found that samples of liquid argon from a commercial spigot had self absorption mean free paths ranging from 2.1 cm to 7.5 cm, and measures made on a local spectrophotometer<sup>†</sup> indicated >10 cm.

---

<sup>†</sup> Made using argon gas at 150 atmospheres and extrapolating to the density of liquid argon (840 atmospheres equivalent).

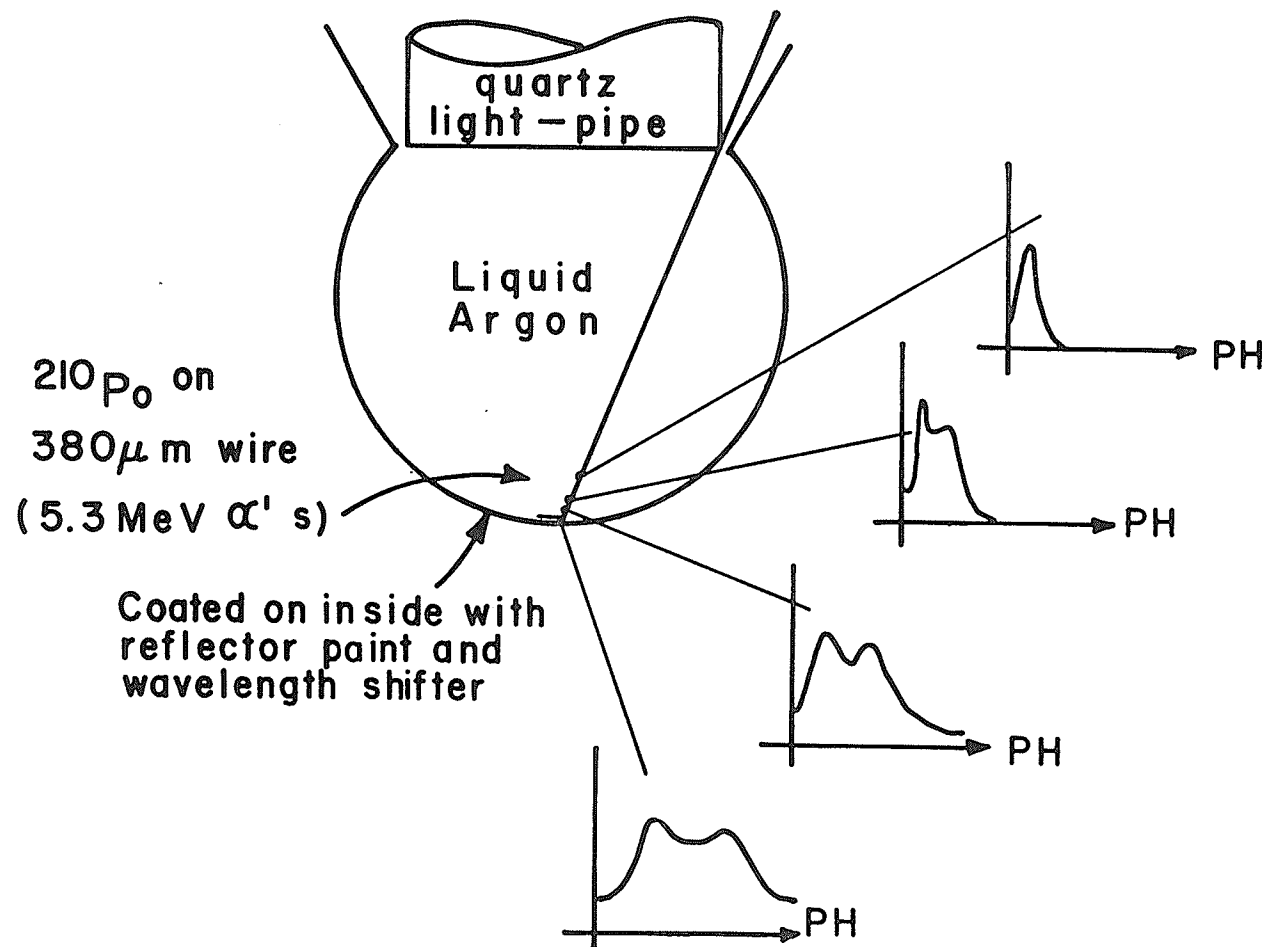


Fig. 2-5 Pulse height spectra for different alpha source positions shown under conditions of strong self-absorption.

As the strong self absorption seemed to indicate the presence of fog, it was decided to try evacuating the whole system (pipes, condensing coil, scintillating volume) before filling. This method has been very successful. Holding the system at a roughing pressure of less than 2 Pascal for 3 hours and then venting to argon before filling, results in one strong peak of virtually the same intensity for all positions of the source.

#### 2.2.4 Testing with Fast Neutrons

Once good repeatable results were obtained with the  $\alpha$ -source, tests were made with fast neutrons. Because of the relatively large mass of an argon nucleus, the recoil energy and hence the scintillation pulse height is reduced as compared with that from a helium scintillator. In Fig. 2-4 the recoil energies are indicated for 36 MeV neutrons scattering through  $120^\circ$  (Lab) from argon and helium for comparison with the 5.3 MeV alpha peak. It is seen that although the pulses from argon will be much lower than from helium they are still useable.

Tests were made with fast neutrons as shown in Fig. 2-6. Neutrons were produced by means of the reaction  ${}^7\text{Li}(p,n){}^7\text{Be}$ . The proton sweep magnet removed protons from the forward flux and the neutrons were used at  $0^\circ$ . With a  $50 \text{ mg/cm}^2$   ${}^7\text{Li}$  target, a  $1\mu\text{A}$  proton beam resulted in approximately  $2 \times 10^5$  neutrons per second following collimation (Watson et al, 1976). This flux was confined to

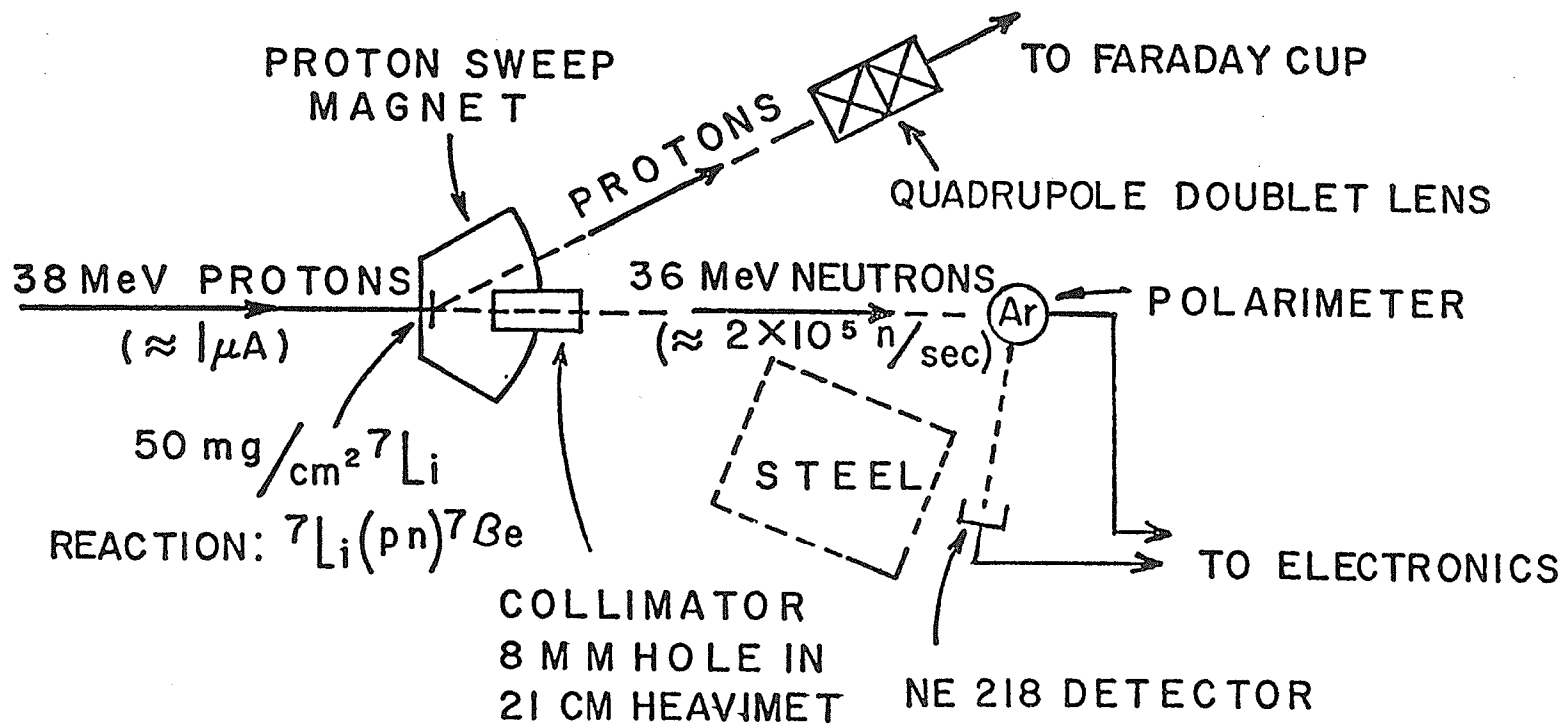


Fig. 2-6 Testing with fast neutrons.

roughly a 2 cm diameter spot at the argon scintillator. The neutron energy may be changed by altering the energy of the proton beam which is variable from 20 to 50 MeV. The experiments described here used a neutron energy of 36 MeV.

The polarimeter was placed a distance of 1.3 metres from the lithium target, with the neutron beam centered on the scintillating volume. Initial alignment was accomplished using a small laser. The detector, a 2 inch NE218 liquid scintillator coupled to an RCA 8575 photomultiplier, was mounted on a moveable stand and could be placed at various distances and angles relative to the polarimeter. Steel bricks were placed so as to shield the detector from the direct flux of neutrons from the production target. It was found that 60 cm of steel reduced the neutron flux at the detector location by a factor of several hundred.

Even with the shielding mentioned above, there was still a high background count rate at the detector. For a total count rate from the detector of 1000 Hz only about one count every two seconds was found to come from neutrons scattered from the argon into the detector. The background is composed mainly of gamma rays, neutrons scattered from the metal parts of the polarimeter, and neutrons not removed by the steel shielding. Neutron gamma pulse shape discrimination (n- $\gamma$  PSD), time of flight techniques and pulse height information can be used to separate the desired events from background. This is accomplished by the

electronics shown in block diagram form in Fig. 2-7.

Standard RCA 8575 2" photomultiplier tubes are fitted to the polarimeter and NE218 liquid scintillator. The phototube used with the NE218 is operated in the conventional grounded anode configuration for best pulse fidelity, whereas the one on the polarimeter is operated in the grounded cathode configuration to avoid possible difficulties connected with the polarimeter imposing a ground at the front face of the tube.

Constant fraction discriminators are used to derive fast timing signals from the photomultiplier anodes.

Pulse height information is derived by taking linear signals from an earlier stage (dynode 9) of the photomultiplier. Pulses from the polarimeter are amplified by the usual charge sensitive preamplifier and shaping spectroscopy amplifier. Linear pulses from the phototube used with the NE218 are amplified by a charge sensitive preamplifier and double delay line amplifier. The resulting bipolar pulse is used in the n- $\gamma$  PSD circuit. The portion of the circuit devoted to n- $\gamma$  PSD is enclosed in a dotted line on Fig. 2-7. The operation of the PSD is the same as described in section 1.3.1 with the exception that here we have used single parameter PSD rather than the two dimensional PSD-PH technique described in 1.3.1. Adequate separation of neutrons and gammas was obtained, however, as is illustrated in the spectrum of Fig. 2-8.

With a 1 $\mu$ A proton beam on a 50 mg/cm<sup>2</sup> <sup>7</sup>Li target



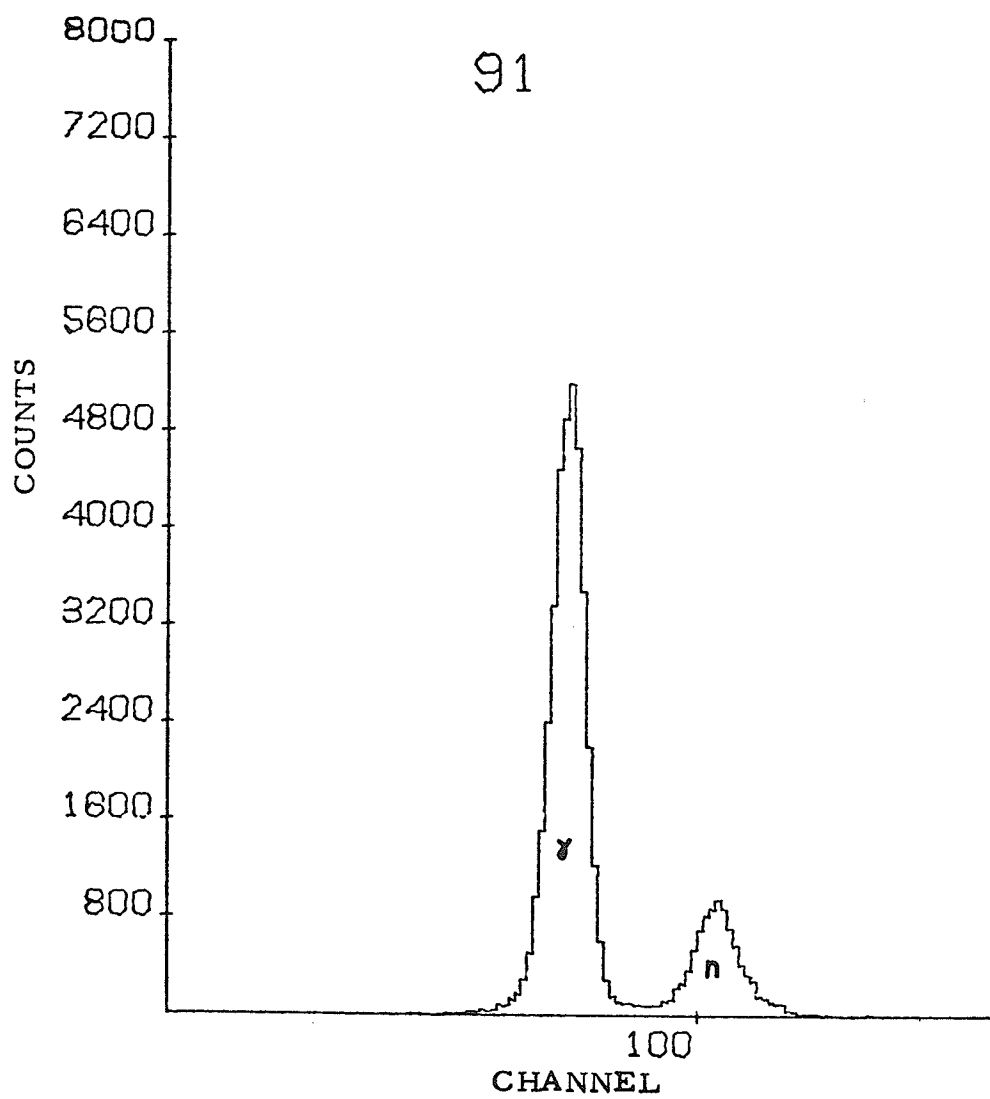


Fig. 2-8 n- $\gamma$  PSD spectrum.

there were about 100 counts per second in the neutron peak and 900 counts per second in the gamma peak.

#### 2.2.4.1 Delayed coincidence

Of the 100 counts attributable to neutrons, only on the order of one count every two seconds came from a neutron scattered into the detector from the argon. These "true" events may be identified by their time relation to the scintillations in the argon. If, for example, a scattered neutron is known to take 6 ns to travel from argon to detector, then any detector pulse corresponding to a legitimate event will be preceded by an argon scintillation occurring 6 ns earlier. The time to amplitude converter labelled "TAC 2" in Fig. 2-7 is used to establish this time relation. It is started with the timing signal from the detector, and stopped with the timing signal from the polarimeter. Delay is introduced into the stop channel as required to place the desired coincidence within range of the TAC. Fig. 2-9 is a pulse height spectrum taken from TAC 2, accepting only those pulses identified as "neutron" by the n- $\gamma$  PSD.

Zero on the time axis corresponds to those scintillations occurring simultaneously in the polarimeter and detector. To the left are those occurring later in the detector and to the right, earlier. We see a large "true coincidence" peak superimposed on a background of "random coincidences." The total number of real counts is obtained

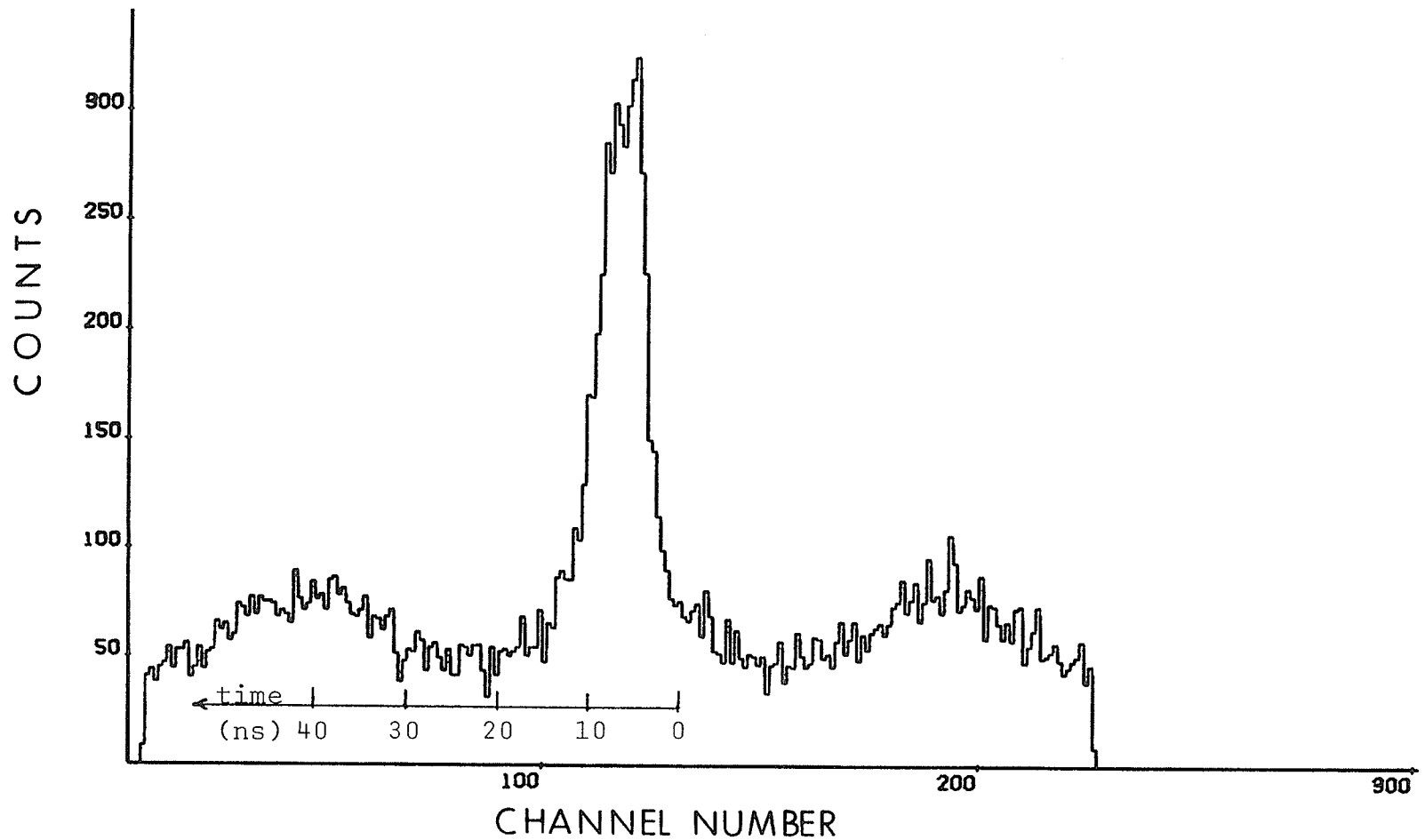


Fig. 2-9 Spectrum of time differences between neutron events in the polarimeter and side detector. Large "true coincidence" peak corresponds to neutrons reaching the detector by means of scattering from the liquid argon.

by fitting the background and subtracting it, leaving only the true coincidences. A statistical precision of 3% following background subtraction was obtained after 2 hours of running.

Notice that the background is periodic with a period of 35 ns. This is because the beam from the cyclotron arrives in bursts at the rate of one every 35 ns. The rate of random coincidences thus increases every 35 ns.

The rate of true coincidences varies directly as the beam current but the rate of random coincidences varies as the square of the beam current. The maximum beam current which can be tolerated and hence the running time required is dictated by the rate of random coincidences. It is clearly an advantage to reduce the randoms as much as possible electronically, which will result in minimum running time for a given statistical accuracy.

The rate,  $N_R$ , of random coincidences appearing in a time window  $\tau$  of the TAC 2 spectrum is given by  $N_R = \tau N_{Pol} N_{Det}$  where  $N_{Pol}$  is the effective count rate of the polarimeter and  $N_{Det}$  is the effective counting rate of the detector. The effect of shielding and n- $\gamma$  PSD in reducing  $N_{Det}$  has been seen.  $N_{Pol}$  can be reduced by means of pulse height discrimination and time of flight information.

#### 2.2.4.2 Time of flight

TAC 1 in Fig. 6 is used to measure the timing of polarimeter scintillations relative to the machine R.F.

It is started by the fast timing pulse and stopped by the R.F. Since the time of arrival of neutrons at the polarimeter always bears a fixed time relation to the machine R.F., placing a window on the appropriate peak in the TAC 1 spectrum (using SCA 1) permits the use of the polarimeter pulses which occur at the time of arrival of neutrons alone. This technique discriminates against gammas from the production target and to some extent against induced radioactivity in the copper of the polarimeter. The peaks in the polarimeter - R.F. TOF spectrum are fairly broad, but use of a TOF window can still reduce the effective polarimeter count rate several times.

#### 2.2.4.3 Pulse Height

Because the scintillation pulse height depends on the energy of the recoil nucleus and hence on the angle of scattering of the neutron, it is possible to reduce background by selecting only those pulse heights corresponding to neutron scattering into the known solid angle of the detector. Actually, it is here that one of the most severe difficulties arises in using argon instead of helium. The recoil energies of argon are significantly lower (e.g. 2.7 MeV argon compared to 19.6 MeV helium at  $120^\circ$  and 36 MeV incident neutron energy). Since to first order the energy resolution varies as  $1/\sqrt{E}$ , the energy resolution obtainable with neutrons on argon is also notably worse than with helium. The combined effect is to place the scintillation pulse

height for neutrons scattering through, say,  $100^\circ$ , in a low part of the spectrum and overlapping a region of very high count rate due to neutron induced radioactivity in the polarimeter. This does not destroy completely the use of pulse height information but its effect is not as dramatic. Work is continuing on methods of getting the maximum use from polarimeter pulse height information.

#### 2.2.5 Isoangular Volume

If the pulse height information is to be of maximum usefulness, it is important that a recoil nucleus of given energy produce the same pulse height due to ionization of other atoms regardless of where in the scintillation volume it is located. As mentioned in 2.2.3, minimum position dependence requires maximum purity of the scintillating liquid. It also requires the correct shape for the scintillation volume.

If the reflector paint on the inner wall of the scintillation volume were 100% reflecting and if self absorption were zero, the shape would not matter as all the light would reach the light pipe eventually regardless of the position of the scintillation. In practice, however, this is not true and pulse height is least dependent on position when the scintillating volume's shape is such that the circular end of the light pipe subtends the same solid angle at every point on the reflector.

The solid angle subtended at a point by a circular

disc is not easily calculated. To calculate the solid angle exactly one must evaluate

$$\Omega = \int_{r=0}^R \int_{\phi=0}^{2\pi} (\cos \theta / d^2) r \, dr \, d\phi \quad 2-4$$

where the notation is that of Fig. 2-10. Unfortunately no closed form solutions of 2-4 are known.

If the distance from the point to the disc is very large compared to the diameter of the disc, then the obliquely viewed circular disc can be approximated by a normally viewed ellipse. The solid angle is then calculated as the area of the ellipse divided by the square of the distance. The solid angle given by this "elliptical approximation" is (Birchall, 1969)

$$\Omega \approx \frac{\pi R^2 h (\rho^2 + h^2)^{\frac{1}{2}}}{(\rho^2 + h^2 - R\rho)^4} \quad 2-5$$

where the notation is still that of Fig. 2-10.

In cases where the elliptical approximation is not valid, 2-4 must be solved exactly. Gardner and Carnesale (1969) have solved 2-4 numerically and represented the result in terms of the product of an analytical expression and a slowly varying correction factor. Their representation is based on the fact that a good approximation to the solid angle subtended by a disc is the solid angle subtended by a square of equal area.

By solving 2-4 exactly using the prescription of Gardner & Carnesale, we have calculated the radius ( $\rho$ ) as a function of height ( $h$ ) such that a disc of unit radius

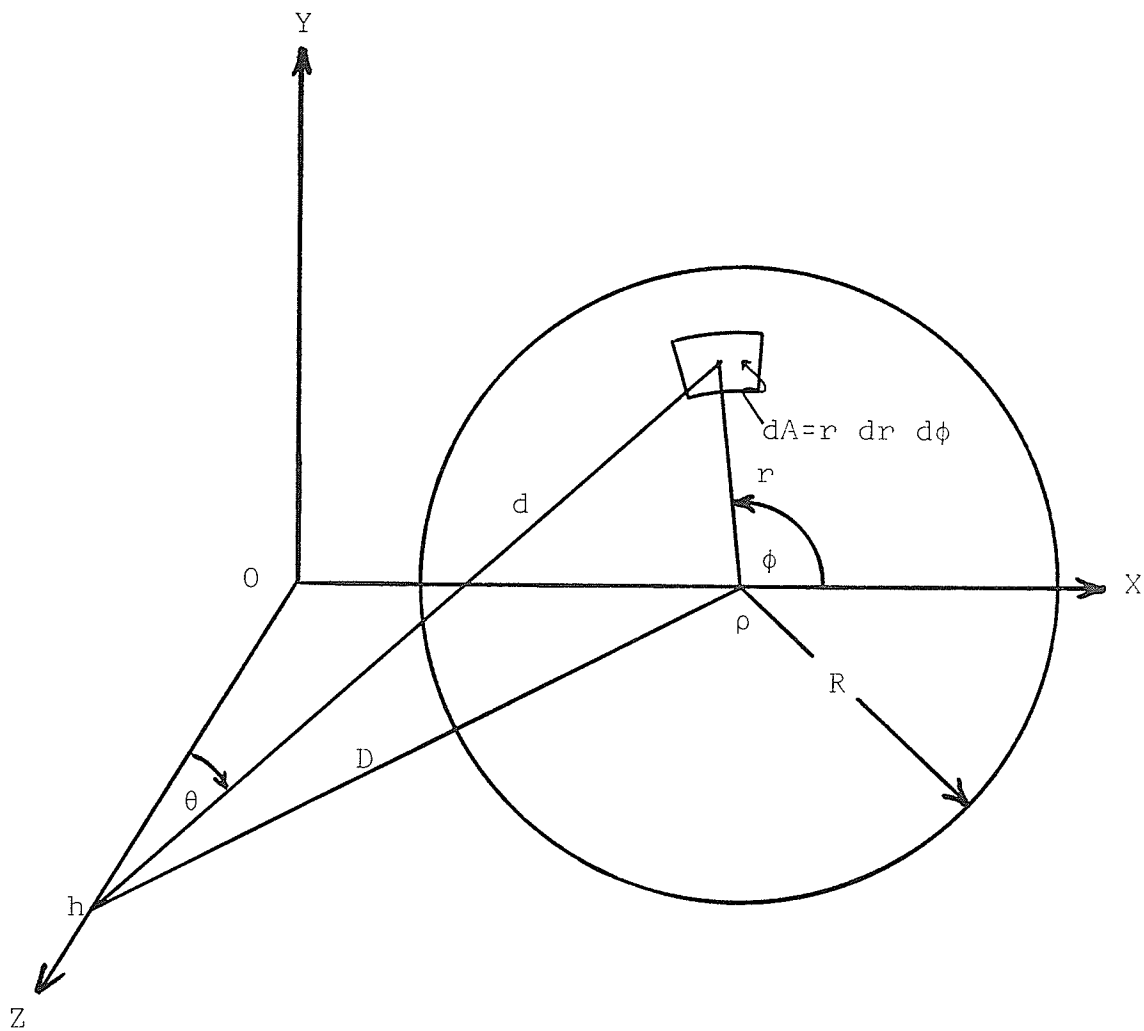


Fig. 2-10 Coordinate system and notation. Disc is in xy-plane.

subtends a constant solid angle of 0.322 sr.

Fig. 2-11 shows both the solid angle ( $\Omega$ ) and radius ( $\rho$ ) as a function of height for three different shapes. The solid curve is the isoangular shape. For this shape the radius at any given height is always just that required to yield a solid angle of 0.322 sr. Also shown is a spherical shape (dashed line) and a shape (dotted line) that gives a constant solid angle of 0.322 sr using the elliptical approximation (eqn. 2-5). Note that although the shape obtained using 2-5 does produce less variation in solid angle than does the sphere, it is still a considerable departure from the true isoangular shape.

In a fine piece of work, machinists at the Department of Physics shop have manufactured a true isoangular volume out of brass. It is intended to compare the performance obtained using the isoangular volume to that obtained with a spherical volume at a later date.

### 2.3 Conclusion

Using the methods described, liquid argon can be prepared fairly simply and used as a scintillating target for fast neutrons. The scintillations induced in liquid argon by fast neutrons are of lower intensity than those induced in liquid helium but are adequate to permit use of an "associated particle" system for reducing background. With a moderate amount of shielding a clean scattering experiment can be performed.

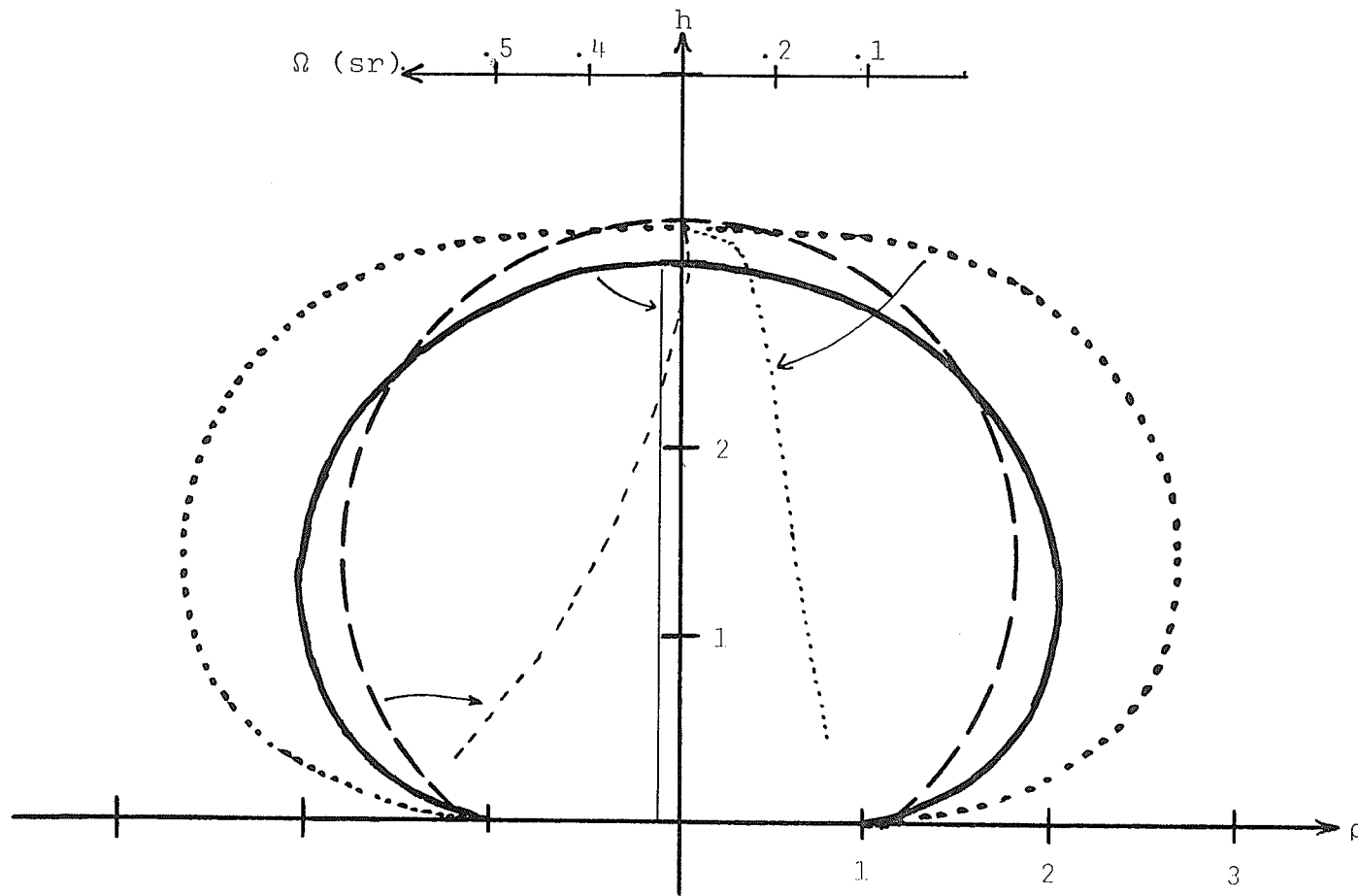


Fig. 2-11 Isoangular shape. Diagram shows radius ( $\rho$ ) and solid angle ( $\Omega$ ) as a function of height ( $h$ ) for three shapes - isoangular (solid lines), spherical (dashed lines), and "elliptical approximation" to isoangular (dotted lines).

#### 2.4 Future work

The isoangular volume will be tested and attempts made to reduce background even further by making best use of pulse height and time of flight information.

The analysing power of the argon should be measured and compared to liquid helium. If argon proves suitable as an analyser it would be cheaper and more convenient than liquid helium.

Regardless of the success of argon as an analyser, it should be possible, using this scintillating liquid argon target, to make useful measures of cross section and angular distributions for the scattering of neutrons from argon.

CHAPTER 3

PROTON INDUCED K-SHELL IONIZATION STUDIES

### 3.1 INTRODUCTION

Our interest in K-shell ionization arose because of the utility of characteristic x-rays in trace element analysis. If a target is bombarded by protons energetic enough to cause inner shell ionization, then the x-rays emitted when the inner shell vacancies are filled can be detected by a suitable detector and the resulting x-ray spectrum used to identify the elements in the target.

Most proton induced x-ray work has been done at very low (Van de Graff) energies, often under 4 MeV. In fact, until recently, it was widely believed that background problems would be so severe above a few MeV that there would be no use studying x-ray fluorescence at higher proton energies. This belief may have been based on the common practice of observing L x-rays, because we have had no difficulty obtaining clean K x-ray spectra using protons in the 20-50 MeV range incident on a variety of targets.

While it is not necessary to know ionization cross sections for trace element analysis (the whole system can be calibrated by recording spectra from calibration targets of accurately known composition), the quality of our K x-ray spectra and the virtual absence of data in our energy range made the measurement of such cross sections very attractive. The only other data within the energy range of the Manitoba Cyclotron are those of Bissinger et al. (1970, 1972) bombarding Ca and Ti at energies up to 25 MeV, Ni at

energies up to 28 MeV and Ag at energies up to 30 MeV.

We have measured K-shell ionization cross sections for the targets Cu, Rb, Ag, Eu and Au, each at nominal proton energies of 24, 32 and 44 MeV.

### 3.2 THEORIES OF K-SHELL IONIZATION

Experimental data are usually interpreted within the framework of the Plane Wave Born Approximation (PWBA), Semi-Classical Approximation (SCA) (Hansteen, 1975) or Binary Encounter Approximation (BEA) (Garcia, 1973). These theories are compared in the review of Madison and Merzbacher (1975). The essential features of each are as follows.

#### 3.2.1 PWBA (Plane Wave Born Approximation)

The plane wave Born approximation takes plane wave states for the incident and scattered proton. The PWBA transition amplitude is

$$T = \frac{1}{(2\pi)^3} \int e^{-i\vec{k}_f \cdot \vec{R}} \langle n' | \frac{-e^2}{|\vec{R}-\vec{r}|} | n \rangle e^{i\vec{k}_i \cdot \vec{R}} d^3R \quad 3-1$$

$$= \frac{-e^2}{2\pi^2 q^2} \langle n' | e^{i\vec{q} \cdot \vec{r}} | n \rangle \quad 3-2$$

where  $n$  and  $n'$  are the initial and final atomic states,  $\vec{r}$  is the position vector of the active atomic electron,  $\vec{R}$  is the position vector pointing from the atom to the projectile,  $\vec{k}_i$  and  $\vec{k}_f$  are the initial and final momenta of the relative motion, and  $\vec{q} = \vec{k}_i - \vec{k}_f$  is the momentum transfer to the atom.

Khandelwal et al. (1969) calculated ionization cross sections in the PWBA using nonrelativistic hydrogenic wavefunctions for a single electron making a transition from K-shell to continuum. These calculations have been published as tables.

The PWBA predicts a scaling law for the integrated cross section. It is

$$\frac{\sigma_k U_k^2}{\theta_k} = f\left(\frac{m}{M} \frac{E_p}{U_k} \frac{1}{\theta_k}\right) \quad 3-3$$

where  $\sigma_k$  is the cross section for K-shell ionization,  $U_k$  is the actual K-ionization energy,  $m/M$  is the ratio of electron mass to proton mass,  $E_p$  is the proton energy, and  $\theta_k$  is the K-shell screening parameter equal to the ratio of actual to hydrogenic ionization energies. Specifically,

$$\theta_k = U_k / Z_k^2 R_\infty \quad 3-4$$

where  $Z_k$  is the effective charge "seen" by K electrons, usually taken to be  $Z_k = Z - 0.3$ , and  $R_\infty$  is the Rydberg constant (13.6 eV).

The PWBA can be improved by use of distorted (Coulomb) waves for the projectile and ejected electron. This is most important at low energies where atomic binding cannot be ignored. In such cases the use of plane waves is not a good approximation and tends to overestimate the cross section.

Another improvement sometimes attempted is the use of better atomic wavefunctions such as hydrogenic Dirac or Hartree-Fock Slater.

### 3.2.2 SCA (Semi-Classical Approximation)

In the Semi-Classical Approximation the proton is taken to move along a purely classical trajectory (usually a straight line). The atom is treated as a quantum

mechanical system subject to a time dependent Coulomb perturbation

$$V(\vec{r},t) = \frac{-e^2}{|\vec{R}(t)-\vec{r}|} \quad 3-5$$

where  $\vec{R}$  and  $\vec{r}$  have the same meanings as in 3-1.

The SCA predicts the same scaling law (3-3) as does the PWBA. In fact, for cases in which interaction with the target nucleus may be neglected, both PWBA and SCA predict the same total ionization cross section<sup>†</sup>. When the interaction of the proton with the target nucleus is not negligible, but when its energy loss is still small, the predictions of the SCA can be improved by using hyperbolic Kepler orbits (rather than a straight line) for the proton trajectory.

The SCA is most applicable in cases where the atomic electron is tightly bound (heavy target) and where the proton is moving swiftly.

### 3.2.3 BEA (Binary Encounter Approximation)

The BEA is a purely classical theory motivated by the remarkable fact that the differential cross section for nonrelativistic scattering by a  $1/r$  potential (Rutherford scattering) is exactly the same whether calculated classically, in the exact quantum mechanical treatment, or in the

---

<sup>†</sup> In practice, discrepancies between PWBA and standard SCA results may arise from different treatment of screening or the use of unrealistic continuum wavefunctions in the SCA (Aashamar and Kocbach, 1977).

Born approximation. The BEA treats the collision of the proton and the target as a purely classical (Rutherford) encounter between the proton and a free electron of velocity  $\vec{v}$ . An average is then taken over the distribution of electronic velocities in the initial atomic state.

Original BEA calculations (Garcia, 1973; McGuire & Richard, 1973) indicated a scaling law,

$$U_k^2 \sigma_k = f \left( \frac{m E_p}{M U_k^2} \right), \quad 3-6$$

which differs slightly from the scaling law (3-3) predicted by the PWBA and SCA. Langenberg and Van Eck (1978) have shown that this discrepancy can be attributed to the use of an unrealistic velocity distribution for the target electron. Using a realistic velocity distribution, they arrive at the scaling law

$$\frac{U_k^2 \sigma_k}{\theta_k} = f \left( \frac{m E_p}{M U_k^2} \frac{1}{\theta_k} \right)$$

- exactly the same as predicted by the PWBA and SCA.

It is very difficult to improve the BEA without losing simplicity. It rapidly becomes more complicated than the quantum mechanics it is supposed to replace.

As the BEA is essentially an impulse approximation it agrees fairly well with the PWBA at higher energies. It is, however, very difficult to set precise limits on the applicability of the BEA.

Application of the scaling law (3-3) causes data

obtained using a wide variety of proton energies and targets to coalesce into a single "universal curve". The data obtained in this experiment are presented in such a way in Fig. 3-4. The broad maximum corresponds to an incident proton velocity equal to the orbital velocity of the bound electron. This maximum in ionization cross section is often referred to as the "velocity matching peak".

### 3.3 THE EXPERIMENT

K-shell ionization cross sections were measured over a wide range of  $\left(\frac{m}{M} \frac{E_D}{U_k} \frac{1}{\theta_k}\right)$  using the experimental setup shown schematically in Fig. 3-1. Protons of nominal energy 24, 32, or 44 MeV are incident on one of five targets and the induced x-rays are detected by a planar Ge(Li) detector.<sup>†</sup> The targets were selected so that, on the universal curve, the 44 MeV data obtained using any target just overlap the 24 MeV data obtained using the target of next lowest z. In this way a range of  $\left(\frac{m}{M} \frac{E_D}{U_k} \frac{1}{\theta_k}\right)$  from 0.15 to 3.5 was covered in five overlapping ranges.

The targets were thin (of the order 200 $\mu$ g/cm<sup>2</sup>) and were prepared by vacuum evaporation on 51 $\mu$ m Kapton film. Gold, silver and copper were evaporated in elemental form, while europium and rubidium were evaporated as chlorides and protected with  $\approx$ 30 $\mu$ g/cm<sup>2</sup> copper.

The target was mounted at 80<sup>o</sup> to the incident beam and the Ge(Li) detector viewed the target from an angle of 120<sup>o</sup> to the forward beam direction. These somewhat unusual angles permitted the simultaneous use of a beam monitor already available in the chamber.

The proton beam was stopped in a suppressed Faraday cup and integrated to give total charge.

---

<sup>†</sup> ORTEC 4.75 mm active depth by 10 mm active diameter.

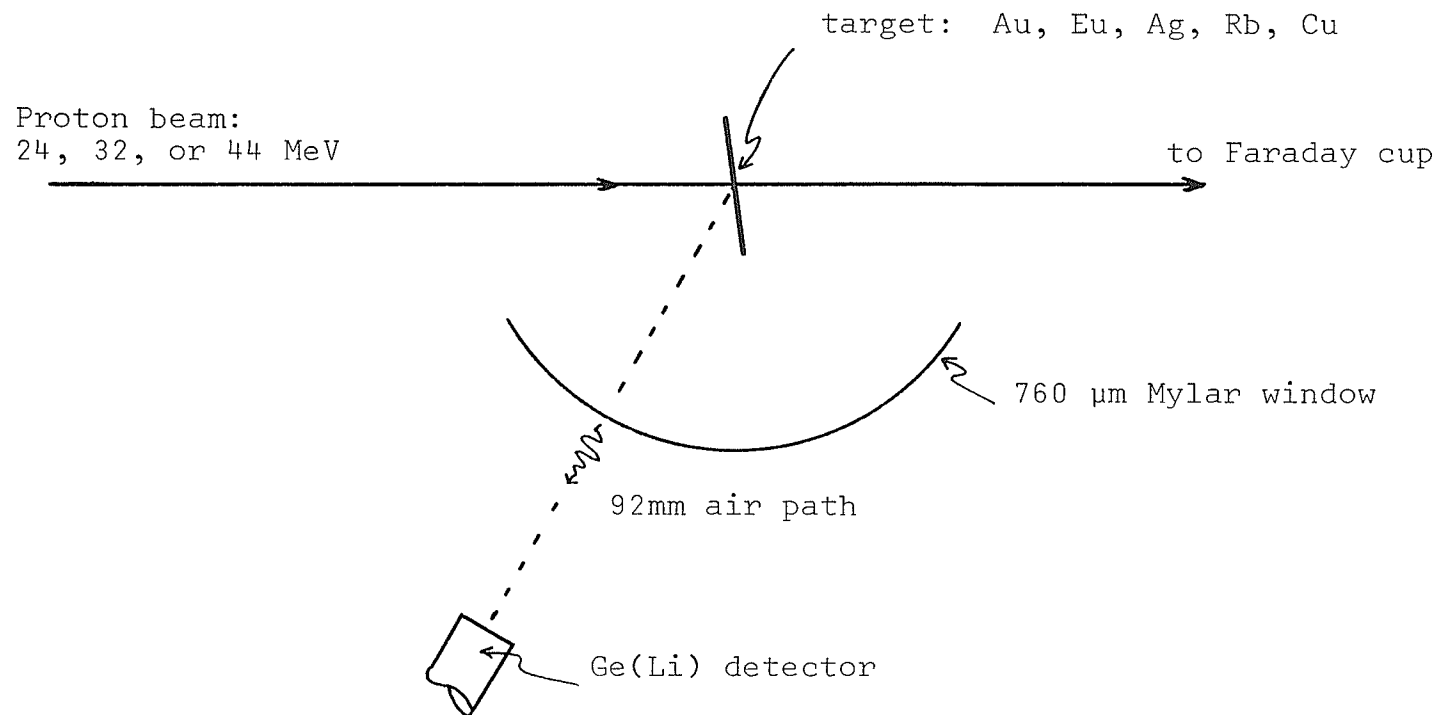


Fig. 3-1 Schematic diagram of the experiment to measure K-shell ionization cross sections.

Signals from the Ge(Li) detector's built in preamplifier were prepared for pulse height analysis by a standard spectroscopy amplifier and fed to an analog to digital converter. 1024 channel spectra were accumulated using a PDP-15 computer. Background subtraction and peak integration yielded the total counts in the K x-ray peaks for each element.

### 3.3.1 Correction for Satellite Peaks

Sample spectra are shown in Fig. 3-2. The gold spectrum shows a small satellite peak at the high energy side of the gold  $K_{\alpha_1}$  peak. This peak results from mercury  $K_{\alpha_1}$  x-rays emitted following de-excitation by internal conversion of mercury atoms from (p,xn) reactions on gold (Randell et al. 1976). The satellite peak is mentioned here because its presence indicates that other mercury x-ray peaks are present. The mercury  $K_{\alpha_2}$  is unresolved, lying under the gold  $K_{\alpha_1}$ , and the mercury  $K_{\beta_1}$  is also unresolved, lying under the gold  $K_{\beta_2}$ . The number of counts in the unresolved mercury peaks was estimated from the number of counts in the satellite peak by using known relative x-ray intensities. The observed K x-ray yield was then corrected for the contribution of the unresolved peaks.

### 3.3.2 Ge(Li) Detector Efficiency

The efficiency of the Ge(Li) detector was measured using an open  $^{241}\text{Am}$  source calibrated against an IAEA standard source. The number of photons per disintegration

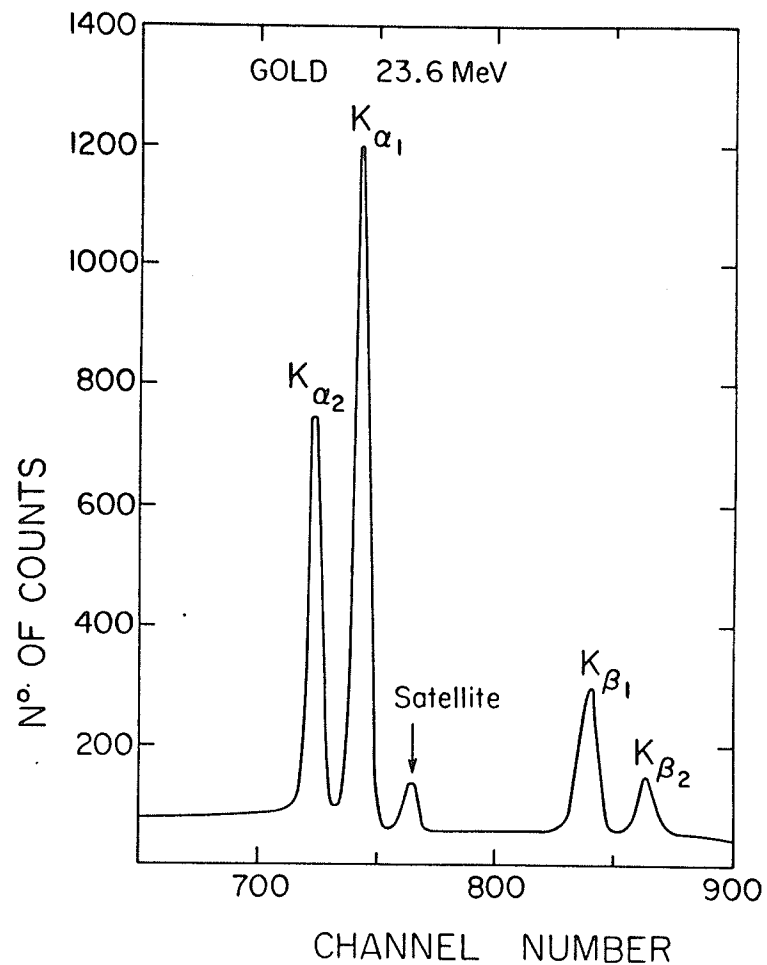
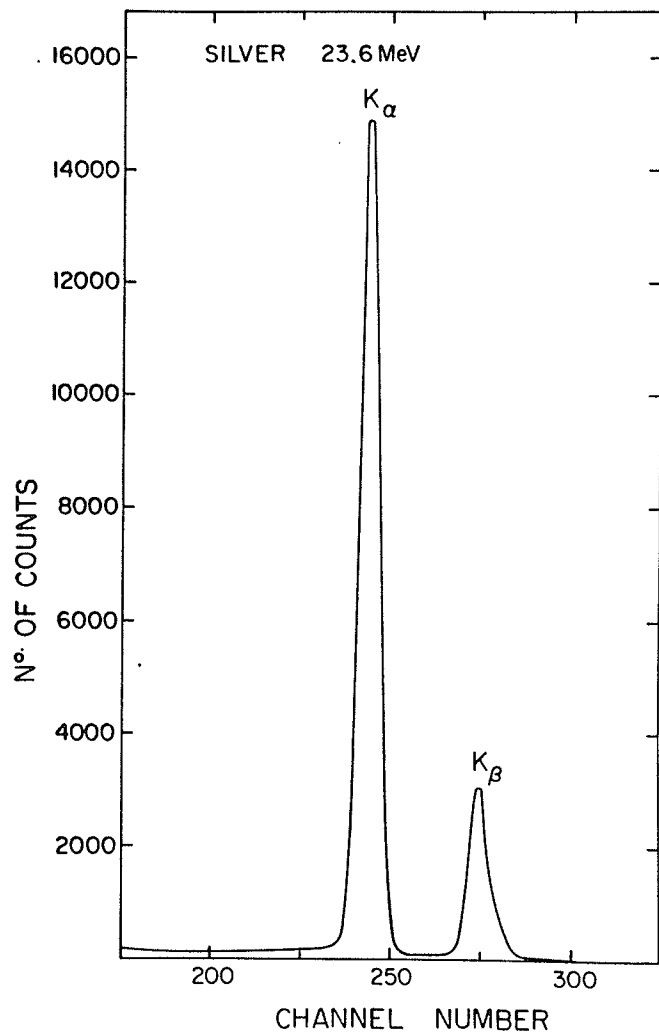


Fig. 3-2 Sample x-ray spectra. a) K x-rays from silver at 23.6 MeV incident proton energy, b) K x-rays from gold at 23.6 MeV incident proton energy showing satellite peak.

as tabulated by Campbell and McNelles (1974) was used. The effective crystal location was found by measuring the variation in count rate with distance and determining the crystal location required to give  $1/r^2$  dependence. By using this distance, the known effective area of the detector, and the number of photons per disintegration, it was possible to calculate the number of photons of each energy incident on the detector crystal. Comparing this number to the number of counts actually recorded gives the detection efficiency. The measured efficiency is shown as a function of energy in Fig. 3-3. The solid portion of the curve is fitted to the 5 points taken with  $^{241}\text{Am}$ . The dotted extension is based on the model of Hansen et al. (1973). At the low energy end the efficiency is dominated by absorption in the germanium deadlayer and the beryllium window of the detector. The efficiency decline at high energy is the result of high energy photons not depositing all their energy in the crystal.

K x-ray energies for the targets used in this experiment are also indicated in Fig. 3-3.

### 3.3.3 Absorption Corrections

As shown in Fig. 3-1, x-rays from the target must pass through a 0.76 mm Mylar window and 92 mm of air on their way to the detector. The absorption in Mylar and air was calculated using the total photon cross sections of Veigele (1973). The results, for the x-ray energies of

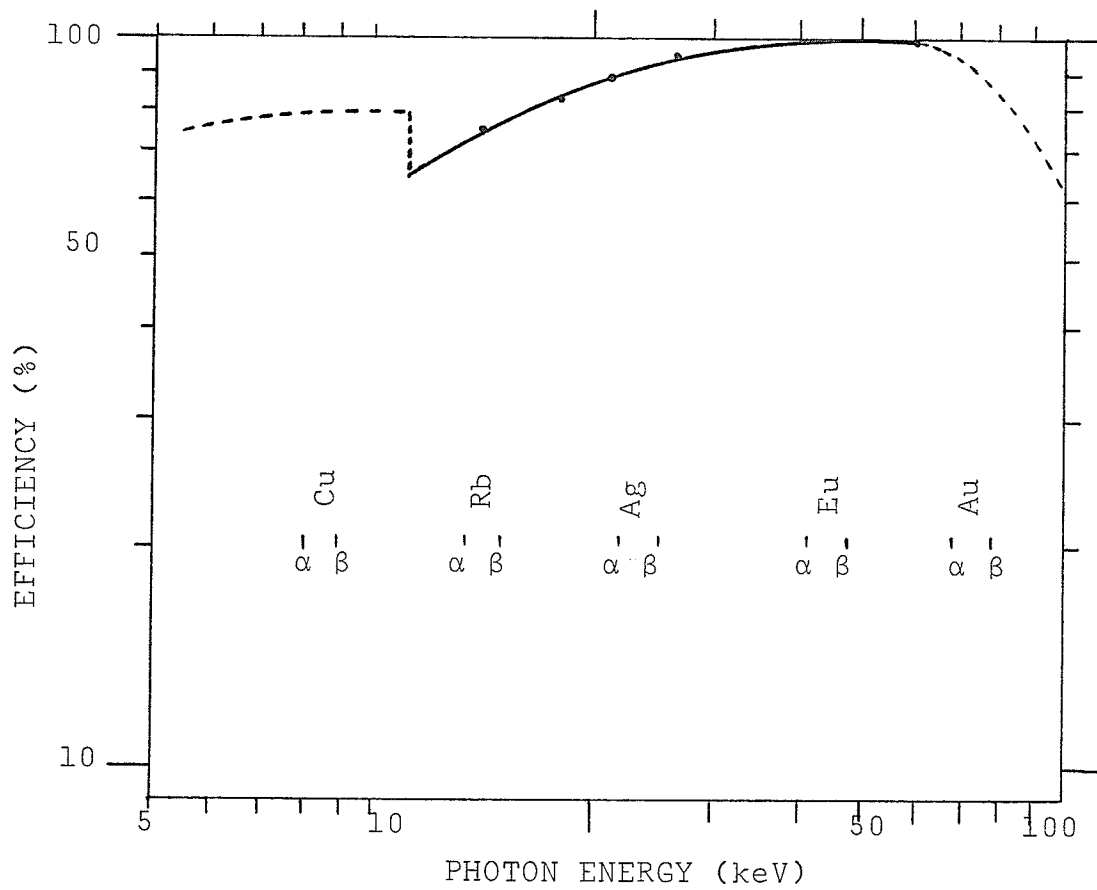


Fig. 3-3 Efficiency of the Ge(Li) detector. The solid portion is a fit to the 5 data points taken with  $^{241}\text{Am}$ . The dotted extension is based on the model of Hansen et al. (1973). K x-ray energies for this experiment are also indicated.

interest are listed in table 3-1. The effective detection efficiency for a given energy x-ray is found by multiplying the Ge(Li) efficiency for that energy (Fig. 3-3) by the transmission through the Mylar and air (Table 3-1).

#### 3.3.4 Results

The quantity actually measured in this experiment is the cross section for K x-ray production. To calculate the cross section for K-shell ionization it is necessary to know what fraction of K-shell vacancies are filled by means of a radiative transition. This information was obtained from the fluorescence yields of Bambynek (1973), and the measured x-ray production cross sections were readily converted to ionization cross sections.

The measured K-shell ionization cross sections are shown in Fig. 3-4. Overall normalization has been chosen to fit the well documented rising portion of the curve. Because the relative detection efficiencies and fluorescence yields are known, the single normalization is sufficient for all data. Relative uncertainties are approximately 8% for Rb, Ag, Eu, and 13% for Cu and Au due to the larger uncertainty in detection efficiency for K x-rays from these elements.

Fig. 3-4 shows clearly the variation in the predictions of the PWBA for screening parameters of 0.95 and 0.65. The experimental results are consistent with these predictions.

Element	Line	Approximate energy (KeV)	Transmission through 0.1059 g/cm <sup>2</sup> Mylar and 0.0111 gm/cm <sup>2</sup> Air
Copper	K <sub>α</sub>	8.0	0.435
	K <sub>β</sub>	8.9	0.545
Rubidium	K <sub>α</sub>	13.4	0.828
	K <sub>β</sub>	15.0	0.869
Silver	K <sub>α</sub>	22	0.943
	K <sub>β</sub>	25	0.955
Europium	K <sub>α</sub>	41	0.975
	K <sub>β</sub>	47	0.975
Gold	K <sub>α</sub>	68	0.980
	K <sub>β</sub>	78	0.980

Table 3-1 Transmission through Mylar and air. The thicknesses correspond to 760μm thick Mylar and 92 mm of air at 20°C and 760 mm Hg pressure.

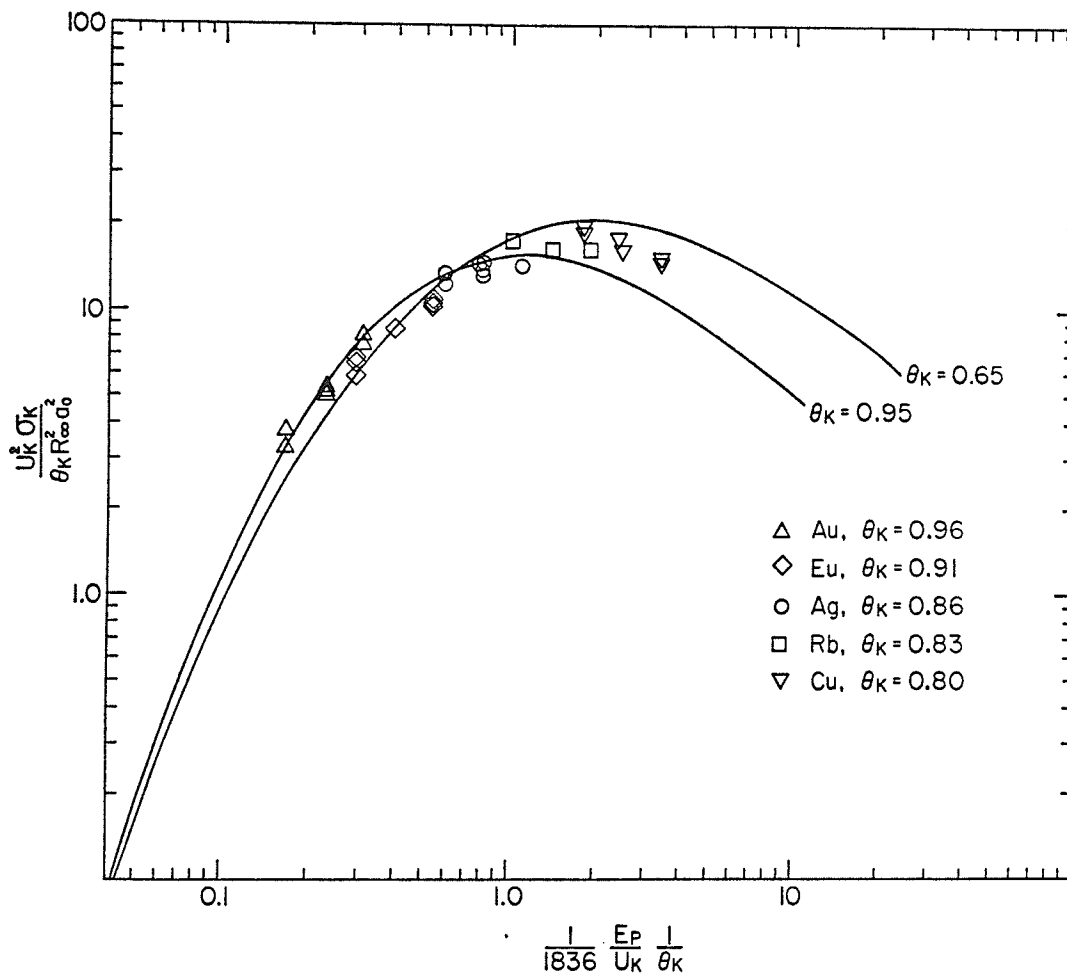


Fig. 3-4 K-shell ionization cross sections measured in this experiment plotted on the "universal curve". The axes are dimensionless.  $U_k$  is the actual K-ionization energy,  $\theta_k$  the K-shell screening parameter equal to the ratio of actual to hydrogenic ionization energies,  $R_\infty$  the Rydberg constant,  $a_0$  the Bohr radius ( $R_\infty^2 a_0^2 = 5179 \text{ KeV}^2$  barn),  $E_p$  the proton energy, and 1836 the ratio of proton mass to electron mass. Solid lines are PWBA results (Khandelwal, 1969).

### 3.4 RELATED WORK

This section reports two separate pieces of work related to the K-shell ionization experiment described in the preceding sections. The first (Kamal et al., 1980) is a study of  $K_{\beta}/K_{\alpha}$  x-ray intensity ratios. It is the result of an analysis, by Ziba Kamal, of the raw data taken in the K-shell ionization cross section experiment. The second is a brief discussion of transition radiation and its possible contribution to x-ray background from proton induced x-ray emission experiments (Ramsay and McKee, 1978).

#### 3.4.1 $K_{\beta}/K_{\alpha}$ x-ray intensity ratios

The obvious reason for calculating the  $K_{\beta}/K_{\alpha}$  ratios is to extract the maximum possible information from the experiment. More fundamentally though, there is some question of whether the  $K_{\beta}/K_{\alpha}$  ratio depends on the energy of the inducing proton. This might happen in the following way:  $K_{\alpha}$  x-rays are emitted when K-shell vacancies are filled by radiative transitions from the L-shell.  $K_{\beta}$  x-rays result when K vacancies are filled from the M or N shells. There is evidence (Der et al., 1971) for the production of multiple L-shell vacancies simultaneous with K vacancy production. Since  $K_{\alpha}$  transitions are fed from the L-shell, multiple L-shell vacancies reduce the probability of a  $K_{\alpha}$  transition. A variation in the extent of multiple ionization as the energy of the proton beam is changed would

cause the  $K_\beta/K_\alpha$  ratio to depend on the energy of the inducing proton.

To measure the  $K_\beta/K_\alpha$  ratios,  $K_\alpha$  and  $K_\beta$  counts were extracted separately from the raw spectra. The  $K_\alpha$  and  $K_\beta$  peaks overlap slightly in the spectra from copper and were unfolded using a Gaussian peak fitting routine. The observed  $K_\alpha$  and  $K_\beta$  counts were then corrected for the effects of different detector efficiency and absorption. The final  $K_\beta/K_\alpha$  ratios are displayed in Table 3-2, the error in each measurement being clearly indicated. To the accuracy of the experiment there would appear to be no dependence of the  $K_\beta/K_\alpha$  intensity ratio upon the energy of the inducing proton. This conclusion is further supported by Fig. 3-5 which includes the data of some earlier work at much lower energies. Again, within the errors quoted, the results are indistinguishable. Fig. 3-5 also shows the theoretical predictions of Scofield (1969, 1974). The data are consistent with the theoretical predictions (upper curve) which incorporate exchange corrections to the K x-ray transition rates in the calculations.

#### 3.4.2 Transition Radiation

Transition radiation is the name given to the radiation emitted when a charged particle crosses the boundary between two media with different dielectric constants. The situation for a charge moving from a vacuum ( $\mu = 1$ ,  $\epsilon = 1$ ) to a dielectric ( $\mu = 1$ ,  $\epsilon = \epsilon_1 + i\epsilon_2$ ) is shown

Element	$K_{\beta}/K_{\alpha}$ Ratios		
	$E_p = 23.6$ MeV	32.1 MeV	43.6 MeV
$^{29}\text{Cu}$	$0.1396 \pm 0.0084$	$0.1398 \pm 0.0084$	$0.1395 \pm 0.0084$
$^{37}\text{Rb}$	$0.1629 \pm 0.0098$	$0.166 \pm 0.010$	$0.1670 \pm 0.010$
$^{47}\text{Ag}$	$0.207 \pm 0.012$	$0.210 \pm 0.013$	$0.2127 \pm 0.013$
$^{63}\text{Eu}$	$0.247 \pm 0.016$	$0.243 \pm 0.016$	$0.2446 \pm 0.016$
$^{79}\text{Au}$	$0.252 \pm 0.025$	$0.2758 \pm 0.028$	$0.29 \pm 0.03$

Table 3-2 Measured  $K_{\beta}/K_{\alpha}$  Ratios.

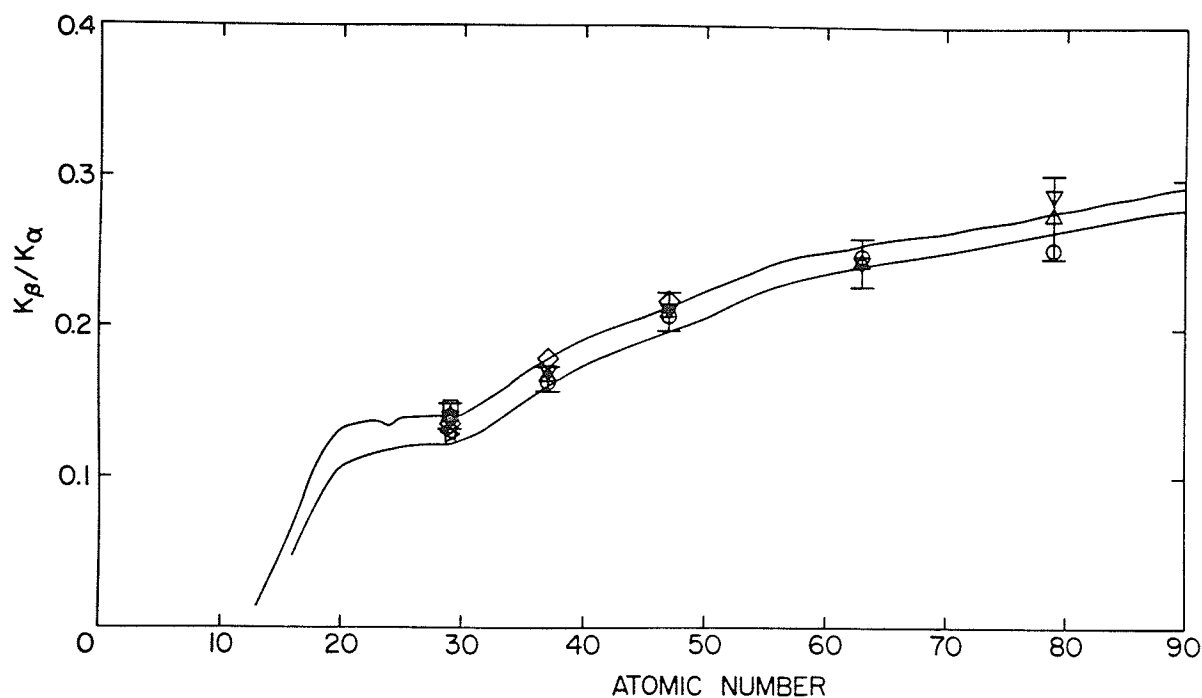


Fig. 3-5 Comparison between experimental values of  $K_{\beta}/K_{\alpha}$  for various elements from the present study, ratios from excitation by lower energy protons, and the theoretical predictions of Scofield (1969) (lower curve) and (1974) (upper curve) (incorporating exchange corrections).

- Legend:
- present work at  $E_p = 23.6$  MeV
  - △ present work at  $E_p = 32.1$  MeV
  - ▽ present work at  $E_p = 43.6$  MeV
  - Lear (1973)
  - ◇ Close (1973)
  - ◁ Bodart (1975)
  - ▷ Richard (1970)
- } <7 Mev

For copper the various data points are so nearly identical as to be almost indistinguishable.

schematically in Fig. 3-6. As indicated, the transition radiation is plane polarized. This feature is characteristic and provides a means of identifying transition radiation.

Transition radiation was first observed from anodes of x-ray tubes but not understood. The theory of transition radiation was first treated by Ginzburg and Frank (1946) and then developed by other authors (Beck, 1948; Korkhmazyan, 1957; Ter-Mikaelyan, 1959; Garibyan, 1958, 1960; Pafomov, 1960).

We became interested in transition radiation because of possible x-ray background in proton induced x-ray emission work. The predictions of transition radiation theory have been confirmed in the optical region by Goldsmith and Jelley (1959) using 1-5 MeV protons incident on aluminum, silver and gold, and more recently by Gibb et al. (1977) for 29 MeV protons incident on gold. Gibb points out that confirmation of the theory in the optical region should permit an estimate to be made of that portion of the transition radiation spectrum extending into the x-ray region.

#### 3.4.2.1 Theory

The case illustrated in Fig. 3-7, of a particle moving from a vacuum to a dielectric, is treated in detail by Garibyan (1958). The method is to write the field of the moving charged particle (in both vacuum and dielectric) in terms of Fourier components. A radiation field is then added and its Fourier components determined to satisfy

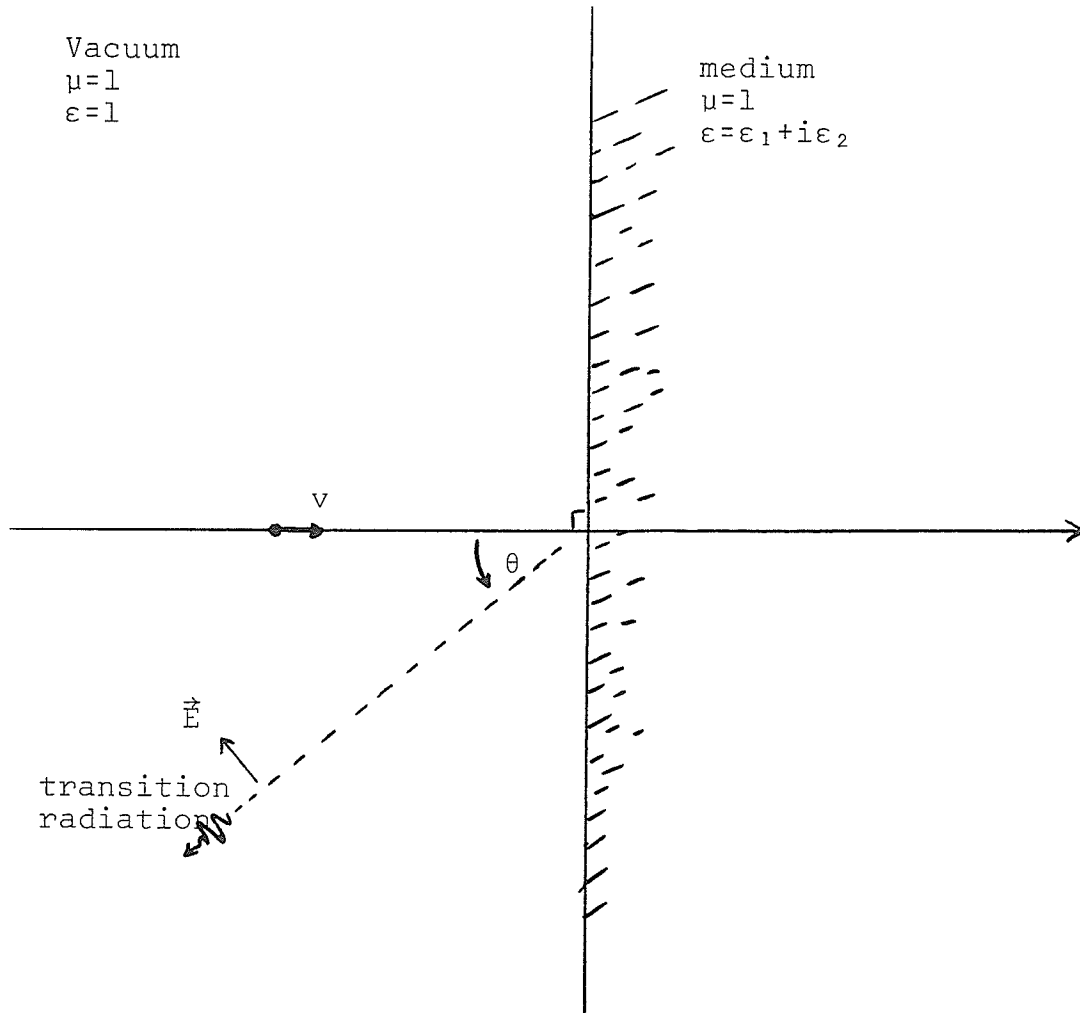


Fig. 3-6 Transition radiation. A pulse of radiation is emitted when a charged particle crosses the boundary between two media with different dielectric constants.

boundary conditions at the interface (i.e. so that tangential components of  $\vec{E}$  and  $\vec{H}$  and the normal components of  $\vec{B}$  and  $\vec{D}$  are continuous across the boundary). The actual radiation field is then found from the Fourier integrals and the transition radiation follows from the Poynting vector,  $\vec{P} = \vec{E} \times \vec{H}$ . Integrating over the time of flight of the particle, the energy radiated per unit circular frequency per unit solid angle in a direction  $\theta$  to the path of the particle is found to be

$$\frac{dW}{d\omega d\Omega} = \frac{ce^2 \sin^2 \theta \cos^2 \theta}{4\pi\epsilon_0 \pi^2 v^2} \frac{\beta^4}{(1 - \beta^2 \cos^2 \theta)^2} \times \left| \frac{(\epsilon-1)(1-\beta^2+\beta\sqrt{\epsilon-\sin^2\theta})}{(\epsilon\cos\theta+\sqrt{\epsilon-\sin^2\theta})(1+\beta\sqrt{\epsilon-\sin^2\theta})} \right|^2 \quad 3-7$$

where  $e$  is the charge of the particle,  $c$  is the speed of light and  $\beta = v/c$ . In deriving this expression it is assumed only that  $\theta$  is not very small and that the distance of the observer from the interface is large compared to a wavelength.

Expression 3-7 may be interpreted physically by rewriting it in the form

$$\frac{dW}{d\omega d\Omega} = \frac{e^2 v^2}{16\epsilon_0 \pi^3 c^3} \sin^2 \theta \left| \frac{1}{1+\beta\cos\theta} + \frac{r}{1-\beta\cos\theta} - f \frac{1}{\sqrt{\epsilon}} \frac{1}{1+\beta\sqrt{\epsilon-\sin^2\theta}} \right|^2 \quad 3-8$$

where  $r$  and  $f$  are Fresnel's reflection and refraction coefficients:

$$r = \frac{\epsilon\cos\theta - \sqrt{\epsilon - \sin^2\theta}}{\epsilon\cos\theta + \sqrt{\epsilon - \sin^2\theta}} \quad (E_{\text{reflected}} = rE_{\text{incident}})$$

$$f = \frac{2\sqrt{\epsilon} \cos\theta}{\epsilon \cos\theta + \sqrt{\epsilon - \sin^2\theta}} \quad (E_{\text{refracted}} = fE_{\text{incident}})$$

for further simplification consider the non-relativistic limit ( $\beta \rightarrow 0$ ). This gives

$$\frac{dW}{d\omega d\Omega} = \frac{e^2 v^2}{16\epsilon_0 \pi^3 c^3} \sin^2\theta \left| 1 + r - f \frac{1}{\sqrt{\epsilon}} \right|^2 \quad 3-9$$

The first term in the absolute value bars gives the radiation from a particle of charge  $e$  and velocity  $v$ , stopping at the boundary. The next term gives the radiation of the image charge stopping at the boundary, and the last term gives the radiation seen in the vacuum from a particle starting at the boundary and continuing in the medium. For a perfect conductor  $r=1$  making the image identical to the incident charge, and  $f=0$  meaning the charge disappears once into the conductor. For a vacuum,  $r=0$  and  $f/\sqrt{\epsilon} = 1$ , resulting in no transition radiation, as expected since there is no transition.

For a perfect conductor, the non-relativistic expression (3-9) becomes

$$\frac{dW}{d\omega d\Omega} = \frac{e^2 v^2 \sin^2\theta}{4\epsilon_0 \pi^3 c^3} \quad 3-10$$

It is this expression (3-10) which was confirmed in the optical region by the experiments of Goldsmith and Jelley (1959) and Gibb et al. (1977).

Since metals are not conductors for all frequencies but become transparent somewhere in the ultraviolet, expression (3-10) (for a perfect conductor) clearly cannot be used

in the x-ray region. It is necessary to use the complete expression (3-7) with realistic values of  $\epsilon = \epsilon(\omega)$ . Fig.3-7 shows examples of transition radiation spectra for copper and silver predicted by using 3-7 with values of  $\epsilon(\omega) = \epsilon_1(\omega) + i\epsilon_2(\omega)$  taken from the literature (Ehrenreich and Philip, 1962). The intensity is seen to drop sharply in the ultraviolet.

To estimate the contribution in the x-ray region we use the expression  $\epsilon = 1 - (\omega_p/\omega)^2$  where  $\omega_p$  is the plasma frequency given by  $\omega_p = \sqrt{ne^2/\epsilon_0 m}$ ,  $n$  is the electron density and  $m$  is the electronic mass. While this formula is strictly true only for an ideal plasma of free electrons, it holds approximately for solids provided  $\omega \gg \omega_p$ .

As a numerical example, consider a typical proton-induced x-ray experiment, similar in character to that referred to by Gibb. The relevant parameters are shown in table 3-3.

Re-writing 3-7 to give the number of photons per steradian per unit interval of photon energy we then have

$$\frac{dN}{d(\hbar\omega)d\Omega} = \frac{e^2}{4\epsilon_0\hbar\pi^3c} \frac{1}{\hbar\omega} \frac{\sin^2\theta \cos^2\theta \beta^2}{(1 - \beta^2 \cos^2\theta)^2} \times \left| \frac{(\epsilon-1)(1-\beta^2+\beta\sqrt{\epsilon-\sin^2\theta})}{(\epsilon\cos\theta+\sqrt{\epsilon-\sin^2\theta})(1+\beta\sqrt{\epsilon-\sin^2\theta})} \right|^2 \quad 3-11$$

Substituting the electron density  $4.66 \times 10^{30} \text{m}^{-3}$  into the expression for the plasma frequency gives  $\hbar\omega_p = 80\text{eV}$ . Since for x-rays  $\hbar\omega \gg 80\text{eV}$  and hence  $\omega \gg \omega_p$ , we may use  $\epsilon \approx 1 - (80/\hbar\omega)^2$

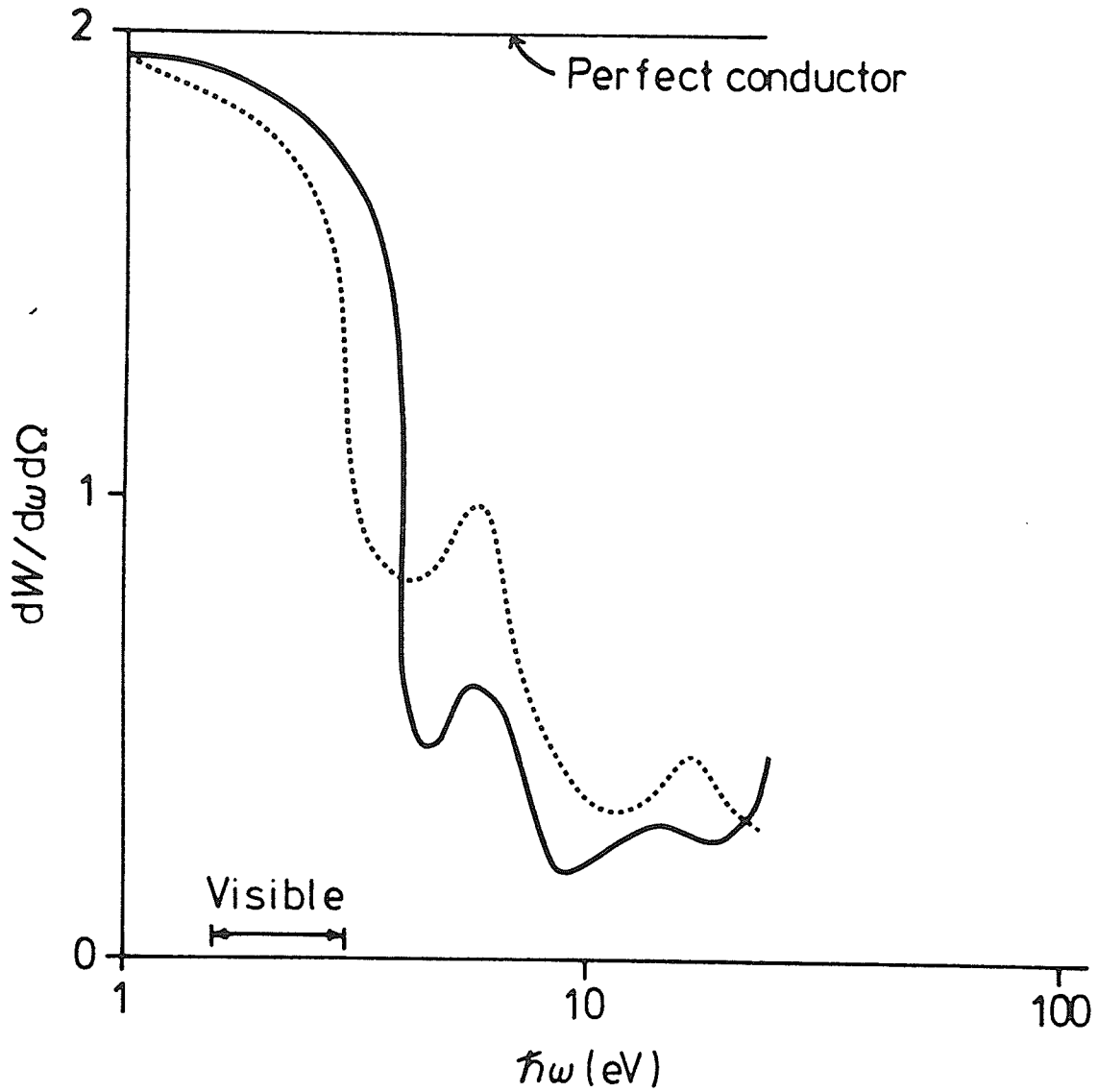


Fig. 3-7 Transition radiation spectra for copper (broken curve) and silver (solid curve) calculated using equation 3-7 with  $\beta = 0.27$ ,  $\theta = 45^\circ$  and  $\epsilon = \epsilon_1 + i\epsilon_2$  from Ehrenreich and Philip (1962).

Target	Gold; total electron density $4.66 \times 10^{30} \text{m}^{-3}$
Incident particles	35 MeV protons; $\beta=0.27$
Beam current	3nA
Run length	1 hour
	} $6.74 \times 10^{13}$ particles
Solid angle ( $d\Omega$ )	$2 \times 10^{-3} \text{sr}$ at $\theta = 45^\circ$

Table 3-3 Typical proton induced x-ray experiment

to evaluate 3-11 in the x-ray region. Let us estimate the number of transition-radiation photons to be detected in the above experiment over a 200 eV interval at 1 keV.

$$\frac{dN}{d\Omega} = \frac{e^2}{4\epsilon_0\hbar\pi^3c} \frac{\sin^2\theta\cos^2\theta\beta^2}{(1-\beta^2\cos^2\theta)^2} \times \int_{\hbar\omega=900\text{eV}}^{\hbar\omega=1100\text{eV}} \frac{1}{\hbar\omega} \left| \frac{(\epsilon-1)(1-\beta^2+\beta\sqrt{\epsilon-\sin^2\theta})}{(\epsilon\cos\theta+\sqrt{\epsilon-\sin^2\theta})(1+\beta\sqrt{\epsilon-\sin^2\theta})} \right|^2 d(\hbar\omega)$$

$\approx 4 \times 10^{-11}$  photons per steradian (for  $\theta=45^\circ$ ,  $\beta=0.27$ ,  $\epsilon=1-(80/\hbar\omega)^2$ ).

With the beam current, run length and solid angle given, this amounts to approximately five transition-radiation photons detected. This number drops sharply with increased photon energy - under the above assumptions, it is down a further three orders of magnitude by 6keV. It should be mentioned that this result depends quite sensitively on the values used for  $\epsilon$ , and more dependable values of the dielectric constant in the x-ray region would be useful. Nonetheless, it seems that the x-ray contribution from transition radiation is very small and is unlikely to be a significant source of background in proton-induced x-ray experiments.

### 3.5 SUMMARY AND CONCLUSIONS

K-shell ionization cross sections have been measured for protons of energy 24, 32 and 44 MeV incident on copper, rubidium, silver, europium and gold. The data represent the most complete set of K-shell ionization cross sections in the energy range. The data were reduced according to a theoretically predicted scaling law. The results are found to be completely consistent with this law.

$K_{\beta}/K_{\alpha}$  x-ray intensity ratios were measured and, for every target, the results at each of the three bombarding energies were compared. To the accuracy of the experiment, the  $K_{\beta}/K_{\alpha}$  intensity ratio does not appear to depend on the energy of the inducing proton. The dependence of the  $K_{\beta}/K_{\alpha}$  ratio on atomic number is in agreement with the theoretical predictions of Scofield (1974).

The spectrum of transition radiation resulting when 35 MeV protons enter a metallic target has been calculated. It is shown that while this radiation is known to be observable in the visible part of the spectrum, that part extending into the x-ray region is insignificant.

## REFERENCES

- O. Aashamar and L. Kocbach, J. Phys. B: Atom. Molec. Phys., 10 (1977) 869
- W. Bambynek, Proc. Int. Conf. on Inner Shell Ionization Phenomena (1972), eds. R. W. Fink, S. T. Manson, J. M. Palms and P. V. Rao (U.S. Atomic Energy Commission CONF-729404, 1973)
- F. D. Becchetti, Jr., and G. W. Greenlees, Phys. Rev. 192 (1969) 1190
- G. Beck, Phys. Rev. 74 (1948) 795
- J. Birchall, M. J. Kenney, J. S. C. McKee, B. L. Reece, Nucl. Instr. and Meth. 65 (1968) 117
- J. Birchall, Ph.D. Thesis, University of Birmingham (1969) unpublished
- J. Birchall, M. J. Kenny, J. S. C. McKee, B. L. Reece, C. O. Blyth and P. B. Dunscombe, Proceedings of the International Symposium on Liquid Scintillation Counting (Salford, 1971) 84
- J. B. Birks, "Theory and Practice of Scintillation Counting" (Oxford, Revised ed., 1967)
- G. A. Bissinger, J. M. Joyce, E. J. Ludwig, W. S. McEver and S. M. Shafroth, Phys. Rev. A1 (1970) 841
- G. A. Bissinger, S. M. Shafroth and A. W. Waltner, Phys. Rev. A5 (1972) 2046
- C. O. Blyth and A. J. Phillips, Private Communication (1975)
- F. Bodart, S. F. J. Wilk and G. Deconninck, X-Ray Spectrom. 4 (1975) 161
- R. C. Byrd, Ph.D. Thesis, Duke University (1978) unpublished
- R. C. Byrd, R. L. Walter and S. R. Cotanch, Phys. Rev. Lett. 43 (1979) 260
- J. L. Campbell and L. A. McNelles, Nucl. Instr. and Meth. 117 (1974) 519
- J. D. Carlson, D. A. Lind and C. D. Zafiratos, University of Colorado Report C00-535-666 (1972)

- J. D. Carlson, C. D. Zafiratos and D. A. Lind, Nucl. Phys. A249 (1975) 29
- R. A. Cecil, B. D. Anderson and R. Madey, Nucl. Instr. and Meth. 161 (1979) 439
- D. A. Close, R. C. Bearse, J. J. Malanify and C. J. Umbarger, Phys. Rev. A8 (1973) 1873
- H. E. Conzett, Phys. Lett. 51B (1974) 445
- S. Cotanch, Florida State University Tandem Accelerator Laboratory Technical Report #4 (1973) unpublished
- S. Cotanch and D. Robson, Phys. Rev. C7 (1973 a) 1714
- S. Cotanch and D. Robson, Nucl. Phys. A209 (1973 b) 301
- R. C. Der, R. J. Fortner, T. M. Kavanagh, K. M. Khan and J. D. Garcia, Phys. Lett. 36A (1971) 239
- C. B. Dover and Nguyen Van Giai, Nucl. Phys. A190 (1972) 373
- M. Drog, Nucl. Instr. and Meth. 105 (1972) 573
- H. Ehrenreich and H. R. Philip, Phys. Rev. 128 (1962) 1622
- J. D. Garcia, R. J. Fortner and T. M. Kavanagh, Rev. Mod. Phys. 45 (1973) 111
- R. P. Gardner and A. Carnesale, Nucl. Instr. and Meth. 73 (1969) 228
- G. M. Garibyan, Sov. Phys.-JETP 33 (1958) 1079
- G. M. Garibyan, Sov. Phys.-JETP 37 (1960) 372
- A. Gibb, J. S. C. McKee and S. F. J. Wilk, J. Phys. D: Appl. Phys. 10 (1977) L203
- V. L. Ginzburg and I. M. Frank, Zh. Eksp. Teor. Fiz. 16 (1946) 15
- P. Goldsmith and J. V. Jelley, Phil. Mag. 4 (1959) 836
- P. D. Greaves, V. Hnizdo, J. Lowe, and O. Karban, Nucl. Phys. A179 (1972) 1
- J. S. Hansen et al., Nucl. Instr. and Meth. 106 (1973) 365

- J. M. Hansteen, O. M. Johnsen and L. Kochbach, At. Data Nucl. Data Tables 15 (1975) 305
- G. W. Hoffman and W. R. Coker, Z. Physik 269 (1974) 307
- Z. Kamal, J. S. C. McKee, W. D. Ramsay, R. Abegg, M. S. A. L. Al-Ghazi, J. Birchall and N. Videla, Phys. Lett. A. (1980) to be published
- J. R. Kane, R. T. Seigel and A. Suzuki, Rev. Sci. Inst. 34 (1963) 817
- G. S. Khandelwal, B. H. Choi and E. Merzbacher, At. Data 1 (1969) 103
- N. A. Korkhmazyan, Izv. Akad. Nauk. 10 (1957) 29
- R. J. Kurz, UCRL-1139 (March 1964)
- A. M. Lane, Nucl. Phys. 35 (1962) 676
- R. Lear and T. J. Gray, Phys. Rev. A8 (1973) 2469
- D. A. Lind, R. J. Peterson and H. W. Fielding, Phys. Rev. C11 (1975) 2099
- R. G. Lovas, Nucl. Phys. A262 (1976) 356
- J. H. McGuire and P. Richard, Phys. Rev. A8 (1973) 1374
- M. W. McNaughton, F. P. Brady, W. B. Broste, A. L. Sagle and S. W. Johnson, Nucl. Instr. and Meth. 116 (1974) 25
- A. Messiah, "Quantum Mechanics, Vol. II" (North-Holland, Amsterdam, 1965) 802
- V. E. Pafamov, Sov. Phys.-JETP 36 (1960) 1321
- D. M. Patterson, R. R. Doering and Aaron Galonsky, Nucl. Phys. A263 (1976) 261
- W. D. Ramsay and J. S. C. McKee, J. Phys. B: Atom. Molec. Phys., 11 (1978) L313
- W. D. Ramsay, M. S. A. L. Al-Ghazi, J. Birchall and J. S. C. McKee, Phys. Lett. 69A (1978) 258
- W. D. Ramsay, J. Birchall and J. S. C. McKee, Nucl. Instr. and Meth. (1980) to be published

- C. P. Randell, J. S. C. McKee and S. F. J. Wilk, J. Phys. G2 (1976) L69
- P. Richard, T. J. Borner, T. Furuta, J. L. Morgan and J. R. Rhodes, Phys. Rev. A1 (1970) 1944
- G. R. Satchler, in "Isospin in Nuclear Physics", ed. D. H. Wilkinson (North-Holland, Amsterdam, 1969) 389
- J. H. Scofield, Phys. Rev. 179 (1969) 9
- J. H. Scofield, Phys. Rev. A9 (1974) 104
- Noel R. Stanton, Ohio State University High Energy Physics Laboratory Report C00-1545-92 (February 1971)
- M. L. Ter-Mikaelyan, Izv. Akad. Nauk. 12 (1959) 141
- W. J. Veigele, At. Data 5 (1973) 51
- B. A. Watson, P. P. Singh and R. E. Segel, Phys. Rev. 182 (1969) 977
- J. W. Watson, J. S. C. McKee and D. J. Roberts, University of Manitoba Cyclotron Laboratory internal report 76/42 (1976)
- J. W. Watson, F. J. Wilson, C. A. Miller and D. O. Wells Nucl. Instr. and Meth. 164 (1979) 129